Autonomous University of Nuevo León
School of Chemical Science

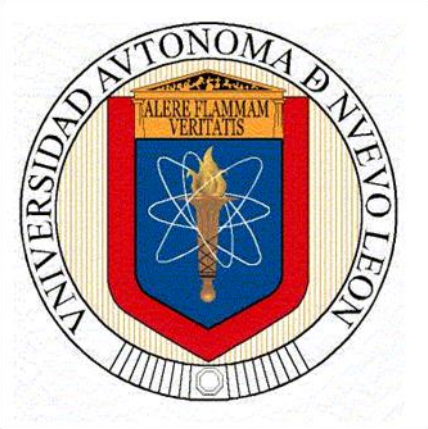

Doctoral Thesis

Doctorado en Ciencias con Orientación en Procesos Sustentables

Folio number: 2-98135-PST-18/208

DESIGN AND EVALUATION OF A 3D PRINTED MOF-MONOLITH FOR THE REMOVAL OF VOLATILE ORGANIC COMPOUNDS FOR INDOOR ENVIRONMENTS

Author: M. C. Alan Antonio Rico Barragán

Supervisor:

Dra. Nancy Elizabeth Dávila Guzmán

Monterrey, N. L., May 31st, 2023.
Laboratory of Wastewater Treatment 1

Aprobación de la Tesis:

_____

Dra. Nancy Elizabeth Dávila Guzmán

Director de Tesis

_____

Dra. Margarita Loredo Cancino

Comité Tutorial

_____

Dr. Jacob Josafat Salazar Rábago

Comité Tutorial

_____

Dr. Javier Antonio Arcibar Orozco

Comité Tutorial

_____

Dra. María Elena Cantú Cárdenas

Subdirectora de Estudios de Posgrado

Acknowledgments

Obtaining the degree of Doctor of Science has been one of the professional goals I achieved with the support of many of my teachers, colleagues, and friends. Thank you for all:

Dra. Nancy E. Dávila Guzmán
Dr. Jacob Josafat Salazar Rábago
Dra. Margarita Loredo Cancino
Dr. Dr. Javier Antonio Arcibar Orozco
Dr. Víctor Manuel Ovando Medina
Dr. Marco A. Garza-Navarro
Dr. J. Raziel Álvarez
Dr. Pasiano Rivas García
Dr. José Bonilla Cruz
Dra. Tania E. Lara Cisneros
Dr. Manuel Alejandro Ávila López
Dr. David A. de Haro del Río
Dr. Gerardo Antonio Flores Escamilla
Dra. Anabel Álvarez Méndez
Dr. Eugenio Hernández
Dr. Joelis Rodríguez-Hernández
Dr. Carlos Javier Lucio Ortiz
Dr. Sanal Kozhiparambil
Norma Tiempos Flores
Gloria Azucena Buitimea Cerón
Jawer David Acuña Bedoya
Clovis Nchikou
Cinthia Berenice García Reyes
Tijin Thomas
Evelyn Figueroa
Daniela Treviño
Arely Núñez
Muhammed Faisal
Karan Singh

I appreciate Dra. Nancy Dávila shared her knowledge with me to be patient, believe in me and the project, and, more importantly, be a great advisor. Thank you to my committee: Dra. Margarita, Dr. Javier, and Dr. Jacob. Thank you, Dr. Pasiano, for the reviews and observations. I appreciate all your comments on my work. Colleagues and friends, thank you for your support to continue the project and for your help in the laboratory. I am grateful to the Faculty and Postgraduate Chemical Sciences personnel at the Autonomous University of Nuevo Leon and the CONACYT for the openness to obtaining permits, spaces, and resources I needed to complete my doctoral project. Finally, I'm grateful to my family for their encouragement as I pursued my Ph.D.

Abstract

Alan Antonio Rico Barragán Fecha de graduación:

Universidad Autónoma de Nuevo León

Facultad de Ciencias Químicas

Study Title: DESIGN AND EVALUATION OF A 3D-PRINTED MOF-MONOLITH FOR THE REMOVAL OF VOLATILE ORGANIC COMPOUNDS IN INDOOR ENVIRONMENTS.

Number of pages: 136 pages

Candidate for the degree of Doctor of Science with Orientation in Sustainable

Study area Engineering, new materials for adsorption processes.

Purpose and method of study The change in conventional MIL-101(Cr) synthesis, use of PET as an organic linker, and avoiding solvents/toxic modulators is investigated through environmental, economic, and technical factors. Furthermore, DOZN™ software was applied to determine the impact on 12 Green Chemistry Principles; meanwhile, the life cycle assessment of MIL-101(Cr) scenarios (M1-M7) are also evaluated. Also, the Monte-Carlo simulation was carried out to obtain a cost with significant probability, counting the variability of raw materials, equipment, and the energy cost necessary to produce 1 g of MIL-101(Cr). Furthermore, technical analysis of MIL-101(Cr) powder materials were evaluated by toluene adsorption. In addition, the ideal synthesis route was selected by the Technique for Order Preference by Similarity to Ideal Solution (TOPSIS) methodology. Finally, 3D printing was used to obtain a MIL-101(Cr)-monolith, and the adsorption capacity of MOF powder and MOF immobilized into monolith was evaluated. The continuous adsorption process was applied at a toluene concentration of 250 ppm and 250 mL min^{-1} at laboratory conditions.

Contributions and Conclusions Optimization of the synthesis process resulted in a MIL-101(Cr) with good textural properties, which behaves as a strong adsorbent suitable for toluene capture at lower concentrations (~2 ppm). The ideal synthesis route was M7; avoiding DMF, changing the commercial linker by PET, and the no use of toxic modulators decreases the impact observed in the Green Chemistry Principle. The LCA methodology obtained similar results; M7 showed 64% minor environmental impact, and applying economic analyses was 34% more economical than a conventional synthesis. In addition, MOF powders were successfully immobilized in monolith (90% wt MOF and 10% Kaolin clay) by 3D printing technique. Continuous adsorption tests with the 3D printed monolith presented a similar adsorption capacity (46 mg g^{-1}) as MOF powders (52 mg g^{-1}).

Thesis Advisor:

_____

Dra. Nancy Elizabeth Dávila Guzmán

TABLE OF CONTENTS

List of Figures

List of Tables

1. Introduction

1.1. Air Pollution

Breathing air that presents different pollutants has been shown to have many side effects on human health. The consequences could be dangerous depending on the concentration and the type of contaminants.[1] Around the world, health and environmental departments have expressed that air pollution is a public health problem. The World Health Organization (WHO) (2019) defined that nearly 90% of the world's population lives in areas where air quality levels exceed WHO limits. Around the world, almost 3.8 million people die yearly because of household air pollution and another 4.8 million from exposure to air ambient with important levels of gases or particles.[2–4]

It is recorded that more time is spent inside closed environments, houses, apartments, cars, and restaurants, so living conditions in interior areas are relevant.[5,6] It should be mentioned that WHO (2019) declares clean air as a basic need for the health and well-being of human beings. Air pollution is a result of a mixture of different chemicals such as carbon monoxide (CO), carbon dioxide (CO_2), ozone (O_3), nitrogen dioxide (NO_2), sulfur dioxide (SO_2), particulate matter (PM), and volatile organic compounds (VOCs).[7–9] VOCs are emitted into the atmosphere by several sources. Depending on the specific compounds, an environmental impact and toxic effects can be defined. These compounds can be found in ambient air and are known to play an important role in indoor air pollution.[10,11]

1.1.1. Organic Volatile Compounds (VOCs)

VOCs are a large group of organic chemicals that readily evaporate at room temperature due to their high vapor pressure of over 133.3 Pa.[12] The VOCs are a group of pollutants produced by different human activities or anthropogenic sources; emissions from petroleum industries, gas stations, cars, and energy plants are based on hydrocarbons. In indoor environments, the emissions from household products, paints, varnishes, and waxes all contain organic solvents, as do many cleaning items, in some cases of electronics, where VOCs are one of the common ingredients. When these organic compounds are emitted into the environment, they form smog.[13–15]

Several VOCs are considered toxic, depending on concentration, contact time, and age of the person, which can increase the risk of affecting public health. The adverse effects of VOCs on health include irritation of the skin and eyes; also, the respiratory system presents affectations as asthma, in some cases, cardiovascular disease, and, depending on the pollutant, a probability of cancer.[16] For example, benzene and toluene are significant pollutants easily found indoors. Benzene is carcinogenic to humans; the risk of leukemia is presented if contact with this pollutant is regular [17]. Toluene is used as a solvent; the main form of toluene is introduced to the body by inhalation; the exposure carries out affectations in different systems of the body, especially the reproductive system.[18,19]

VOCs not only present affectations on human health but are also precursors of pollutants; they react with NOx in the presence of solar light to form tropospheric O_3, a secondary pollutant. [20] In indoor environments, different VOCs can be observed; Huang et al. (2021) analyzed indoor-outdoor air pollution in 8 houses; higher indoor pollutants were limonene (31.5 μg m^{-3}), followed by toluene (20.4 μg m^{-3}) and formaldehyde (11.7 μg m^{-3}). Meanwhile, under outdoor conditions, toluene was the most abundant VOC species (20.5 μg m^{-3}). [21] The removal of VOCs is necessary because environmental affections and toxic effects can occur even at low concentrations.[22]

1.2. Adsorption as Technology for Indoor Air Purification

The research and development of techniques for removing VOCs in indoor environments have gained interest due to the environmental and public health problems they represent.[23] VOC removal techniques can be described as destructive or recovery processes. Photocatalysis and catalytic oxidation correspond to destructive techniques. Meanwhile, recovery techniques include membrane separation, condensation, absorption, and adsorption.[24]

The most used technique for VOC removal is adsorption, a process in which the molecules of the substance of interest are retained on the surface of a material known as an adsorbent.[25] Although adsorption becomes relevant due to lower energy consumption and low operating costs, the materials used must have a high capacity to remove the contaminant and stability.[5] Adsorption onto activated carbon (AC) is the most widely used

contaminant gas removal technique. Its low cost and high regeneration capacity are two characteristics of great importance.[26] Zeolites are another material used for gas adsorption; the microporous mineral structure is appropriate to trap gases within small channels. There are about 300 types of zeolites, 40 of them are natural, and the rest are synthetic.[28] However, new materials has been developed increasing surface area than CA and Zeolites.[29]

1.3. Metal-Organic Frameworks (MOFs)

Metal-organic frameworks have recently become popular because of their features and wide applications. The expression MOF was first introduced by Omar Yaghi in 1995 when he synthesized a copper-4,4'-bipyridyl complex that exhibits metal-organic interactions.[30] MOFs are a class of materials composed of metal ions or clusters (titanium, zinc, chromium, lead, scandium, and vanadium ions have been used) linked by organic ligands to form porous and crystalline structures (Fig. 1).[31,32]

Metal-organic frameworks represent a new stage of development of porous materials in which the pore size and the active site structure can be modified within wide limits.[33,34] MOF presents a uniform pore distribution, with a pore diameter of 0.5 to 10 nm. In addition to being lightweight materials, they are also characterized by a high specific surface area. On average, they exhibit values ranging from 1500 to 4000 m^2 g^{-1}, although some can reach 10000 m^2 g^{-1}.[35]

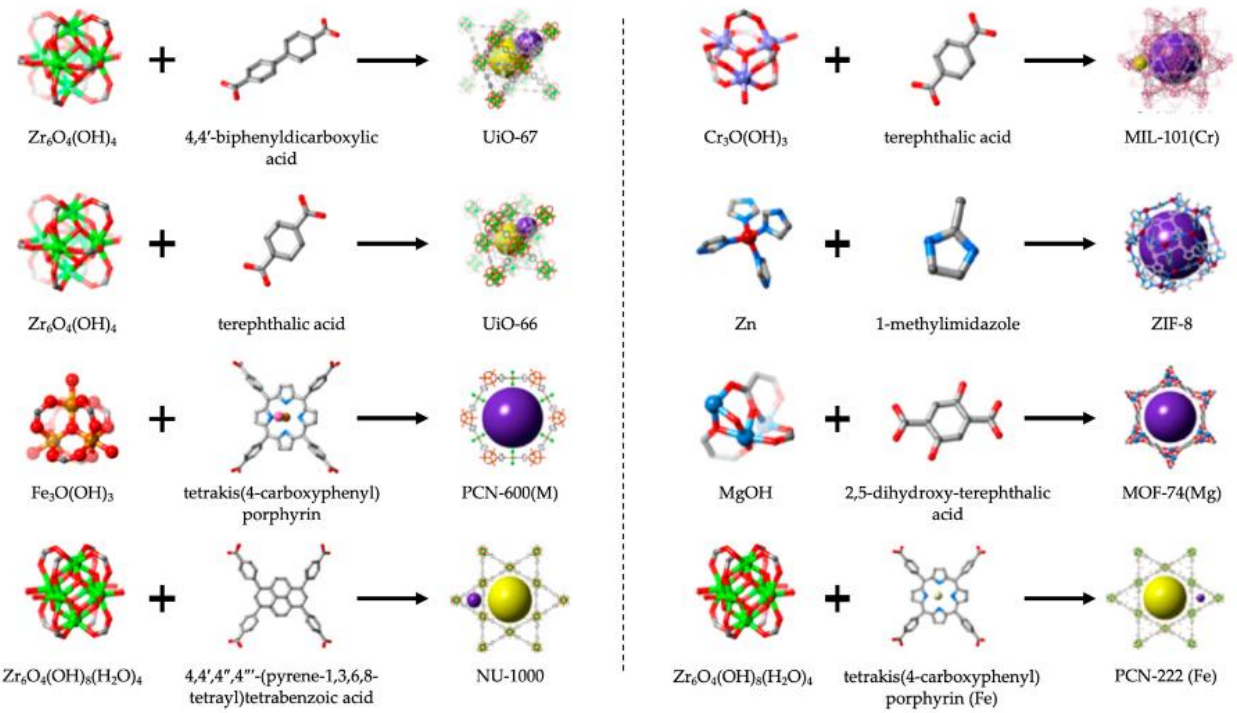

Fig. 1. MOF structures with their corresponding organic linkers and metallic clusters.[36]

Overall, MOFs are a rapidly developing class of materials with a wide range of potential applications in different fields; numerous studies on the development of MOFs have been conducted because of their ideal properties in the fields of gas adsorption for the storage of fuel gases[37,38] as well as in the area of gas separation as an adsorbent material.[39,40] A diverse variety of MOFs have demonstrated an affinity to adsorb or separate gaseous mixtures of VOCs and CO_2, attributed to the strong interaction between the sites of the unsaturated metal and electron donation.[41,42] In this sense, MIL-101, MIL-53, and CPM-5 were tested for VOCs adsorption; MIL-101(Cr) showed a much higher adsorption capacity (2115 mg g^{-1} and 2060 mg g^{-1}) for both toluene and isobutanol compared to MIL-53 (730 mg g^{-1}, 730, and 643 mg g^{-1}) and CPM-5 (338 mg g^{-1} and 569 mg g^{-1}). [43]

1.3.1. MIL-101(Cr)

Many research groups have adopted a short acronym to identify their materials, which generally refers to the institute where the materials were created, such as MIL-101(Cr) for Matériaux Institut Lavoisier. MIL-101(Cr) presents an MTN zeolite topology with the empirical formula $[Cr_3(O)X(BDC)_3(H2O)_2]^*nH_2On$ (BDC=benzene-1,4-dicarboxylate, X = OH or F, *n* is ~25), also the structure presented two types of inner cages (2.9 and 3.4 nm) with two windows (1.2 and 1.6 nm) (Fig. 2), and BET surface area higher than 3000 $m^2 g^{-1}$.[44]

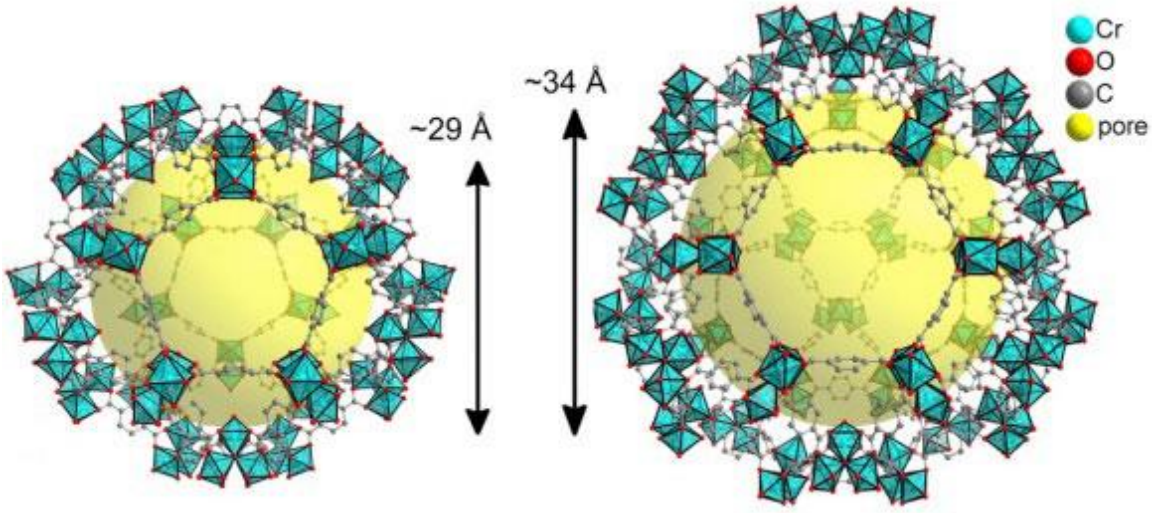

Fig. 2. Structure of MIL-101(Cr) [45].

Among all the applications, MIL-101(Cr) is a suitable adsorbent of indoor air toxic pollutants like volatile organic compounds (VOCs). The π-π interactions and cation-π interactions between MOF-VOC are stronger than C-π and O-π interactions from carbon-VOC or zeolite-VOC, respectively. [42,46] MIL-101(Cr) has been compared with other MOFs

to remove toluene from closed areas; it presented higher capacity adsorption at 30% relative humidity (RH). [43]

The conventional synthesis of MIL-101(Cr) consists of the reaction of terephthalic acid (H_2BDC) (166 mg, 1 mmol) with chromium (III) nitrate nonahydrate (400 mg, 1 mmol), hydrofluoric acid (0.2 ml, 1 mmol), and H_2O (4.8 mL, 265 mmol), for 8 hours at 220 °C [47]. In conjunction with growing alarms and worries about minimizing the influence on the environment of chemicals and hazardous substances, there has been a change in conventional synthesis to eco-friendly methods. [48]

Recently, several methods have been tried to synthesize HF-free MIL-101(Cr), taking a count of different less corrosive and toxic modulators used to improve nuclei formation and modified crystal growth.[49] Instead of commercial H_2BDC, several studies propose using poly(ethylene terephthalate) (PET), which contains H_2BDC within its structure. MIL-47, MIL-53 (Cr), MIL-53 (Al), MIL-53 (Ga), and MIL-101(Cr) have been synthesized using PET as a precursor of H_2BDC; the PXRD pattern of the MOFs matches the simulated pattern. Even though this process offers an economically attractive strategy for eliminating waste PET streams while making value-added materials, the change in commercial organic ligand increases the amount of the modulator (HF or HCl).[50] A different MOF, UiO-66(Zr), was obtained using waste PET bottles as a source of an organic linker. As a result, UiO-66(Zr) (BDC-derived PET) presented a low BET surface area (814 $m^2\ g^{-1}$) compared with conventional synthesis (1171 $m^2\ g^{-1}$).[51] Another study was elaborated by Zhou et al. (2019); they used formic acid and acetone as solvents in

the depolymerization reaction of PET. The MOF revealed high thermal and hydrothermal stability in the air but continued using a commercial ligand. Although several studies manifest that a change in conventional synthesis offers a sustainable version of MOF, the environmental impact is rarely evaluated.[52]

1.4. Adsorption Isotherms

Adsorption isotherms are commonly used to analyze adsorption processes to express equilibrium data at constant temperature and relate the equilibrium adsorption capacity (q_e) to the equilibrium adsorbate concentration (C_e).[53] Adsorption isotherms are essential for designing continuous and batch adsorption systems; the shape of such isotherms holds much information regarding the adsorption process's nature.

The simplest form of an adsorption isotherm is a linear'equation (Henry's isotherm), a mathematical model that describes the adsorption of gas molecules onto a solid surface at low pressures. Specifically, the Henry isotherm describes the linear relationship between the amount of gas adsorbed on the surface and the gas pressure in the surrounding environment. Henry's model approximates the data trend only at low solute concentrations such that all adsorbate molecules are separated from their closest molecules. Hence, it shows monolayer adsorption at initially low adsorbate concentrations.[54] [55] Thus, Henry´s model is related to the following linear expression:

$$q_e = K_e^H C_e \qquad \text{Eq. 1}$$

Where q_e is the amount of the adsorbate at equilibrium per gram of adsorbent (mg g^{-1}), K_e^H is Henry's adsorption constant, and C_e is the equilibrium concentration of the adsorbate in the solution.

The Langmuir isotherm is another model generally used to describe adsorption equilibrium; the model describes gas-solid interaction based on kinetic principles. [56] The Langmuir model applies to homogeneous adsorption, where the adsorption of adsorbate molecules onto the surface has equal sorption activation energy.[57] The following equation represents the non-linear form of Langmuir isotherm:

$$q_e = \frac{q_m K_L C_e}{1+K_L C_e} \qquad \text{Eq. 2}$$

Where q_m is the theoretical monolayer saturation capacity, and K_L (L g^{-1}) is the Langmuir equilibrium constant.

A critical consideration of the Langmuir isotherm is the separation factor, or equilibrium parameter (R_L):

$$R_L = \frac{1}{1+K_L C_0} \qquad \text{Eq. 3}$$

Where C_0 is the initial concentration of adsorbate (mg L^{-1}). If R_L <1, the adsorption is favorable, near 0 indicates that adsorption is irreversible; meanwhile, R_L = 1 suggests that the adsorption isotherm is linear, and finally, R_L > 1 corresponds to unfavorable adsorption. [57]

The Freundlich model is the most significant multisite adsorption isotherm for heterogeneous surfaces; this model also considers the exponential distribution of active sites and their energies. [56,57] The non-linear form of the Freundlich isotherm is as follows:

$$q_e = K_F C_e^{\frac{1}{n}} \qquad \text{Eq. 4}$$

Where is K_F (L g^{-1}) is the adsorption capacity or Freundlich constant and $\frac{1}{n}$ is the adsorption intensity; $0<\frac{1}{n}<1$ the adsorption is assumed favorable, meanwhile $\frac{1}{n}>1$ is considered unfavorable and is irreversible at $\frac{1}{n} = 1$.

1.5. Adsorption Kinetics

Adsorption kinetics describes the amount of adsorbate retained on the adsorbent over time; the study provides information on the adsorbent's performance and the mass transfer mechanisms. The adsorption kinetic is essential for the design of adsorption systems.[58] Generally, the adsorption rate considers three stages carried out simultaneously: external diffusion, internal diffusion, and adsorption on active sites (Fig.3).[59]

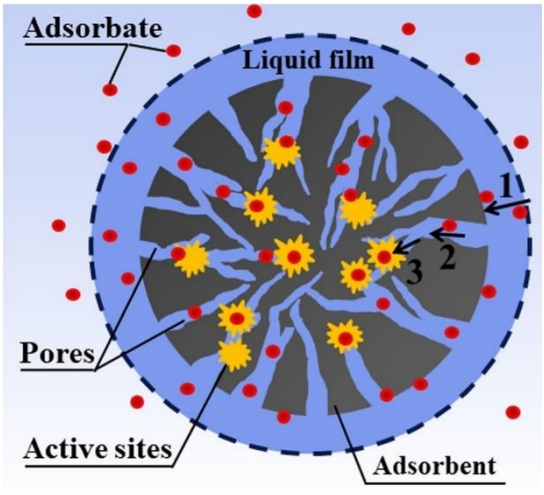

Fig. 3. Adsorption steps 1) external diffusion, 2) internal diffusion, and 3) adsorption on active site.[58]

Internal diffusion is related to the transport of adsorbate molecules inside the porous structure of the adsorbent. When the pores of the adsorbent are sufficiently large, the adsorbate molecules can diffuse freely within the material until they reach the adsorption sites. However, when the pores are small, the adsorbate molecules may experience resistance to their movement due to the narrow pore size, resulting in slower internal diffusion.[60] On the other hand, external diffusion refers to the transport of adsorbate molecules from the bulk gas phase to the surface of the adsorbent. This process occurs when the adsorbate molecules must travel through the thick gas layer surrounding the adsorbent particles before reaching the adsorption sites on the surface.[61]

The main difference between internal and external diffusion is the location of the mass transfer process. Internal diffusion occurs within the porous structure of the adsorbent, while external diffusion occurs in the surrounding gas phase. Both internal and external

diffusion can be rate-limiting steps in the overall adsorption process, depending on the specific conditions of the system.[61]

Active sites in adsorption refer to specific regions or sites on the surface of a solid material responsible for the adsorption of molecules or particles. These sites typically have a particular geometry or arrangement of atoms that enable them to interact with the adsorbate in a specific way and are often chemically active.[59]

A kinetic model in adsorption is a mathematical representation of the adsorption process that describes the rate at which adsorbate molecules or particles are adsorbed onto an adsorbent material.[61,62] Different factors that can affect the adsorption kinetics include the size and shape of the adsorbate molecules, the pore size and structure of the adsorbent material, and the temperature and pressure of the adsorption system. Kinetic models can be used to investigate the effects of these factors on the adsorption behavior and to identify optimal conditions for adsorption.[63]

Various adsorption kinetic models have been applied to describe gas adsorption into solid adsorbents, such as the pseudo-first-order (PFO) model, the pseudo-second-order (PSO) model, and Elovich´s model.[61] According to the PFO model, the rate of change in the adsorption of adsorbate at a specific reaction time is directly proportional to the difference in concentration and rate at which the adsorbate is adsorbed.[64] The linearized equation of the PFO model is described as follows:

$$\ln(q_e - q_t) = \ln q_e - k_1 t \qquad \text{Eq. 5}$$

Where q_t is the adsorption capacity of the adsorbent at time *t* (mg g^{-1}), k_1 is the rate constant for PFO adsorption model (min^{-1}).

PSO model (Eq. 6) describes that the rate of solute adsorption is proportional to the number of available sites on the adsorbent. The reaction rate is proportional to the quantity of solute on the surface of the adsorbent, and the driving force (q_e-qt) is dependent and related to the number of active sites on the adsorbent. [65]

$$\frac{t}{q_t} = \frac{1}{k_2 q_e^2} + \frac{1}{q_e}(t) \qquad \text{Eq. 6}$$

Where q_t is the adsorption capacity of the adsorbent at time *t* (mg g^{-1}), k_2 is the rate constant for PSO adsorption model (g mg^{-1} min^{-1}).

Elovich´s model is an empirical model without definite physical meanings that describes the PSO kinetic further, assuming that the sorbent surface is energetically heterogeneous. [66] Eq. 7 describes Elovich´s model:

$$q_t = \frac{1}{\beta}\ln(\alpha\beta) + \frac{1}{\beta}\ln(t) \qquad \text{Eq. 7}$$

Where α is considered the initial rate of adsorption (mg g^{-1} min^{-1}), β is the desorption constant (g mg^{-1}), and q_t is the adsorption capacity of the adsorbent at time *t* (mg g^{-1}).

1.6. Breakthrough Curve

A breakthrough curve can be used to characterize the performance of types of materials used in separation processes.[67] In general, breakthrough curves are generated by measuring the concentration of the substance in the feed stream, the effluent stream, and potentially other points in the process, at various time intervals. [68,69] Various breakthrough curve models have been applied to describe adsorption process into solid adsorbents, such as Thomas and Yoon Nelson model.

The Thomas model is a widely used empirical model assuming that the adsorption process is governed by the equilibrium between the solute concentration in the bulk fluid and the concentration on the adsorbent surface. The adsorption model takes into account negligible axial dispersion since the rate driving force obeys the second order reversible reaction kinetics.[69] The Thomas model equation is typically represented as:

$$\frac{C_t}{C_o} = \frac{1}{1+\exp\left(\left(\frac{k_{Th}}{Q}\right)(q_{Th}m - C_o Q t)\right)} \qquad \text{Eq. 8}$$

Where $\frac{C_t}{C_o}$ is the dimensionless concentration ratio, k_{Th} is the adsorption rate constant of Thomas model (mL min^{-1} g^{-1}), Q is the volumetric flow rate (mL min^{-1}), m is the adsorbent mass (g), C_o (mg L^{-1}) represents the inlet concentration, and q_{Th} (mg g^{-1}) represents the adsorption capacity.

The Yoon-Nelson model assumes that the adsorption process is governed by a combination of external mass transfer limitations and internal pore diffusion limitations within the adsorbent.[69] Yoon-Nelson model can be used to estimate the breakthrough time, or the point at which the concentration of the solute in the effluent stream first exceeds a predetermined threshold value. Yoon-Nelson data model is obtained by following equation:

$$\frac{C_t}{C_O} = \frac{1}{1+ e^{K_{YN}(\tau - t)}} \qquad \text{Eq. 9}$$

Where K_{YN} (mL min^{-1}) is the rate constant and τ is the time required for 50% adsorbate breakthrough.

1.7. Green Chemistry Principles

IUPAC has defined Green Chemistry as “The invention, design, and application of chemical products and processes to reduce or to eliminate the use and generation of hazardous substances” [70]. The Green Chemistry concept involves the product and process design with the aim of less use and generation of hazardous materials [71]; on the contrary, it seeks to prevail in the application of renewable materials and green energy [72]; in that sense, twelve principles are established (Fig. 4).

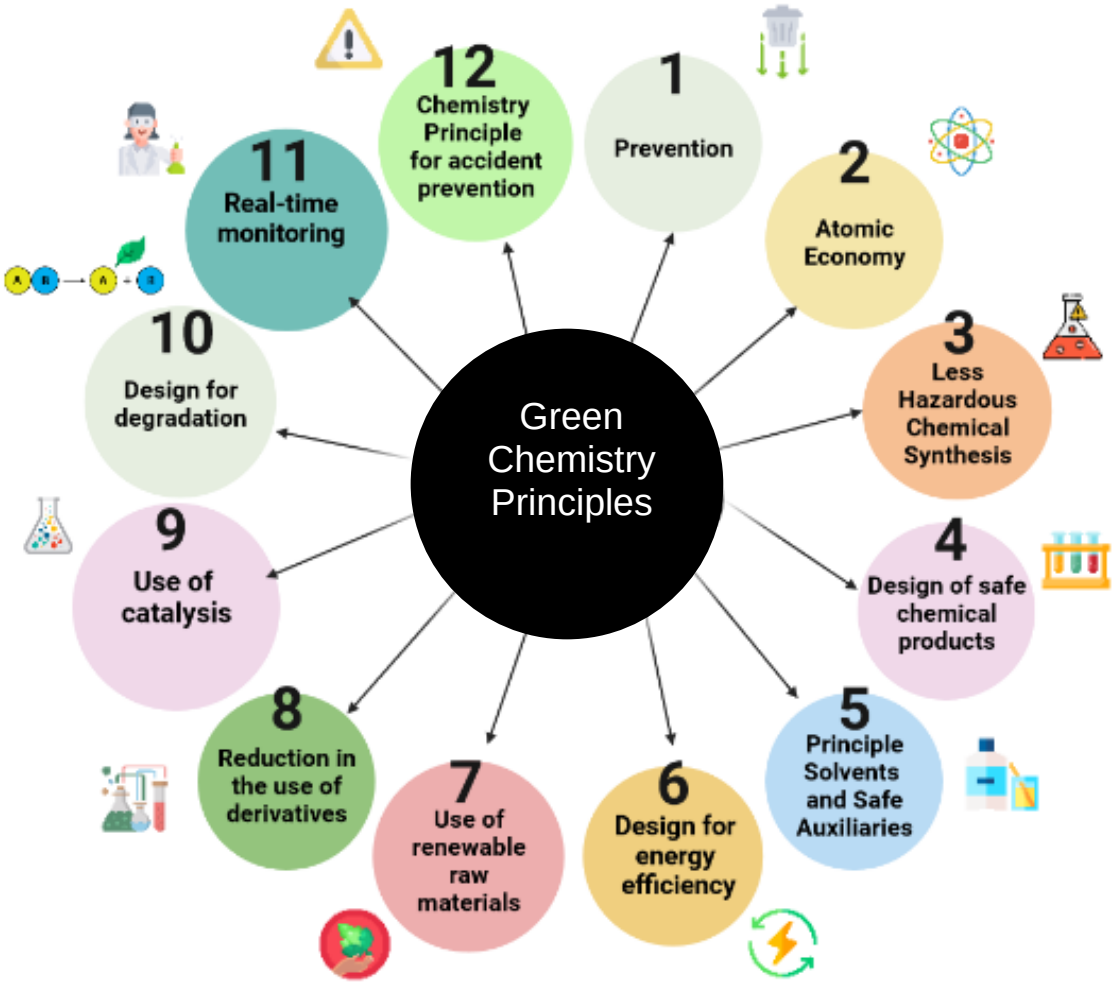

Fig. 4. Twelve principles of green chemistry.

Green chemistry principles are guidelines and concepts that promote the design of chemical products and processes that are environmentally friendly, sustainable, and safe for human health. [71,73]

The 12 principles of green chemistry are as follows:

1st Principle Prevention: It is better to prevent than to treat or eliminate residues after being synthesized.

2nd Principle Atomic Economy: The synthesis routes must be designed to maximize the incorporation of the raw material in the final product.

3rd Principle of Less Hazardous Chemical Synthesis: Whenever possible, the synthesis routes must be designed to use and generate substances with little or no toxic impact on the population's health and the environment.

4th Principle Design of safe chemical products: Chemical products must be designed to preserve their efficiency in their application while reducing their toxicity.

5th Principle Solvents and Safe Auxiliaries: The use of auxiliary substances should be minimized whenever possible and in the same way innocuous.

6th Principle Design for energy efficiency: The energy requirements of the chemical process must be considered due to their economic and environmental impacts and minimized, seeking to be at environmental conditions of temperature and pressure.

7th Principle Use of renewable raw materials: Priority should be given to using them as long as they are technically and economically feasible.

8th Principle Reduction in the use of derivatives: The use of derivatives in the chemical process as blocking groups, protection/deprotection, or modification of chemical or physical processes should be avoided as much as possible because it requires additional reagents that can generate waste.

9th Principle Use of catalysis: Catalytic reagents are superior to stoichiometric reagents.

10th Principle Design for degradation: The synthesized chemical products, once their function is finished, must decompose into innocuous products and not persist in the environment.

11th Principle Real-time monitoring: Analysis methodologies must be sensitive enough to monitor and control the process under continuous conditions to avoid forming unwanted substances.

12th Safer Chemistry Principle for accident prevention: Substances and their chemical form used in processes must be selected to minimize the potential for chemical accidents, including explosions or fires.

Generally, the green synthesis of MOFs relies on non-toxic reactants, a non-toxic solvent, mild conditions, and fewer byproducts.[74] However, only a few studies present the evaluation of green chemistry for MOF synthesis, and researchers only focus on change the solvent that use in the synthesis. For example, toxic DMF was replaced by cyrene, a biobased solvent from waste cellulose, in synthesizing HKUST-1, ZIF-8, and UiO-66; MOFs exhibited similar XRD patterns compared to MOF conventional production with DMF but presented lower BET surface area (ZIF-8 and UiO-66).[75]

Although the change of toxic solvents by eco-solvent has been carried out, the environmental impact quantification was not observed. In this sense, the transition from qualitative to quantitative assessments has been a critical advancement in green chemistry and green synthesis of metal-organic frameworks. [76]

1.8. Life Cycle Assessment

Life Cycle Assessment (LCA) is another way to measure the environmental impact of material production. LCA is essential from a sustainability viewpoint since it considers a product or service's complete life cycle and the requirements to manufacture it, avoiding local improvements from simply moving the environmental impact elsewhere. [77]

The ISO 14040 standard outlines the LCA approach into four phases: aim and scope definition, inventory analysis, impact assessment, and interpretation. [78] The product or process under research and the study's objective are mentioned in the goal and scope specification. [79] For example, other adsorbents, such as activated carbon, presented LCA to evaluate the principal contributor to environmental damage; as a result, the use of reactants has a mainly negative effect. [77,80]

Similar studies of LCA of MOF synthesis presented that a low solvent consumption compared with the conventional procedure can reduce the impact on environmental indicators. For example, four different routes synthesized CPO-27-Ni; the significant environmental impacts of the MOF procedure are observed in the synthesis and cleaning stage; the reduce of organic solvents can decrease near 1100 kg CO_2 eq in climate change category indicator.[81] Meanwhile, the DUT-4 scenario avoiding DMF decreased to near 90% environmental impacts, although the adsorption capacity of the material was lower than conventional synthesis. [82]

The Green Chemistry Principle 4, applied to MOF production, explains that chemical modifications to MOF procedure should be designed to preserve the efficacy of function while reducing toxicity.[83,84] To the best of our knowledge, no study about using the LCA of MIL-101(Cr) synthesis exists.

1.9. Economic Assessment of MOF Production

Manufacturing a novel green product depends on a deep perception of its economic and environmental effects. [85] Therefore, financial performance is one of the most crucial aspects in designing chemical processes such as adsorption. [86]

Monte Carlo (MC) simulations have been employed to perform the economic assessment of a material or process by simulating the product's financial performance under various scenarios and assumptions. MC simulation is a computational technique that models and analyzes complex systems or processes through random sampling and probability theory. [87,88]

The following steps can be followed to perform an MC simulation:

1. Define the key variables: Identify the key variables that will affect the financial performance of the new material product. These variables may include the raw materials price, production costs, electricity value, equipment cost, and product lifespan.

2. Determine the probability distributions: Assign a probability distribution (normal, triangular, exponential, or uniform) to each variable that reflects the range of possible values and the likelihood of each value occurring.
3. Generate random samples: Use a random number generator to generate many random samples for each variable based on the assigned probability distribution.
4. Calculate the economic performance: Use a financial model to calculate the product cost.
5. Analyze the results: Analyze the distribution of the financial metrics across all the random samples to estimate the range of possible outcomes and the probability of achieving certain levels of financial performance. This analysis can identify the key drivers of financial performance, assess the risk of the investment, and make informed decisions about the viability of the new material product.

As a MOF procedure cost, MC simulation can be a valuable tool for evaluating the economic value of a new material product, allowing researchers to estimate the probability of achieving various levels of financial performance and identify the key factors that drive that performance. [89]

1.10. Immobilization of MOF

The immobilization of Metal-Organic Frameworks (MOFs) involves attaching or bonding these porous materials onto a solid support or substrate, such as a polymer, ceramic, or metal surface, to enhance their stability and durability under various conditions.

Furthermore, producing MOF materials in powders that present particle sizes between 100 nm and 50 mm can produce high-pressure drops, obstruction, and high fouling when used in columns packed at an industrial scale. [90] For this reason, it is relevant that powder-adsorbent materials can be immobilized. The choice of immobilization method depends on the specific application; for example, MOF materials have been processed in pellets, fibers, spheres, and monoliths, but they continue to present challenges due to adsorption efficiency.[91]

1.10.1. Pellets

One of the most frequent methods for structuring powder materials is to shape MOF into pellets. Pellets are made by applying pressure to a powdered substance with or without a binder. Exists two ways to obtain MOF-pellets: tableting or extrusion.[92] First, the powder adsorbent is exposed to precise mechanical pressure using a laboratory press; when pellets are formed via tableting, the tablet may be crushed and sieved to a specified size in some circumstances.[93] Meanwhile, extrusion of pellets involves the fabrication of a paste consisting of a solvent, either a binder or not. Finally, to obtain the pellet, the paste is extruded via a die (Fig 5).

Mechanical or hydraulic pressure and the binder chosen are essential to present a suitable structure. With increased pelletization pressure, mechanical stress can affect crystallinity, but hydraulic pressure can give mechanical strength while reducing surface area.[95] In the case of binder, has been utilized polymers (e.g., polyvinyl alcohol,

polyvinylchloride, methylcellulose, polystyrene, polyvinyl formal, cellulose-acetate, polyetherimide) and minerals (e.g., kaolinite, bentonite, silica). A low binder loading is sought to form MOF pellets to avoid reducing the MOF powder properties but enough to provide mechanical strength.[96,97]

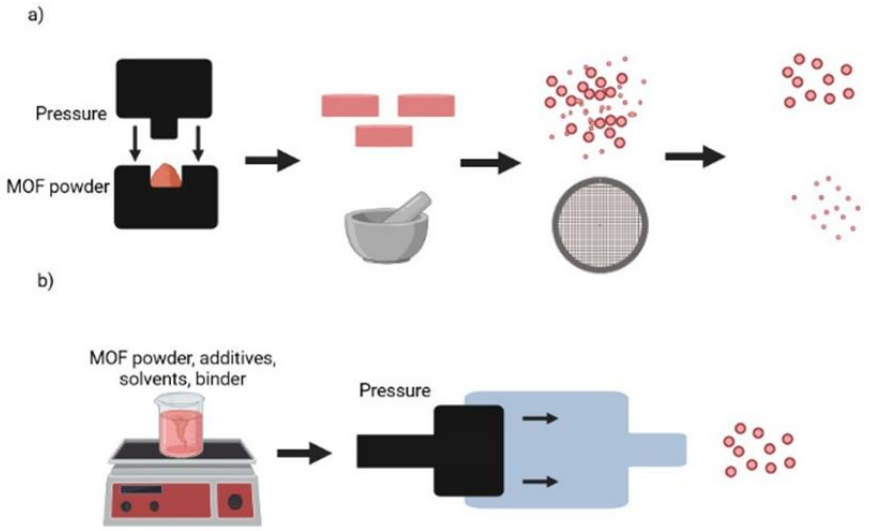

Fig. 5. Methods to form pellets (a) tableting and (b) extrusion. [94]

1.10.2. Spheres

Spheres is other form of MOF can be immobilized; the phase inversion method can be applied to obtain these structures. The novel technique prepared MOF composite spheres using a single orifice spinneret and a polymer as the binder (Fig 6). An advantage of these methods is that the dimensions of composite spheres can be controlled.

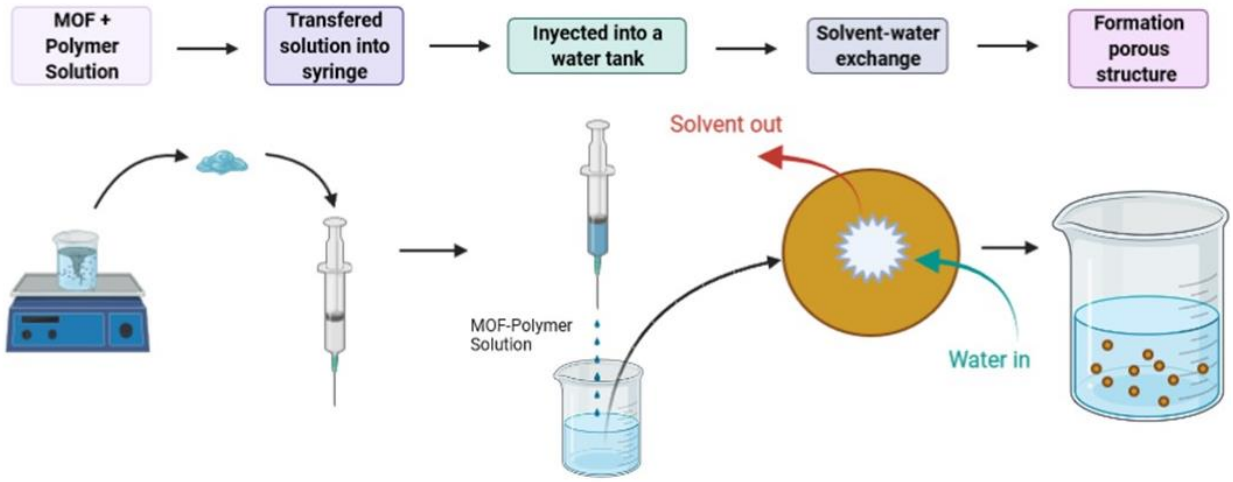

Fig. 6. Phase inversion process to form MOF/Polymer spheres. [98]

The dispersion process is a method to obtain MOF spheres; a single-step technique to produce composite structures with micrometer-sized particles. In this process, a monomer is dissolved in a solvent, the prepared polymer is insoluble, and polymer particles begin to shape and stabilize as the reaction progresses. [99] The continuous flow spray drying process was used to prepare spherical Zr-MOF microbeads. This method converts a flow of liquid (solution, suspension, or emulsion) into dried powder using a hot gas, which evaporates the solvent. [100] Recently, the spray-granulation method was used to prepare the CPO-27-Ni sphere, which implies using a pump to feed a slurry through a spray nozzle and using air as an atomizing agent. [101]

1.10.3. Monoliths

A monolith is a single-piece construction with porous material channels forming a continuous network. Monoliths have unique properties, such as high flow rate tolerance

and a wide range of surface chemistries, which make them useful for applications. In this sense, the monolithic structure represents an economical and viable alternative to immobilizing a MOF powder. [102,103]

One of the processes for producing MOF-monoliths is the conventional extrusion process; compared with other shaping methodologies, extrusion is a high-efficiency, continuous, and low-cost shaping technology. [104] The materials used in the MOF-monolith production process involve MOF, binders, and plasticizers (Fig. 7). In extrusion paste, a binding agent is necessary to ensure that the monolithic structure is mechanically stable. [105] MIL-101(Cr) and $Cu_3(BTC)_2$ are MOFs immobilized by the conventional extrusion process.

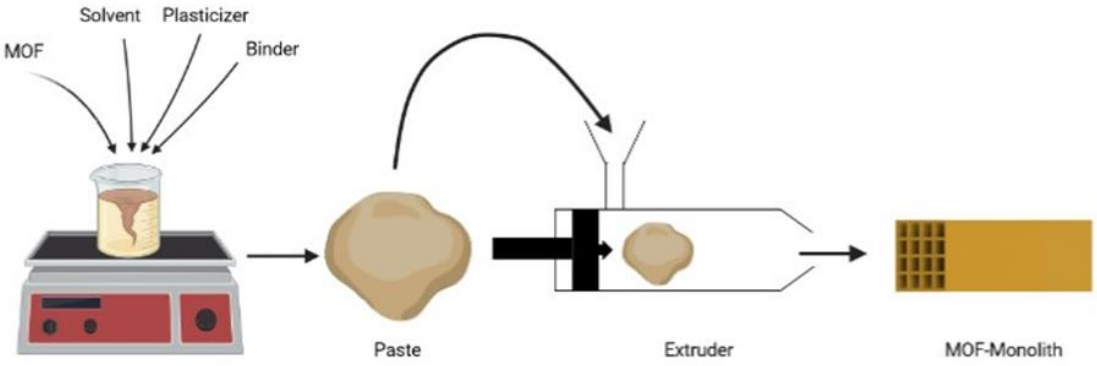

Fig. 7. Paste extrusion technique to obtain MOF-monoliths. [105]

Growing MOF crystals into hollow structures is another approach to shaping MOF. An example of increasing MOF crystals in cordierite monolith was carried out by Lawson et al. (2017) using MOF-74(Ni) and UTSA-16 (Co); in this case, the amount of MOF was near 76% and 80%, respectively, but the total specific area was lower 20% and 30% compared with MOF powder (Fig. 8).[106]

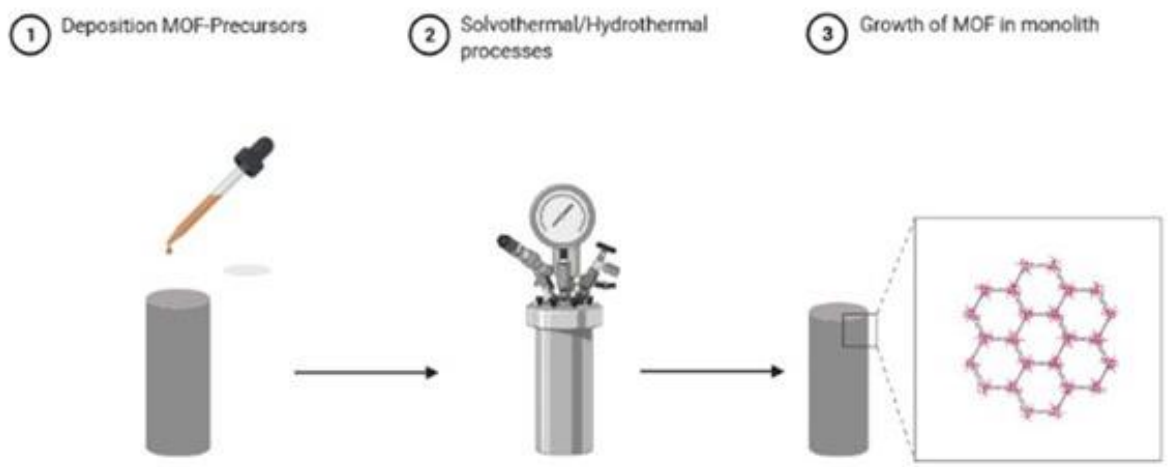

Fig. 8. MOF's growth in a monolith.[107,106]

Also, MOF-monoliths can be formed by a mechanical procedure which is a process where a loose material becomes more cohesive as the applied pressure rises. MOF-177 monoliths with varying densities were formed from powdered bulk samples. A known amount of MOF (50–100 mg) was placed in a cylindrical die, then sealed with a stainless-steel dowel. After the assembly, the material was manually compressed until a density was achieved; the force required was estimated between 0-10 ton cm^{-2}, and no organic solvent or water was used. [108]

It's relevant to analyze the differences between powder and monolith samples first to confirm the immobilization of MOF into monolith structure and to demonstrate the formation of the MOF in the case of the growth of MOF material. [109] Frequently, in monoliths, the porosity of the adsorbent structure is linked to the total pore volume. Porosity is high in adsorbent monoliths with large total pore volumes.[110] Even though MOF-monolith presents a values reduction in textural properties compared to MOF

powder. Also, it is relevant that the material structure obtained shows mechanical stability due to different applications like adsorption, storage, or catalysis. The binder effect is also visible in mechanical properties; a high amount of bentonite clay in MOF-monolith represents a fracture-resistant monolithic form.[105] MOF-monoliths have been evaluated for greenhouse gas capture, such as CO_2; Lawson et al. (2017) presented coated MOF monolith; it showed a CO_2 adsorption capacity of 2.5 and 1.6 mmol g^{-1} at 1 bar and room temperature, respectively, the amount of MOF was about 76 wt% and 80 wt%. [106]

1.10.4. 3D printed Monoliths

Additive manufacturing can be applied to produce complex structures such as lattices and porous scaffolds; in this sense, the three-dimensional (3D) printing technique has been used to build various high-resolution architectures from digital models. Moreover, 3D printing has different applications, like extruding other materials into shapes for biomedicine, reactors, and environmental processes. As a result, it appears to be a promising method for immobilizing MOF powders into monoliths. One of the first studies that applied 3D technology was developed by Thakkar et al. (2017), which used a 3D printing technique to immobilize MOF-74(Ni) and UTSA-16(Co).[111] The paste composition consisted of 80%-85% MOF, 10-15% bentonite, and 5% PVA as a plasticizer (Fig. 9). The paste was located in a syringe and extruded from a nozzle. As a result, MOF-monoliths structures presented a 1.5 cm height and 1.5 cm diameter with some reduction in the specific surface areas compared with MOF powder.

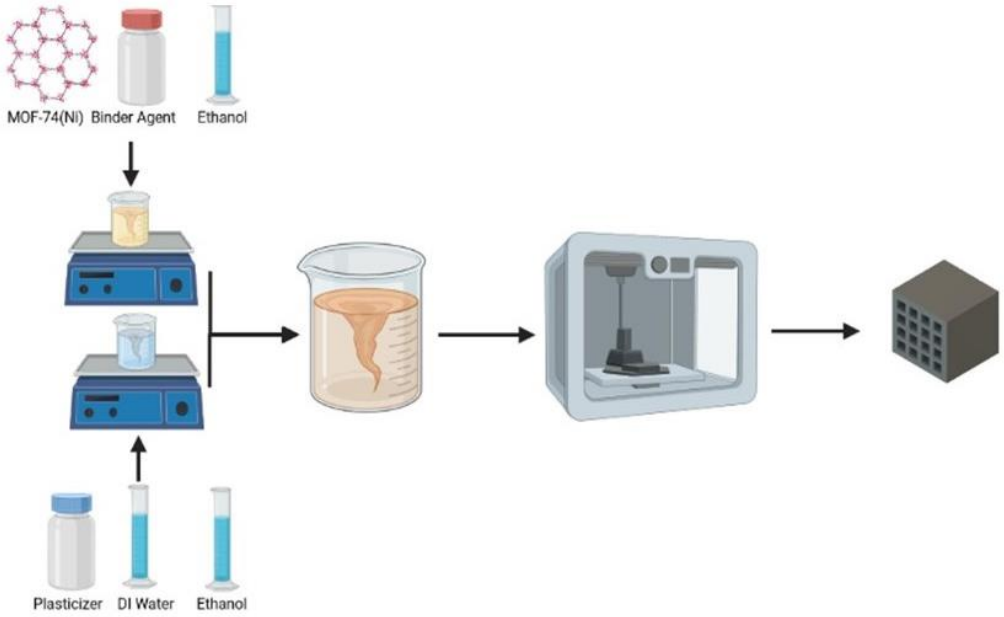

Fig. 9. 3D-Printing of a MOF-monolith using a paste based on a binder and plasticizer.[111]

N_2 physisorption measurements are commonly carried out to evaluate the textural properties of the MOF-monoliths and compare them with the MOF powders. MOF-74(Ni) monolith exhibited a reduction in the surface area by near of 38% compared to MOF-74(Ni) powder (1180 m^2/g), which can be a consequence of the presence of additives in the paste; the pore structure of MOF-monolith was similar to the MOF powder with pores in the range of 1-4 nm. Similarly, in the study presented by Lefevere et al. (2019) was observed a decrease near 20% in pore volume and surface area.[112] In the case of the investigation of Bible et al. (2018), conventional filament ABS was combined with ZIF-8 and HKUST-1 to produce MOF filament. The surface areas of the MOF-filaments were reduced at 435 and 329 m^2/g for ABS-ZIF-8 and ABS-HKUST-1 filaments, respectively, compared to surface areas of pure MOF powders, ZIF-8 (1446 m^2/g), and HKUST-1 (776 m^2/g). [113]

Another essential characteristic is mechanical stability; in the study carried out by Kreider et al. (2018) about ABS-MOF filaments, the incorporation of MOF-5 into the polymer reinforces the mechanical properties of the composite compared to pure polymer. The amount of MOF in a paste contributes to the mechanical stability of the monolith; Thakkar et al. (2017) established that the maximum MOF content they could use was 80-85% wt., elevated ratios caused the monoliths did not present enough mechanical strength.[111]

.

2. Literature Review

VOCs are a prime environmental problem, with increasing air pollution leading to lung and heart-related issues.[114] The conventional adsorbents for removing air pollutants are activated carbon and zeolites.[115] Even though the pore characteristics (diameter and geometry) that zeolites and activated carbon present are unsuitable for the adsorption of different VOCs.[116] Therefore, it's necessary to create materials that present better characteristics (pore size, surface area, and host/guest interactions) for VOC adsorption. On the other hand, MOFs are a recent class of porous materials with large pore sizes and uniform structures. Several of these structures have been applied to air purification; examples are MIL-101(Cr), MIL-53, MIL-125, CPM-5, MOF-177, and UIO-66. [117–119]

The studies using MOF to remove VOCs from the air have increased in the last decade. Among the different types of MOF, MIL-101(Cr) shows essential properties for removing polluting gases from the air, such as high specific area and active metal sites available for adsorption. [26,120,121] Zhao et al. (2011) compared carbon materials, zeolites, and MIL-101(Cr) in the adsorption of benzene in the air.[122] The MOF sample showed an extra-large surface area (BET 3054 $m^2 g^{-1}$) and large pore volume (2.01 $cm^3 g^{-1}$). Meanwhile, π-π interaction can be formed by benzene molecules and benzene rings in the linker for the MIL-101(Cr) when benzene is adsorbed, which is stronger than the C-π and O-π interactions between benzene molecules and carbon materials or zeolites, which improved adsorption capacity of benzene in MIL-101(Cr). Yang et al. (2011) showed the effective adsorption of VOCs on MIL-101(Cr) and the influence of VOC molecular size

and shape on adsorption capacity. The BET method (3980 m^2 g^{-1}) and Langmuir method (5870 m^2 g^{-1}) found the specific surface area. The total pore volume was estimated to be 1.85 cm^3 g^{-1}.[120] On the other hand, the authors assumed that the quick diffusion of benzene and toluene into the pores of MIL-101(Cr) could be attributed to their smaller molecular sizes compared with the molecular sizes of acetone, ethylbenzene, and xylenes. They concluded that a pore-filling mechanism carries out the adsorption of VOCs by MIL-101(Cr). Also, the interaction between the organic linker in the MOF structure and toluene positively impacts adsorption capacity.[43]

The conventional synthesis was proposed by Ferey et al. (2005) using no-green reagents like hydrofluoric acid (HF), 1-4 benzene dicarboxylate (H_2BDC), and chromium nitrate ($Cr(NO_3)_3$).[123] After that, several researchers evaluated the modification of the conventional synthesis of MIL-101(Cr) on its physicochemical characteristics. Zhao et al. (2011) synthesized MIL-101(Cr), the MOF exhibited a high surface area of 4443 m^2 $g^{-1,}$ and its adsorption capacity of benzene was twice the value for zeolites (silicalite-1 and SBA-15), and 3-5 times higher than that of activated carbons (Ajax and ACF) under similar conditions.[124]

Instead of commercial BDC, several studies propose using poly(ethylene terephthalate) (PET), which contains BDC within its structure. Lo et al. (2016) presented PET as an initial precursor instead of terephthalic acid for synthesizing five MOFs based on terephthalate, within which MIL-101(Cr) is located.[50] This process offers an economically attractive strategy for eliminating waste PET while making value-added materials;

however, chromium nitrate and HF use persists. The literature search showed that there is no completely sustainable synthesis of MIL-101(Cr); it is intended to develop a synthesis using PET and without adding HF like modulator. No green metrics or LCA of MIL-101(Cr) synthesis was found.

To select a sustainable adsorbent, it's necessary to provide the cost of MOF synthesis routes. For example, Luo et al. (2021) applied Monte Carlo simulation to evaluate simulated production cost distributions for UiO-66-NH_2. [125] The economic analysis of the UiO-66-NH_2 production determined that an aqueous solution-based system is more economically feasible than the conventional solvothermal system. However, although the economic assessment was applied to select an ideal adsorbent, it is essential to get the point of view into the material's application, sustainable and economic impact. In this sense, no studies about a techno-economical environmental assessment of MIL-101(Cr) were observed in the literature.

Another important aspect of an ideal adsorbent material is that it must be immobilized into a stable structure for continuous adsorption processes. Therefore, a group of researchers investigated the fabrication of various adsorbent monoliths using the 3D printing technique and its subsequent use for removing air pollutants. The results revealed that the monoliths still have their physical properties, mechanical integrity, and similar adsorption capacities to the powder form. [126–128] In the studies about manufacturing monoliths through the 3D printing technique, the effect of mixture composition MOF-binder on the properties of the monolith is evaluated. An example of that is the research

of Lefevere et al. (2019) applied additive manufacturing to the synthesis of ZIF-8 monoliths for the adsorption of n-butanol from the air.[129] To observe the effect of binder, they formed two monoliths: one with 80 wt% ZIF-8 and 20 wt% bentonite and the other with 66.7 wt % ZIF-8, 16.7 wt% bentonite, and 16.7 wt% methylcellulose. The ZIF-8-bentonite presented a saturation capacity of about 90% of the pure ZIF-8 powder. However, for the second monolith, the saturation capacity dropped to around 70% compared to the pure powder; the authors expressed that the decrease in saturation corresponds to the total amount of organic e inorganic binder present in the sample. Based on the literature reviewed, it was observed that MIL-101(Cr) monoliths obtained by 3D technology had not been obtained.

This work evaluates the economic and environmental impact of MIL-101(Cr) synthesis for toluene adsorption in indoor conditions, avoiding less corrosive materials and using residues of PET to obtain MOF material. Moreover, the immobilization of MOF in a monolith using 3D printing technology was analyzed in continuous adsorption processes.

3. General Objective

To synthesize and evaluate the use of MIL-101(Cr) monolith developed by 3D printing and green chemistry principles to reduce toluene in closed environments.

4. Specific Objectives

a) To develop a green MIL-101(Cr) synthesis and replace HF as a modulator with HNO_3, CH_3COOH, or H_2O.

b) To develop a techno-economic environmental assessment of MIL-101(Cr) synthesis.

c) To obtain the toluene isotherms and kinetics onto MIL-101(Cr).

d) To obtain a printable mixture of MOF-binder to 3D printed MIL-101(Cr) monolith.

e) To characterize MIL-101(Cr) monolith and compare its physicochemical properties with the MOF powder material.

f) To get breakthrough curves of toluene using MIL-101(Cr) powder and monolith.

5. Hypothesis

From a green synthesis and additive manufacturing based on 3D printing, a MIL-101(Cr) monolith can be obtained to remove toluene as a model molecule of VOCs.

6. Scientific Contribution

The results of this research will present a synthesis of MIL-101(Cr) that contributes to the 3rd, 5th, and 7th principles of green chemistry, using PET residues and less toxic modulators such as HNO_3 and CH_3COOH instead of HF. Additionally, a methodology to analyze the techno-economic environmental impact of a MOF will be presented. In addition, this study will provide a method of obtaining a 3D-printed monolith that can remove VOCs in indoor environments.

7. Materials and Methods

7.1 MIL-101(Cr) Synthesis

The MIL-101(Cr) synthesis was carried out with variations as described by Alivand et al.[130] A mix of HBDC (2 g) and $Cr(NO_3)_3 \cdot 9H_2O$ (4 g) was dissolved in DI water (48 mL) using sonication for 30 min; in the case of modulator used HNO_3 (10 mmol), CH_3COOH (10 mmol) and without any substance. The reaction was carried out in a Teflon autoclave at 215 °C for 8 h. After cooling, the product was treated with hot DMF, ethanol, and water in a recirculation system for 4 h, and one sample only was treated with hot ethanol and water. Finally, the green powder was separated by centrifugation and drying at 110°C for 12 h.

To obtain MIL-101(Cr) from PET, bottles were recollected, washed, and cut into small PET flakes. 2 g of PET flakes, 4 g of $Cr(NO_3)_3 \cdot 9H_2O$, and 48 mL of DI water were ultrasonically mixed for 30 min. The same reaction conditions, modulators, and type of purification were applied as in the previous synthesis. Finally, the resulting green solid was dried in an oven at 110 °C overnight to obtain MIL-101(Cr). All syntheses are resumed in Table 1. To evaluate the BDC obtained from PET, the same reaction of MIL-101(Cr) production was applied without metallic salt and modulator; after that, the white product was washed with hot ethanol and dried at 100°C overnight.

Table 1. Synthesis of MIL-101(Cr)

MIL-101(Cr)	Modulator	Source BDC	Purification
M-1	H_2O	H_2BDC-C	EtOH- H_2O
M-2	H_2O	H_2BDC-C	DMF-EtOH- H_2O
M-3	CH_3COOH	H_2BDC-C	DMF-EtOH-H_2O
M-4	HNO_3	H_2BDC-C	DMF-EtOH- H_2O
M-5	HNO_3	H_2BDC-PET	DMF-EtOH-H_2O
M-6	CH_3COOH	H_2BDC-PET	DMF-EtOH-H_2O
M-7	H_2O	H_2BDC-PET	EtOH-H_2O

7.2 MIL-101(Cr)-Monoliths

The 3D-printed MIL-101(Cr) monoliths were fabricated following two paste solution-base procedures. Briefly, 2 g of carboxymethyl cellulose (CMC) was dissolved in 100 mL for 24 h to obtain the organic binder; the paste a solution was prepared by dissolving MIL-101(Cr) green powders (95%wt) and CMC (5%), a small quantify of deionized water was added to obtain an extrudable paste. The second solution was obtained using a mix of 95%wt MIL-101(Cr) powders and 5%wt kaolin clay. To get a homogenous solution, 1.25 mL of deionized water and ethylene glycol was added to 1 gr of the mix before described. Finally, both pastes were mixed at 2500 rpm for 10 minutes using an IKA RW20 mixer.

Monolith dimensions were designed using Fusion 360 software: a diameter of 1.8 cm and 1 cm of height. The monolith model was saved as an STL file and exported to CURA software: monolith configuration was a honeycomb with 35% infill, 5 mm s^{-1} of velocity

printing, and 3 mm of layer height. After being printed, the monolith was dried at ambient temperature and then moved to an oven at 45°C overnight.

7.3 Characterization

Different techniques evaluated MOF physical and chemical characterizations; Scanning electron microscopy (SEM) images were obtained using a JEOL JSM-6490LV microscope with acceleration voltage from 0.3 to 30 kV and a thermionic electron gun with W filament. The functional groups of MIL-101(Cr) were analyzed by Fourier transform infrared spectrometer (FTIR, Alpha II) equipped with a diamond ATR accessory, the spectra from 4000 to 400 cm^{-1} with a spectral resolution of 2 cm^{-1} (Bruker, Germany). The BET surface area (S_{BET}) and pore volume (V_{pore}) of MIL-101(Cr) products were obtained from the N_2 adsorption isotherm at 77 K using a Micromeritics ASAP 2020 after out-gassing the material at 150 °C for 8 h under vacuum.

Powder X-ray diffraction (PXRD) patterns of green MOF powder were collected in Bragg-Brentano geometry with Cu-K_α radiation (λ = 1.541830 Å) in an Ultima IV diffractometer. The powder patterns were recorded from 3 to 40° (2θ) in 0.02° steps and 10° min^{-1} scan speed. In addition, ^{1}H and ^{13}C nuclear magnetic resonance (NMR) spectroscopy was applied at 25 ± 0.5 °C using a Bruker Avance-400 spectrometer operating at 400.01 and 100 MHz, respectively. The X-ray photoelectron spectroscopy (XPS) characterization of MIL-101(Cr) samples was performed in a Thermo-Scientific, K-Alpha spectrometer with monochromatized AlKα radiation (E = 1.5 keV). Accordingly, the C1s, O1s, and Cr2p

spectra were recorded to elucidate the chemical state of elements in M4 and M8. These spectra were deconvoluted and fitted using a Gaussian approach in the PeakFitV4.12 software. For rheology characterization of MIL-101(Cr) paste, the experimental conditions were 25°C in a dual 40 mm Peltier plate; the apparent viscosity was determined as a function of shear rate at a constant frequency 6.283 rad s^{-1}. For analysis of stepped deformation, measurements were measured in oscillatory mode using an angular frequency of 0.1 rad s^{-1}.

7.4 Adsorption Isotherms

The experiments were carried out at 3, 5, 7, 8, and 10 ppm of toluene, and 0.25 g L^{-1} adsorbent doses were used; the experiment was carried out at room temperature. The powder materials were put on 20 mL vials with glass wool after a volume of VOC was injected, and the vial was kept for 2 h to ensure equilibrium.

The samples were tested for toluene concentration using gas chromatography during the adsorption experiments. To test the concentration of VOC, each sample was injected into a Shimadzu Nexis GC-2030 gas chromatograph with a flame ionization detector (FID). The capillary column was a Shimadzu SH-Rxi-5ms (15 m x 0.25 mm inner diameter x 0.25 m film thickness). The column, injector, and detector temperatures were set to 70, 200, and 250°C, respectively. Helium was used as the carrier gas, with a flow rate of 0.7 mL/min and a pressure of 54 kPa. With split radio 1.0, the injection volume was 0.5 mL,

which took 2.5 minutes. The experiments were realized in triplicate. The adsorption capacity was calculated using the following equation:

$$q = \frac{(\mathrm{C_o} - C)\mathrm{V}}{\mathrm{m}} \qquad \text{Eq. 10}$$

Where q represents the adsorption capacity (mg g^{-1}), C_o represents the VOC initial concentration (mg m^{-3}), C represents the VOC concentration over time (mg m^{-3}), V represents the volume (m^3), and m represents the adsorbent mass (g).

7.5 Adsorption Kinetics

The adsorption kinetics experiments were carried out at 2 ppm of toluene. 40 mg of adsorbent powder material was used, and the experiment was conducted at room temperature. After a volume of VOC was injected, the powder materials were put on 20 mL vials with glass wool. The same chromatography conditions described before were used to evaluate the adsorption kinetics. The experiments were realized in triplicate, and every 2 min sample was injected to evaluate the concentration. The adsorption capacity was calculated using Eq. 10. The PFO and PSO models were fitted to the experimental data.

7.6 Adsorption in Dynamic Systems

The adsorption of toluene in the vapor phase was studied using liquid toluene from J.T Baker company. The initial and final concentrations of the vapors generated were determined using a photo ionization 0.4 detector (photo check tiger). For adsorption

experiments, a MOF powder material (0.37 g) was packed inside a polypropylene column with a volume of 22.9 cm^3, the height and diameter of column were 9 cm and 1.8 cm, respectively. The initial concentration was 250 ppm and the feed flow 250 mL min^{-1}. The concentration of VOC was generated by inlet air through a saturator containing VOC placed in a refrigerant bath at 15 ºC. This temperature was maintained constant recirculating water with the help of a peristaltic pump and a thermostatic bath; the effluent was diluted with air choosing the required air flow rate to get 250 ppm of VOC. Flow rate of the column vapor inlet was controlled with a mass flow controller and the adsorption temperature was 40º C. The graphical representation of the outlet concentration of VOC versus time is the breakthrough curve and the VOC adsorption capacity (mg VOC g^{-1} MOF powder) was obtained by numerical integration of the breakthrough curves using the following equation:

$$q_t = \frac{QM_T}{W_m V}\left(C_0 * t_s - \int_0^t C dt\right) \qquad \text{Eq. (11)}$$

where q_t is the adsorption capacity (mg g^{-1}), W_m is the mass of monolith (mg), C_0 and C represents the VOC initial concentration and the concentration over time (mg m^{-3}) respectively, T_s is the time (min), V is the volume of solution (mL $mmol^{-1}$), M_T is the molecular weight of toluene (mg $mmol^{-1}$).

7.7 Principles of Green Chemistry

DOZN™ 2.0 was applied to evaluate the impact of MIL-101(Cr) production considering time, synthesis steps, solvents, and waste generation. The values (temperature, time, and solvent exchange step) used in the DOZN™ 2.0 tool to obtain the green score are

obtained from the synthesis routes. The properties of chemicals were recollected using the UN's Globally Harmonized System of Classification and Labelling of Chemicals (GHS). Millipore Sigma established and tested the green evaluator software based on the 12 Green Chemistry Principles and the equations that were previously published. [131] DOZN^{TM} 2.0 does not include the initial materials' life cycle impacts but contemplates the materials' risk of use and profitable consumption.

7.8 Life Cycle Assessment for MIL-101(Cr) Powders

7.8.1. Goal and Scope

The LCA of the MOF synthesis was performed following ISO 14044.[132] Five steps are included in the system boundaries to synthesize MIL-101(Cr): PET cleaning, ultrasonic mixing, hydrothermal reaction, solvent exchange, and drying. The environmental impacts related to the construction laboratory were not assessed to preserve consistency with prior LCA studies on the manufacture of adsorbent materials on a laboratory scale. [82,125]

Each of the different MIL-101(Cr) synthesis strategies was considered as a study scenario:

• Scenarios M1, M2, M3, and M4: include the stages of mixing, hydrothermal reaction, solvent exchange, and drying.

• Scenarios M5, M6, and M7: consider PET cleaning, ultrasonic mixing, hydrothermal reaction, solvent exchange, and drying.

According to prior LCA studies on the manufacturing of adsorbent materials (activated carbon, MOF-74, and DUT-4),[133–135] the functional unit (FU) was set as 1 g of MIL-101(Cr) manufactured on a laboratory scale. Fig. 10 shows the system boundaries of MIL-101(Cr) production.

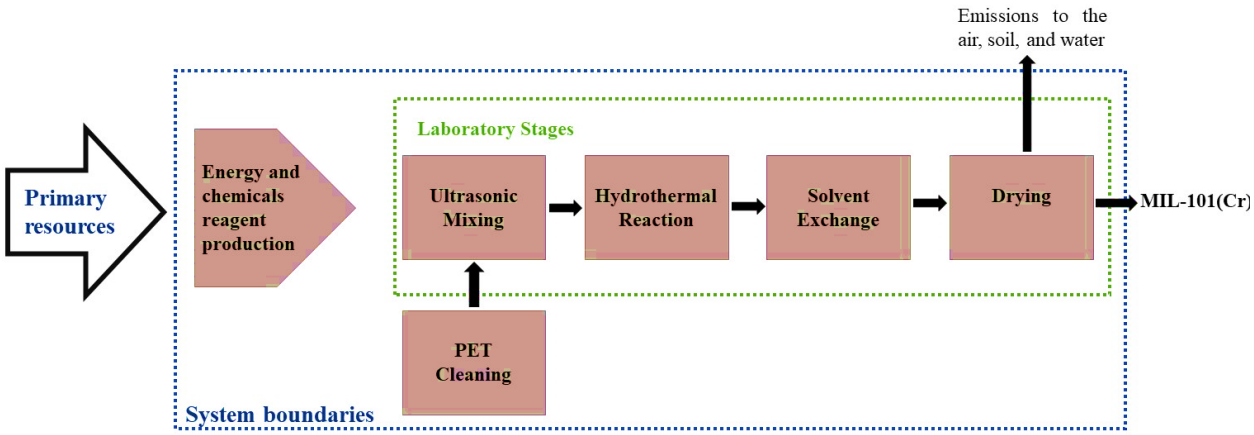

Fig. 10. System boundaries to produce MIL-101(Cr).

The information on the life cycle inventory (LCI) of chemical precursors and energy used in the MIL-101(Cr) production scenarios was obtained from the laboratory data, analytical procedures, and material-energy balances.

The production of energy and chemical reagents needed to synthesize MIL-101(Cr) was considered inside the system boundaries (Fig. 10). The LCI for these resources was taken from the Ecoinvent v3.3 database. However, the life cycle impact data for Chromium Nitrate Nonahydrate ($Cr(NO_3)_3$ $9H_2O$) is unavailable in the Econivent v3.6 database. Therefore, the production of the metal precursor was included in the process description

to calculate their life cycle impact data. Fig. 11 describes the reaction steps to obtain the $Cr(NO_3)_3\ 9H_2O$. A description of process and energy requirements for $Cr(NO_3)_3\ 9H_2O$ is described in Appendix A.

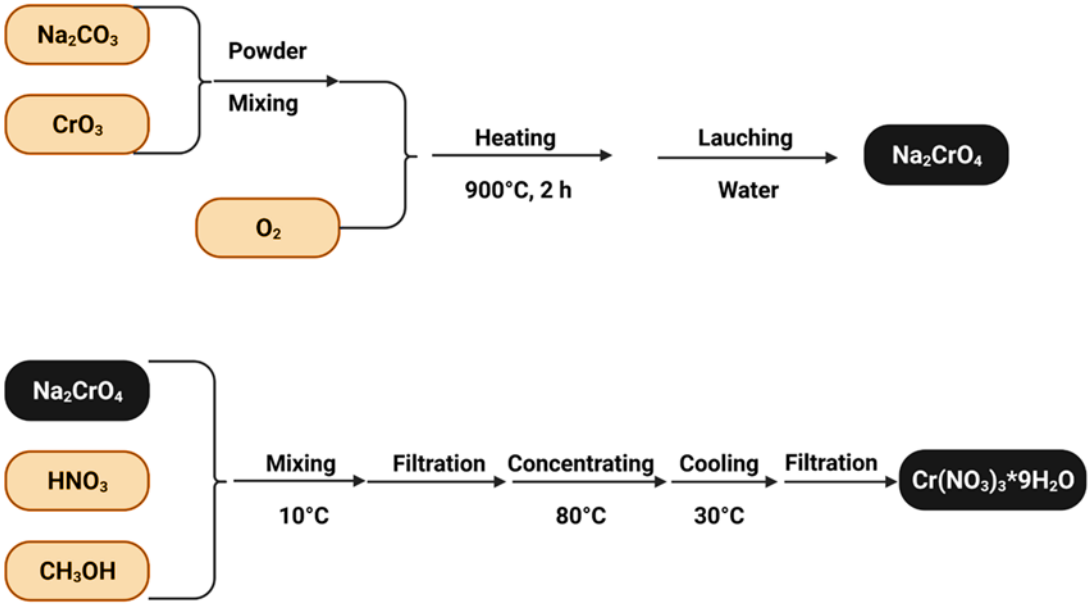

Fig. 11. Process to obtain Cr $(NO_3)_3\ 9H_2O$.

The MIL-101(Cr) synthesis required energy at every production stage; in this sense, the power necessary was obtained by energy balance. On the other hand, PET cleaning did not involve input energy due to the drying of PET flasks was an environmental temperature.

The energy balance corresponding to ultrasonic mixing was evaluated with Eq. 12. Specific energy (E_s) wasted in the stage of ultrasonic was calculated by the potence (P) of the equipment, time (t), volume (V), and concentration of total solids (Ts_0).

$$Es = \frac{P\ t}{V\ Ts_o} \qquad \text{Eq. 12}$$

The energy balance in the autoclave was evaluated using Eq. 13 as in previous reports[82]. The first part of the equation ($\mathrm{m}_1 \int_{\mathrm{Te}}^{\mathrm{Tw}} \mathrm{Cp}_{mix}\mathrm{dT}$) related to sensible heat was evaluated with mass fraction, boiling point, and specific heat capacity of each chemical reactant involved in the synthesis. The two following terms ($\mathrm{m}_2 \int_{\mathrm{Te}}^{\mathrm{Tw}} \mathrm{Cp}_{\mathrm{tf}}\,\mathrm{dT}$, $\mathrm{m}_3 \int_{\mathrm{Te}}^{\mathrm{Tw}} \mathrm{Cp}_{\mathrm{ss}}\,\mathrm{dT}$) corresponding to Teflon and stainless steel (autoclave) heating were obtained based on their specific heat capacity.

$$E = m_1 \int_{Te}^{T_w} Cp_{mix}dT + m_2 \int_{Te}^{Tw} Cp_{tf}\,dT + \; m_3 \int_{Te}^{Tw} Cp_{ss}\,dT \qquad \text{Eq. 13}$$

Table 2 resumed the variables and values used in the hydrothermal synthesis of MIL-101(Cr) energy balance.

Table 2: Value of each variable and parameters used for the energy balance in the solvothermal reactor.

Variable	Description/unit	Value
$\mathbf{m_1}$	Fluid mass (g)	52.5
$\mathbf{m_2}$	Stainless steel mass of autoclave (g)	4600
$\mathbf{m_3}$	Teflon liner mass of autoclave (g)	403
$\mathbf{T_w}$	Work temperature (ºC)	215
$\mathbf{T_e}$	Environmental temperature (ºC)	25
$\mathbf{Cp_{mix}}$	Fluid specific heat (J $g^{-1}\cdot K^{-1}$)	3.83
$\mathbf{Cp_{ss}}$	Stainless steel specific heat (J $g^{-1}\cdot K^{-1}$)	0.5
$\mathbf{Cp_{tf}}$	Teflon liner specific heat (J $g^{-1}\cdot K^{-1}$)	1.0

The centrifugation stage considers the cleaning using all solvents in some syntheses (M2-M6), another only ethanol and water (M1 and M7). The rotational kinetic energy equation Eq. 14 calculated the energy needed in the present centrifugation stage:

$$E_{cr} = \frac{1}{2} * m * r^2 * (2\pi f)^2 * f_r \qquad \text{Eq. 14}$$

Where *r* is the rotor radius (0.068 m), *f* is the frequency (166.667 s^{-1}), *m* is the mass to centrifuge (51-53 g), and f_r is the friction factor (1.45). The wastewater due to the cleaning stage was discarded according to our laboratory's hazardous waste management program. Therefore, the environmental impacts of the final disposal of this waste were not considered in the LCI, as reported by previous reports. [136]

After separation, the energy necessary to evaluate solvent exchange was obtained by the following equations.

$$\Delta H = m \int_{25°C}^{80\,°C} Cpmix dT \qquad \text{Eq.15}$$

$$Q = UA \int_{25°C}^{80°C} dT \qquad \text{Eq.16}$$

$$E_{se} = \Delta H + Q \qquad \text{Eq.17}$$

Where m is the mass (g), Cpmix is specific heat capacity (J g^{-1} $°K^{-1}$), U is the heat coefficient of transfer Pyrex glass (11.6 W m^{-2} $°K^{-1}$), and A is the flask area (0.001 m^2).

The energy required (Eq. 18) in the drying stage was obtained by calculating the heat energy needed to remove the solvent per unit mass of MIL-101(Cr). The energy balance for this stage was taken by previous reports like Sepúlveda-Cervantes et al. [27]

$$\frac{q_T}{m_s} = C_{ps}(T_{sb} - T_{sa}) + X_a C_{pL}(T_v - T_{sa}) + (X_a - X_b)\lambda + X_b C_{pL}(T_{sb} - T_v) + (X_a - X_b)C_{pV}(T_{va} - T_v) \quad \text{Eq. 18}$$

Where q_T/m_s is the amount of heat transferred per unit mass of solids (J g^{-1}), C_{ps}, $C_{pL,}$ and C_{pV} are the solid-specific heat, the liquid-specific heat, and the steam-specific heat, respectively (J $g^{-1}\cdot K^{-1}$). T_{sb} and T_{sa} are the final temperatures of the solids and the feed temperature, respectively (K). X_a and X_b are dry solids' initial and final mass per unit. T_v y T_{va} is the vaporization temperature and the final vapor temperature (K), and λ is the latent heat of vaporization (J g^{-1}).

The LCI was carried out following an attributional approach. This viewpoint attempts to measure the environmental consequences of the manufacturing process. It is focused on assessing the emission of products, and resource flows as it passes through their life cycle, using representative average data for all processes and input and output flows. To evaluate the LCA, the software SimaPro 7.3.3; the LCA was used to take a count of the ReCiPe 2016 method, considering midpoint and endpoint indicators. [137,138]

7.9 Economic Assessment

The lab-scale synthesis cost of producing 1 g of MIL-101(Cr) powder was divided into capital (*CC*) and operation costs (*OC*) (Eq. 19).

$$Synthesis\ Cost\ MIL-101(Cr) = OC + CC \qquad \text{Eq. 19}$$

7.9.1. Capital Cost

According to previous similar research reports, construction and equipment procurement are included in capital costs; laboratory construction was not included in capital costs due to regional variability. As a Mexican Norm regulates, the equipment's usefulness was determined as five years. [139] Some assumptions must be applied because the focus is a lab-scale production of MIL-101(Cr); the laboratory equipment, such as an oven or reactor, was analyzed at a laboratory scale, meaning a small capacity. The cost of equipment needed for MOF production is observed in Appendix B.

7.9.2. Operation Cost

The energy, raw materials, and chemical reagent requirements for MIL-101(Cr) synthesis are included in the operation cost. A list of chemical suppliers was registered and compiled to determine a raw material distribution; the cost of chemicals was obtained in kg and g; the price data were gathered from several chemical suppliers' internet pages such as Molbase.com or Mexican suppliers (CTRscientific.com). The raw material cost distribution (triangular, exponential, and normal) was analyzed by MINITAB 19™. The energy consumed in MIL-101(Cr) was obtained from inventory data for each scenario (M1-M7). The electricity cost was considered in the north of Mexico as 0.047 USD kWh^{-1}.

The mean cost of synthesis routes was obtained using a Monte Carlo simulation. Every variable was introduced with its defined distribution; the simulation was carried out in 30,000 trials, showing the probability cost of production of 1 g of MIL-101(Cr).

Finally, A Monte Carlo simulation (30,000 trials) was carried out to show the probability cost distributions of the synthesized 1 g of MIL-101(Cr). Simular™ software was applied to account for the variability associated with the market cost of raw materials price and equipment cost; every variable was introduced with its defined distribution.

7.10 Selection of ideal MIL-101(Cr) Scenario

TOPSIS (Technique for Order of Preference by Similarity to Ideal Solution) method has been applied to select the ideal adsorbent based on some criteria.[140] In the present study, there are seven alternative scenarios (i=1,2…,7) of MIL-101(Cr) production. Each scenario was evaluated in three criteria: environmental impact, synthesis cost, and VOC adsorption capacity (j=1,2,3). The TOPSIS method was applied to determine the ideal MIL-101(Cr) scenario choice; the process can be explained in the following steps. [140–142]

Step 1: Determine the normalized performance ratings. The vector normalization process creates a comparison across attributes easier with dimensionless units.

$$r_{ij}(x) = \frac{x_{ij}}{\sqrt{\sum_{i=1}^{7} x_{ij}^2}} \qquad \text{Eq. 20}$$

Step 2: Obtain the weighted normalized decision matrix. The related weight of each criterion (environmental impact, synthesis cost, and toluene adsorption capacity) equals one (*w*=1).

$$v_{ij=}r_{ij}(x) * w_j \qquad \text{Eq. 21}$$

Step 3: Find positive and negative ideal solutions. The PIS (positive ideal solution) and the NIS (negative ideal solution) are determined by the criteria; for example, PIS for environmental impact was related to the minor negative effect of MIL-101(Cr). Meanwhile, PIS for adsorption capacity was obtained for the higher value of toluene adsorption capacity presented by the particular scenario. PIS and NIS were detected using the following equations.

$$PIS = A^+ = \{v_1^+(x), \dots, v_7^+(x)\} = \left\{\left(\underset{i}{max} v_{ij}(x) \middle| j \in J_1\right), \left(\underset{i}{min} v_{ij}(x) \middle| j \in J_2\right)\right\} \qquad \text{Eq. 22}$$

$$NIS = A^- = \{v_1^-(x), \dots, v_7^-(x)\} = \left\{\left(\underset{i}{min} v_{ij}(x) \middle| j \in J_1\right), \left(\underset{i}{max} v_{ij}(x) \middle| j \in J_2\right)\right\} \qquad \text{Eq. 23}$$

Step 4: Evaluate the separation values. The distance of each scenario rating from the PIS and NIS is obtained by applying the Euclidean distance theory. Eq. 24 and Eq. 25 describe the process of obtaining the positive (ED_k^+) and negative (ED_k^-) separation values.

$$ED_k^+ = \sqrt{\sum_{i=1}^{7}\left[v_{ij}(x) - v_i^+(x)\right]^2} \qquad \text{Eq. (24)}$$

$$ED_k^- = \sqrt{\sum_{i=1}^{7}\left[v_{ij}(x) - v_i^-(x)\right]^2} \qquad \text{Eq. (25)}$$

Step 5: Calculate the overall preference score. The overall preference score (C_K) for each scenario is obtained as shown in Eq. 2. Scenarios are ranked based on higher C_K values. The best MIL-101(Cr) scenario is ubicated near 1; the worst scenario is near 0.

$$C_K = \frac{ED_k^+}{ED_k^+ + ED_k^-} \qquad \text{Eq. 26}$$

7.11 Disposal of the generated waste

Wastes generated during the development of this project were disposed of based on the current Safety and Environment Regulations of the Faculty of Chemical Sciences of the UANL.

8. Results and Discussion

8.1 BDC-PET Characterization

The same conditions of MIL-101(Cr) production were used to evaluate if BDC derived from PET was correctly obtained, avoiding modulator use. PXRD of BDC obtained from PET and from Sigma Aldrich are shown in Fig. 12. Similar reflections at 2θ = 17.34°, 25.14°, and 27.95° were detected in BDC-PET and BDC-Sigma Aldrich.

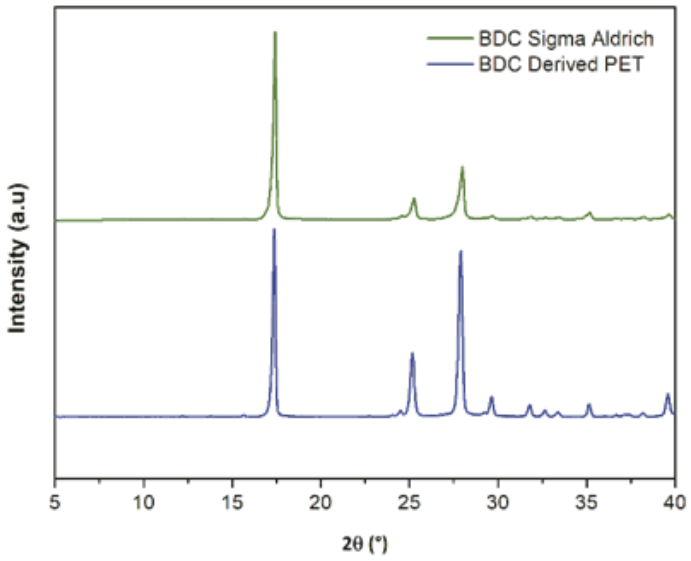

Fig. 12. PXRD pattern of BDC Sigma Aldrich and BDC-PET.

To determine the hydrolysis of PET flakes into BDC, the white material obtained was analyzed by NMR analysis; in this sense, both BDC, commercial and PET, were mixed using dimethyl sulfoxide-d6 (DMSO-d6). The ^{1}H and ^{13}C NMR spectra of the organic ligands are also shown in Fig.14. In the ^{1}H MNR spectrum, the BDC-PET present two intense resonance signals at 8.10 ppm and 13.33 ppm, and the same characteristic signals were found in commercial BDC, ^{1}H chemical shift corresponded well to the

resonance signal of H atoms on the aromatic ring of the BDC linker (Fig. 13a). Meanwhile, ^{13}C NMR spectrum of both BDC materials presents comparable patterns (Fig. 13b).

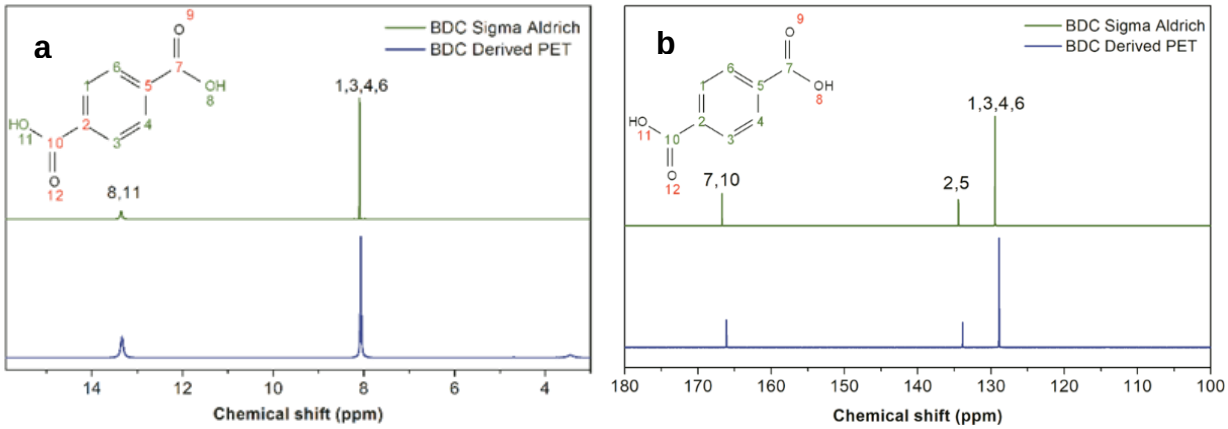

Fig. 13. a) ^{1}H NMR and b) ^{13}C NMR of BDC Sigma Aldrich and BDC derived PET.

8.2 MOF Characterization

8.2.1. X-Ray Diffraction (XRD)

The synthesized samples of MIL-101(Cr) was analyzed by XRD to verify its identity. The powder X-ray diffractograms of the MIL-101(Cr) samples matched to XRD patterns of simulated MIL-101(Cr) obtained from the Cambridge Structure Database (CSD), validating the similarity of the crystalline structure of MOF material (Fig. 14a and 14b). The diffraction peaks are coherent with previously reports of standard MIL-101(Cr). In fact, M2, M3, and M4 present a comparable intensity of the peaks, meanwhile the others MOF sample showed a weaker peak intensity, conceivably by residual impurities onto the MOF structure. M1 and M7 did not use DMF in the purification process; also, M5, M6, and M7, obtained BDC as organic linker for the synthesis from PET flasks, thus, the hydrolyzation reaction could be incomplete at the reaction time.

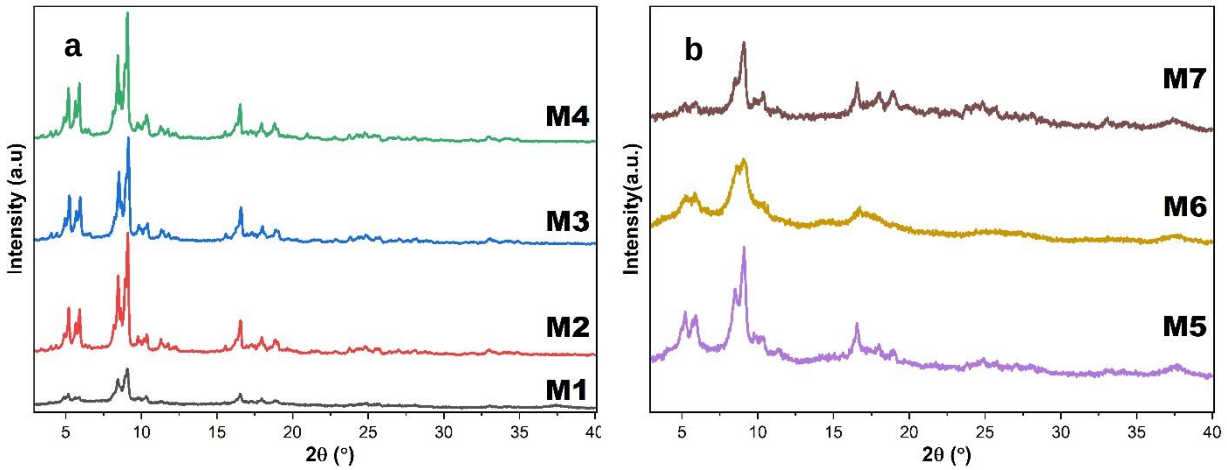

Fig. 14. a) PXRD patterns of MIL-101(Cr) M1-M4 and b) PXRD patterns MIL-101(Cr) M5-M7.

Furthermore, the particle size can be related to the broad Bragg reflections. In this sense, M5, M6, and M7 presents a smaller particle size (broader Bragg reflections) than first samples of MIL-101(Cr).

8.2.2. FT-IR spectra

The functional groups of MIL-101(Cr) surface were determined by FT-IR (Fig. 15). The characteristic peak at 570 cm^{-1} corresponding to the Cr-O vibration is observed, which indicates a connection between Cr and the carboxyl groups of the organic ligand. While the peaks between 600 and 1600 cm^{-1} are attributed to terephthalic acid and its aromatic rings; the peaks at 750, 880, 1016, and 1150 cm^{-1} correspond to the C-H vibration. The peak located near 1400 cm^{-1} is due to the symmetric O-C-O strain. The band indicated at the wavelength of 1517 cm^{-1} is related to the C=C tension. The peaks observed at values

of 1623 and 3400 cm^{-1} are characteristic of water molecules adsorbed inside the MOF. The results shown in the FTIR analysis are consistent with data already published.[143]

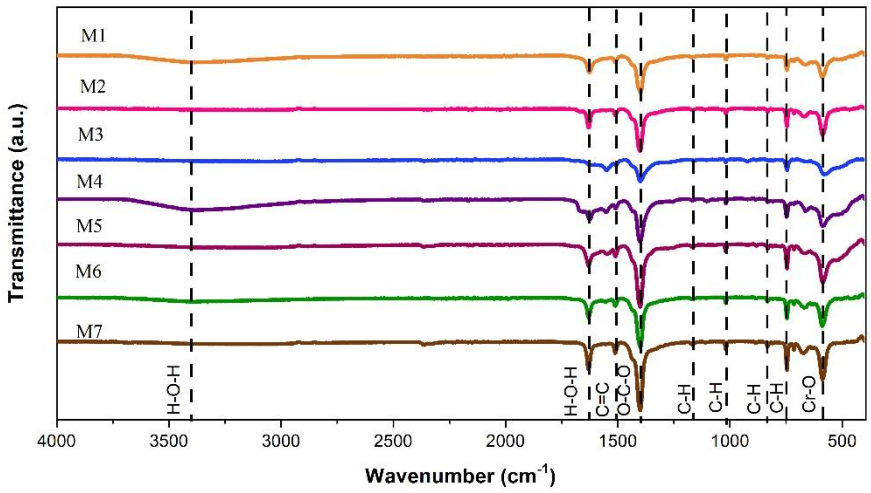

Fig. 15. FTIR spectra of MIL-101(Cr) samples.

8.2.3. XPS Analysis

The chemical state of Cr, O, and C present on M4 and M7 samples were analyzed by XPS. The emissions related to C and O are identified in Fig. 16a and Fig. 16b; the signals are attributed to the BDC ligand; a small peak observed of N is associated with DMF solvent. Moreover, we can also detect two signals related to Cr, according to Cr2p spectra obtained from these samples, appear at 577.2 and 587 eV, corresponding to core emissions from Cr2p3/2 and Cr2p1/2 states, which agree with those expected for Cr(III) linked to carboxylate moieties at BDC units.[144]

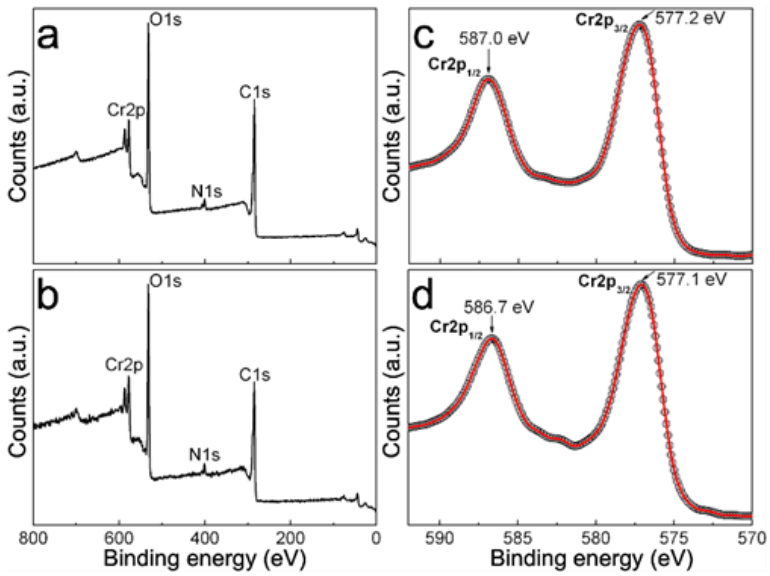

Fig. 16. Survey XPS spectra recorded for: (a) M4 and (b) M7. Cr2p spectra of samples: (c) M4 and (d) M7.

Meanwhile, the C1s and O1s spectra measured for the MOF sample are observed in Fig.17. The C1s spectra present four peaks at value of 284.6, 286.3-286.7, 288.5, and 291.5-291.4 eV attributed to photoelectrons emitted from C in C-C/C-H, C-O, O-C-O, and O=C-O bonds, respectively (see Fig. 17a and 17b).[145,146]

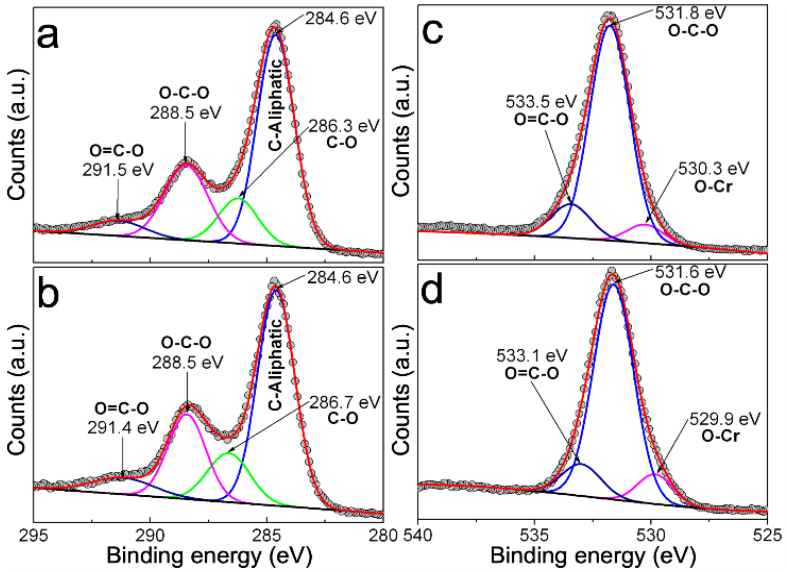

Fig. 17. C1s XPS spectra obtained for: (a) M4 and (b) M7; O1s XPS spectra for: (c) M4 and (d) M7.

Moreover, three peaks in the O1s spectra can be identified related to O in O-Cr, O-C-O, and O=C-O at 530.3-529.9, 531.8-531.6 and 533.5-533.1 eV,[146] (see Fig. 17c and 17d) These results are congruent with those obtained from FTIR measures and assure the formation of MIL-101(Cr) structure from either BDC reagent or PET molecules.

8.2.4. Textural properties

The textural properties of MOFs refer to the physical properties that describe the internal structure and surface area of the material. N_2 adsorption isotherm was used to obtain the BET surface area (S_{BET}) and pore volume (V_{pore}) of MIL-101(Cr) (Table 3). M4 presented a higher specific surface area (3432 $m^2\ g^{-1}$) compared with the other routes of synthesis presented in this work and similar values than previously reported.[147,148]

Table 3. Textural properties of MIL-101(Cr) M1-M7 and compared with previously reported.

MOF MIL-101(Cr)	BET Surface Area ($m^2\ g^{-1}$)	Pore Size (nm)	Pore Volume ($cm^3\ g^{-1}$)
M1	1782	2.93	1.01
M2	3053	2.07	1.57
M3	3072	2.24	1.54
M4	3432	2.44	1.67
M5	1791	3.26	1.46
M6	1385	6.47	1.24
M7	1852	3.18	1.04
MIL-101(Cr)[149]	2052	1.84	0.94
MIL-101(Cr)[150]	2397	1.34	1.13
MIL-101(Cr)[151]	4100		2.00

M2, M3, and M4 present similar values of specific surface area; in this sense, the use of DMF helps to eliminate the particulate of the organic linker that does not react and block the pores of MIL-101(Cr). Meanwhile, M1 presents a lower value than the other three MOFs; only hot ethanol and water were applied in the purification process.

Comparing the green materials, M5 to M7, the last one presented a higher value of BET surface area of 1852 $m^2 g^{-1}$, which was slightly lower than the previous report using waste PET bottles as a source of organic ligand,[152] is comparable to free-modulator hydrothermal synthesis. The textural properties differences between MIL-101(Cr) samples were expected because the use of acidic modulators enhances the porosity of MIL-101(Cr) and for an extra step of purification with DMF. [153]

8.2.5. Scanning electron microscopy (SEM)

Scanning electron microscopy (SEM) is one of the most widely used techniques to characterize MOF. The SEM images of all routes of MIL-101(Cr) synthesis were used to observe the morphology of MIL-101(Cr) (Fig. 18-Fig. 19). Although M1, M2, M3, and M4 (Fig. 18) only had the characteristic octahedral morphology previously reported,[154,155] while M5, M6, and M7 (Fig. 19) presented irregular morphology and agglomeration of crystals.

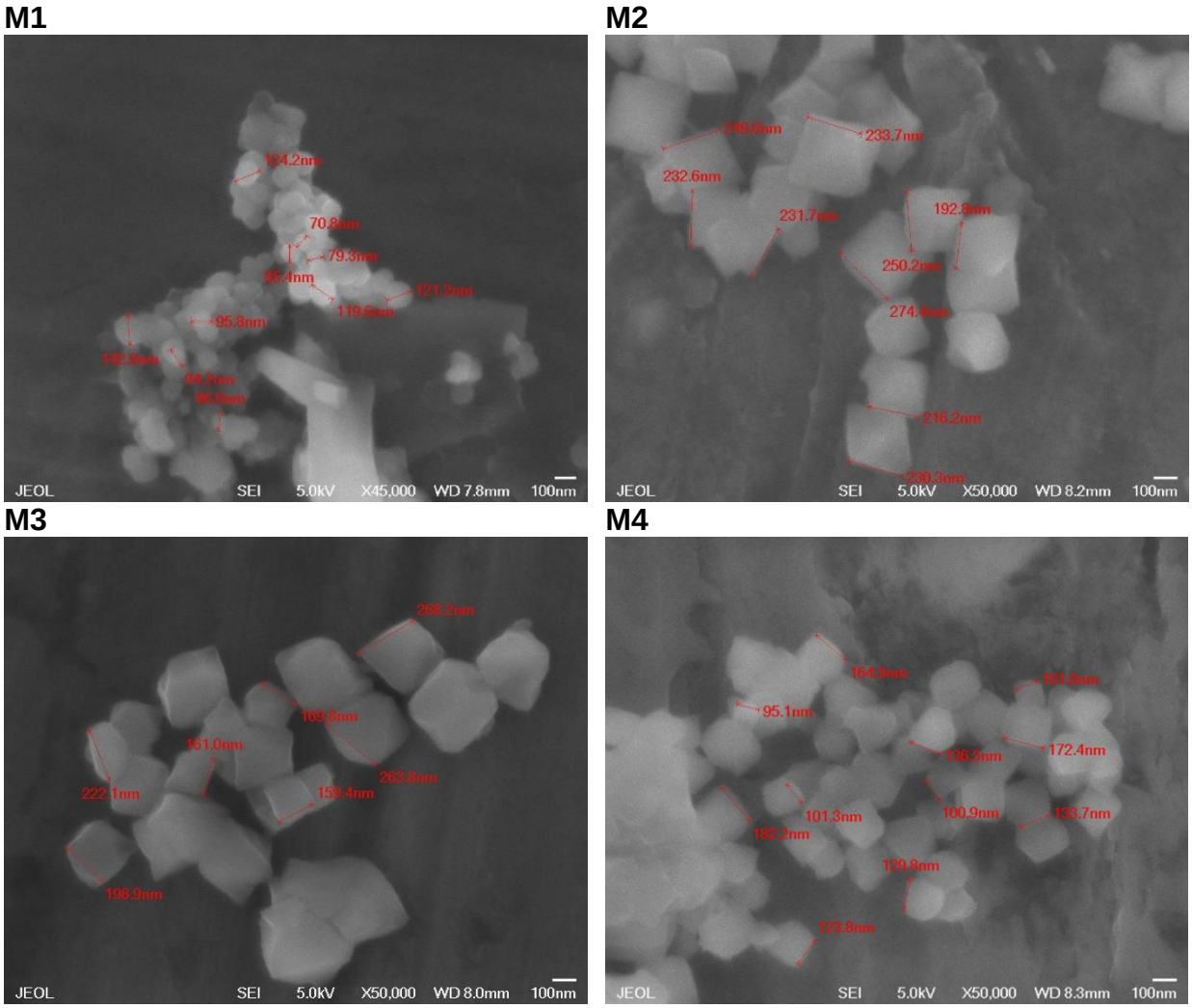

Fig. 18. SEM images of the MIL-101(Cr) M1 to M4.

The use of HNO_3 as a modulator helps obtain regular shape crystals without aggregation due to the moderate speed of nucleation; moreover, PET flasks directly affect the morphology of MOF.

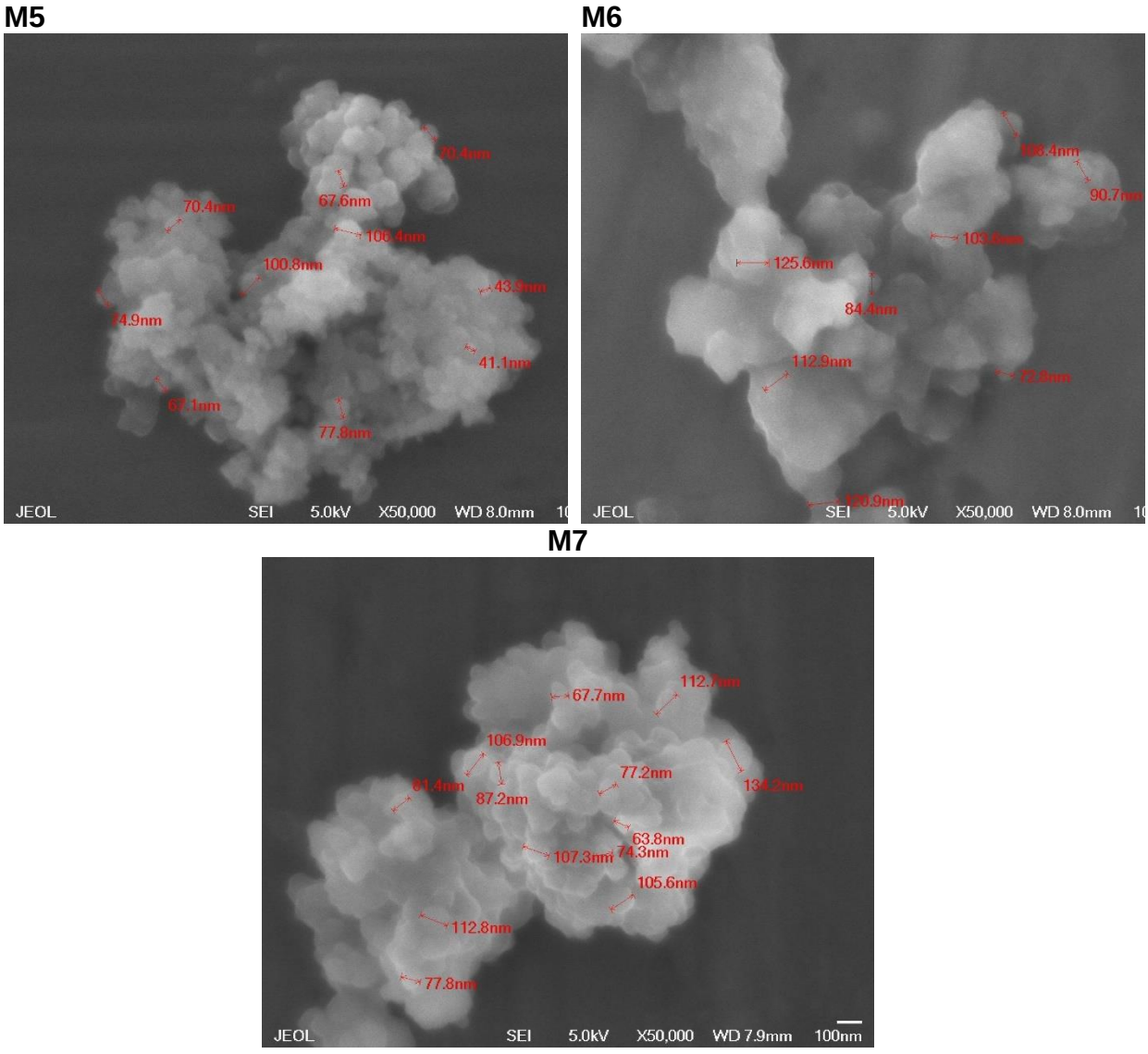

Fig. 19. Sem images of the MIL-101(Cr) M5 to M7.

8.3 Green Metrics

The transition from qualitative to quantitative assessments based on quantifiable parameters has been a critical advancement in green chemistry. [76] This study applied the DOZN™ tool to evaluate the compliance with 12 green chemistry principles (GCP) of each MIL-101(Cr) synthesis. Table 4 resumes all output data of the software, expressed

as an adverse effect in percentage in every GCP. As the derivatives were indeterminate, **GCP 8** (*reduced derivatives*) was not applicable to all synthesis; meanwhile, no significant differences were found in the **GCP 9** (*catalysis*) and **GCP** 11 (*real-time analysis for pollution prevention*). In red are shown the higher impacts derived from the synthesis routes; in green, the lowest effect is observed. A significant part of the impacts is listed in M2, M3, and M4; the principal reason is the use of DMF in the purification process and apply a modulator like HNO_3 and CH_3COOH.

Table 4. Output data for the evaluation of green chemistry.

	Impact (%)						
GCP (Green Chemistry Principles)	M1	M2	M3	M4	M5	M6	M7
1. Prevention	7.7	16.6	15.9	15.9	11.2	14.4	6.1
2. Atom Economy	10.3	14.5	14.6	14.6	13.8	13.1	8.1
3.Less Hazardous Chemical Synthesis	8.8	12.4	12.4	26.9	11.8	11.2	7.0
4. Designing Safer Chemicals	11.7	11.7	11.7	18.4	11.7	11.7	11.7
5. Safer Solvents and Auxiliaries	0.0	19.6	17.3	17.7	16.5	15.7	0.0
6. Design for Energy Efficiency	11.9	13.8	14.2	14.2	13.3	12.7	9.3
7. Use of Renewable Feedstocks	10.3	14.5	14.6	14.6	13.8	13.1	8.1
8.Reduce Derivatives	n/a	n/a	n/a	n/a	n/a	n/a	n/a
9. Catalysis	12.5	12.5	12.5	12.5	12.5	12.5	12.5
10. Design for Degradation	9.8	13.7	13.3	13.3	13.3	13.3	10.3
11. Real-time analysis for Pollution Prevention	12.5	12.5	12.5	12.5	12.5	12.5	12.5
12. Inherently Safer Chemistry for Accident Prevention	9.5	13.4	13.4	21.2	12.7	12.1	7.5

According to **GCP 1** (*waste prevention*), it is desirable to avoid generating waste than to clear it up after it has occurred. [71,156] Due to its severity, the use of DMF solvent is the primary contributor to waste in MOF synthesis. Avoiding the use of DMF, a reduction of 60% of environmental impacts in M7 synthesis is reached where contrasted with with the impacts of the M3 synthesis (higher value). This result is an indication of the improvement of the MIL-101(Cr) synthesis in the framework of the Green Chemistry Principle 1.

The *Atom Economy* concept of the **GCP 2** includes making the most effective use of raw materials so that the material (MOF) contains the maximum number of atoms from the reactants. [72] In this regard, the extra washing step with DMF in the purification process of M3 and M4 contributed to the loss of the powder product, thus, M3 and M4 presented significant impacts due to their low mass of MOF powder (1.9 g and 1.828 g) compared with the mass of M7 product (2.4 g).

The **GCP 3** (*less hazardous chemical synthesis*) prioritizes the production of non-toxic compounds for the environment and public health. [157,158] The data on the harmful effects of each raw material is found in the Material Safety Data Sheet and input data of DOZN™. In the procedure of M4, the use of a toxic solvent (DMF) and corrosive compound (HNO_3) presented the major hazard score (Category 4) due to the high acute aquatic toxicity of both substances (<1.00 mg L^{-1}). In the case of M7, the elimination of hazardous compounds from the synthesis process resulted in a reduction of environmental impacts, with a decrease of 74% compared to the M4 synthesis.

The **GCP 4** (*designing safer chemicals*) focuses on how MOF products should be planned to reduce their toxicity and preserve their original purpose [73]; analysis of the toxicity of raw materials and products is required to receive a score on **GCP 4**. LD50 (lethal dose for 50% of mice) of MIL-101(Cr) was utilized due to the lack of information regarding MIL-101(Cr) humans' toxicity. The GHS classification of M1-M7 synthesis corresponds to group 4 (B score = 1) because this value exceeds 2000 mg/kg body weight [113]. Thus, the 20% additional impact of the M4 synthesis is due to the toxicity levels of the raw materials.

Focusing on greener solvents is the most active area of study in green chemistry; the GCP that presented the more difference in impact derived from MIL-101(Cr) production is the **GCP 5** (*Safer Solvents and Auxiliaries)*. Furthermore, many conventional solvents present effects on health and the environment[159,160]. DMF is classified as probably carcinogenic to humans in the 2A group of IARC (International Agency for Research on Cancer) [161]; also, the use of HNO_3 like modulator presents an impact on this GCP due to its harmful characteristic[74]. The non-use of solvents or modulators reduced to 0% the effect of M1 and M7 in **GCP 5**.

The synthesis of MIL-101(Cr) needs high-temperature values for crystallization (220 °C) and purification (80°-100°C), causing a negative effect in the **GCP 6** (design for energy efficiency), which focuses on minimizing the energy requirements[71,73]. In this regard, M8 and M1 presented lower impact due to the less purification step. The **GCP 7** (use of renewable feedstocks) prioritizes using renewable raw materials or feedstocks above

depletion.[156] DOZN™ refers to renewable material as a "biobased product", which means a product composed, in whole or in significant part, of biological products, not the case of PET. The difference in this impact was determined by the lower mass of raw materials and the greater mass obtained in M7 compared with other syntheses.

M7 presents eight green flags, meaning that in 8 GCP shows the lower impact; meanwhile, M4 presents a higher negative effect in 6 GCP. The total environmental score (Fig. 20) can be used for comparison between all synthesis routes; as a previous analysis, the higher impact (54) is observed in M4; basically, the first four routes present higher values than the last synthesis. M7 shows the lowest value of 34; in this sense, applying DOZN™ analysis, M7 can be considering the synthesis with minor impacts.

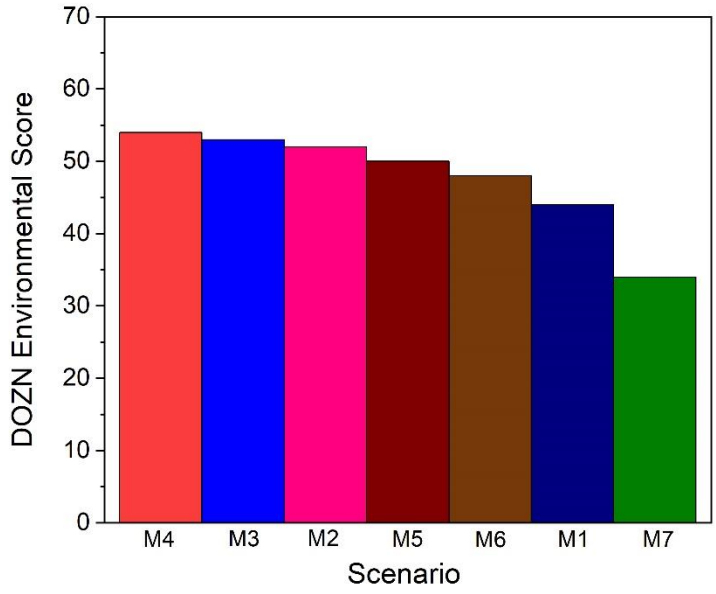

Fig. 20. Total environmental score of different routes of MIL-101(Cr).

The 12 Green Chemistry Principles are categorized into three major groups: Enhanced Energy Efficiency (**GCP 6**), Reduced Human and Environmental Hazards (**GCP 3, GCP**

4, GCP 5, GCP 10, and GCP 12), and Improved Resource Use (**GCP 1, GCP 2, GCP 7, GCP 8, GCP 9, and GCP 11**). Fig. 21 presents the comparison of M7 (lowest impact) and M4 (highest impact).

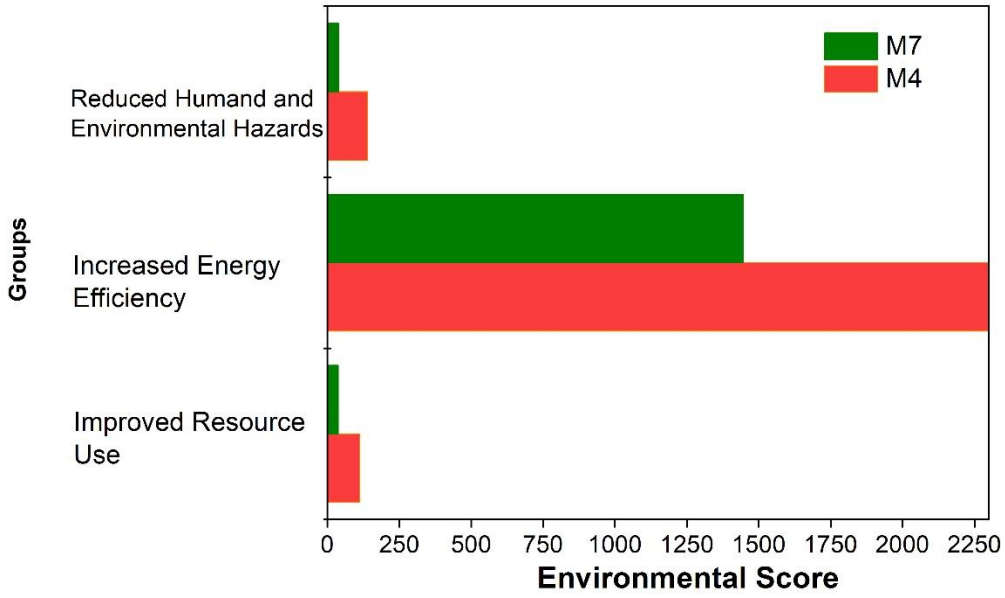

Fig. 21. Groups of impact into environmental score for M4 and M7.

The Reduced Human and Environmental Hazards score for M7 and M4 was 39 and 141, respectively. In the case of the Increased Energy Efficiency category, M7 achieved a lower environmental score (1446) compared with M4 (2250) due to the high yield and fewer stages for the solvent exchange process. At the last category, Improved Resource, M4 presented a value of 112; meanwhile, M7 showed a 38-score value. Finally, DOZN™ provides an aggregate score that resumed all impacts; in this sense, M4 and M7 exhibited 58 and 30, respectively. Based on the results, avoiding HNO_3 as a modulator, using non-toxic solvents, and applying PET as a source of organic linker reduced nearly 50% of the impact on the 12 GCP.

As commented before, green chemistry focuses on the change of conventional solvents for less toxic solvents; similarities are presented between the green assessment conducted using DOZN™ software and other previously reported methodologies. For example, Venturi et al. (2020) [162] showed an environmental assessment of solvents to produce UiO-66. The solvents' greenness was based on the physicochemical properties and toxicity of reagents and products; a color classification of solvents was obtained and evaluated in the synthesis of MOF powder. Although the results showed a green assessment, they were purely descriptive and only considered solvents. In another study, Eftahia et al. (2020) [163] applied a green metric based on 12 GCP to determine sorbent's green assessment; the classification depended on how principles were achieved. However, the metric only considers if the sorbent compliance or not the green chemistry guides; even though it is essential to establish a qualitative metric, it is more pertinent to evaluate the range of green materials based on quantitative metrics [164] as presented using DOZN™.

8.4 Life cycle assessment of MIL-101(Cr)

8.4.1 Life Cycle Inventory

LCA is an alternative to verify material production's greenness. Usually, LCA is considered the best method for quantifying the effects of a process and considers the entire life cycle of the product, including the extraction of raw materials and energy needed to obtain the outcomes. [27]

The inventory data recompiled in the MIL-101(Cr) production are observed in Table 5. The energy needed to synthetize 1 g of MOF powder varies between 116.07 and 123.30 Wh. A major part of power consumption was wasted in the hydrothermal synthesis stage (68%-72%), next the solvent exchange stage represented around a 25-29%, the drying stage wasted 2.1-2.9% of total energy, and finally, less than 0.1% is consumed in the ultrasonic mixing stage. Pioquinto et al. (2021) studied a DUT-4 production on a laboratory scale; the scenario with higher power consumption was observed in the synthesis stage (74%), although the DUT-4 temperature reaction (120° C) was lower than MIL-101(Cr) (215° C), the percentage of power used in synthesis stage is similar to the actual study.

In terms of raw materials, M1-M4 syntheses required a significant amount of organic linker (0.83–0.91 g) to produce 1g of MIL-101(Cr) powder. In contrast, M5-M7 scenarios utilized PET waste as a source of H_2BDC, thereby eliminating the need for a commercial organic linker. The chromium nitrate mass observed was higher in M4 and M5 (2.19 g and 2.11 g); finally, DI water presented mean values of 23.93±1.90 mL. The use of DMF, ethanol, and water in the solvent exchange stage was higher in M4 (54.70 mL) than the mean observed in all other scenarios (DMF 49.41±5.64, ethanol 48.76±5.69, and water 48.76±5.69 mL). The cleaner MOF production searches for the absence of toxic solvents [165] and the minimization of reagents and auxiliaries, [166] in this sense, M7 used fewer raw materials to produce MIL-101(Cr) with similar characteristics compared with scenario M4 (see Section 8.2).

Table 5 Inventory data for MIL-101(Cr) production.

Inputs (Value/UF)	Synthesis						
	M1	M2	M3	M4	M5	M6	M7
Electricity Stage (Wh)							
Ultrasonic Mixing	0.03	0.03	0.02	0.03	0.03	0.03	0.03
Hydrothermal Reaction	84.13	84.13	84.17	84.13	84.14	84.14	84.19
Solvent Exchange	30.16	29.96	30.33	36.24	30.40	30.34	29.36
Drying	2.53	2.88	2.97	2.90	2.58	2.90	1.48
Chemicals Reagents							
H_2BDC (g)	0.87	0.83	0.87	0.91			
PET (g)					0.83	0.79	0.83
Nitrate Chromium (g)	2.11	1.99	2.11	2.19	2.00	1.90	1.67
Water DI (mL)	25.26	23.88	25.26	26.25	24.00	22.86	20
Nitric Acid (mL)				0.24	0.22		
Acetic Acid (mL)			0.23			0.21	
DMF (mL)		49.75	52.63	54.70	50.00	40.00	
Ethanol (mL)	52.63	49.75	52.63	54.70	50.00	40.00	41.67
Water (mL)	52.63	49.75	52.63	54.70	50.00	40.00	41.67

FU: Functional Unit

8.4.2 Environmental impacts of MIL-101(Cr) production

The endpoint indicator ReCiPe single score (related to FU in each scenario) is shown in Fig. 22. In terms of endpoint Single Score, the environmental impact indicators with more contribution in all scenarios of MIL-101(Cr) are climate change, fossil depletion, particulate matter formation, and metal depletion.

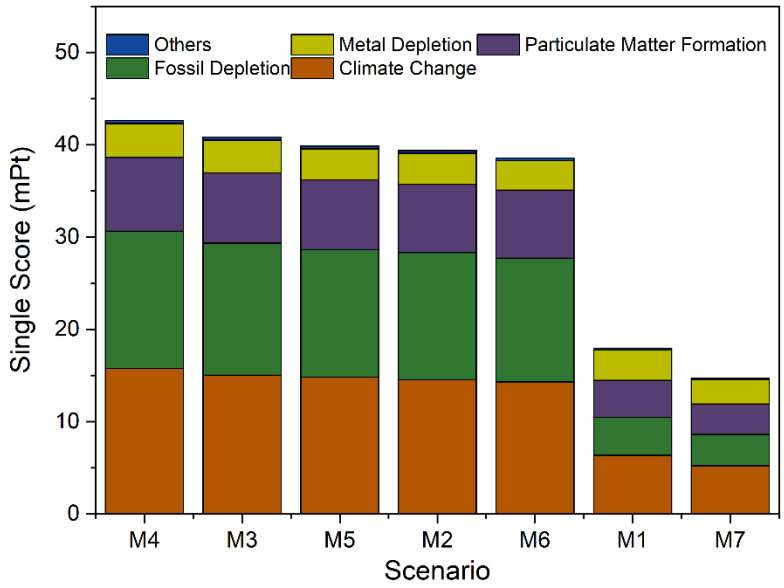

Fig. 22. Environmental impact of MIL-101(Cr) production.

The main impact observed on the three first indicators is related to the use of DMF in the solvent exchange stage; 48.76-54.70 mL of solvent was necessary to remove the unreacted H_2BDC in the synthesis stage. However, the use of DMF added a negative environmental impact on MOF production. The negative effect on metal depletion is directly attributed to chromium nitrate nonahydrate manufacturing. Scenario M4 presented a higher environmental impact (42.62 mPt); meanwhile, the difference between

scenarios M3, M5, M2, and M6 was depreciable (± 0.92 mPt). Minor impacts were observed in M1 (17.9 mPt) and M7 (14.68 mPt); in this sense, the no use of DMF reduced the environmental impacts compared to the remaining scenarios.

The characterization of the indicators of environmental impact for each scenario using the endpoint ReCiPe related to 1 g of MIL-101(Cr) are analyzed in Fig. 23. As observed before, climate change indicator showed more negative affectation. However, previous reports made by Grande et al. (2018) and Pioquinto et al. (2021) expressed that decreasing the amount of solvents reduced the effect of climate change environmental impact. [81,82] Fig. 23a presents that the major impact related to climate change indicator is DMF manufacture. M4, M3, M5, M2, M6, and M7 showed 0.18, 0.17, 0.16, 0.16, 0.15, and 0.13 kg CO_2 eq, respectively, corresponding to DMF production. Meanwhile, no effect was presented in M1 and M7 because no DMF solvent was applied. In this sense, M7 reduces 66% of the impact on climate change compared to M4 (from 0.34 to 0.11 kg CO_2 eq). The main climate change impact in M7 was observed in the electricity needed to carry out the hydrothermal reaction (6.6 $\times 10^2$ kg CO_2 eq).

Fossil depletion is the second most representative MIL-101(Cr) production indicator (Fig. 22), and the results are closely related to the climate change indicator (Figure 23b). Near to 67% of the impact observed in scenarios M2-M6 was related to solvent production. In this sense, DMF manufacture resulted in the activity with the most incidence (8.2-9.4$\times 10^{-2}$ kg oil eq) in fossil depletion, followed by electricity consumption in solvent exchange (1.8×10^{-2} kg oil eq) and hydrothermal synthesis (1.32×10^{-2} kg oil eq).

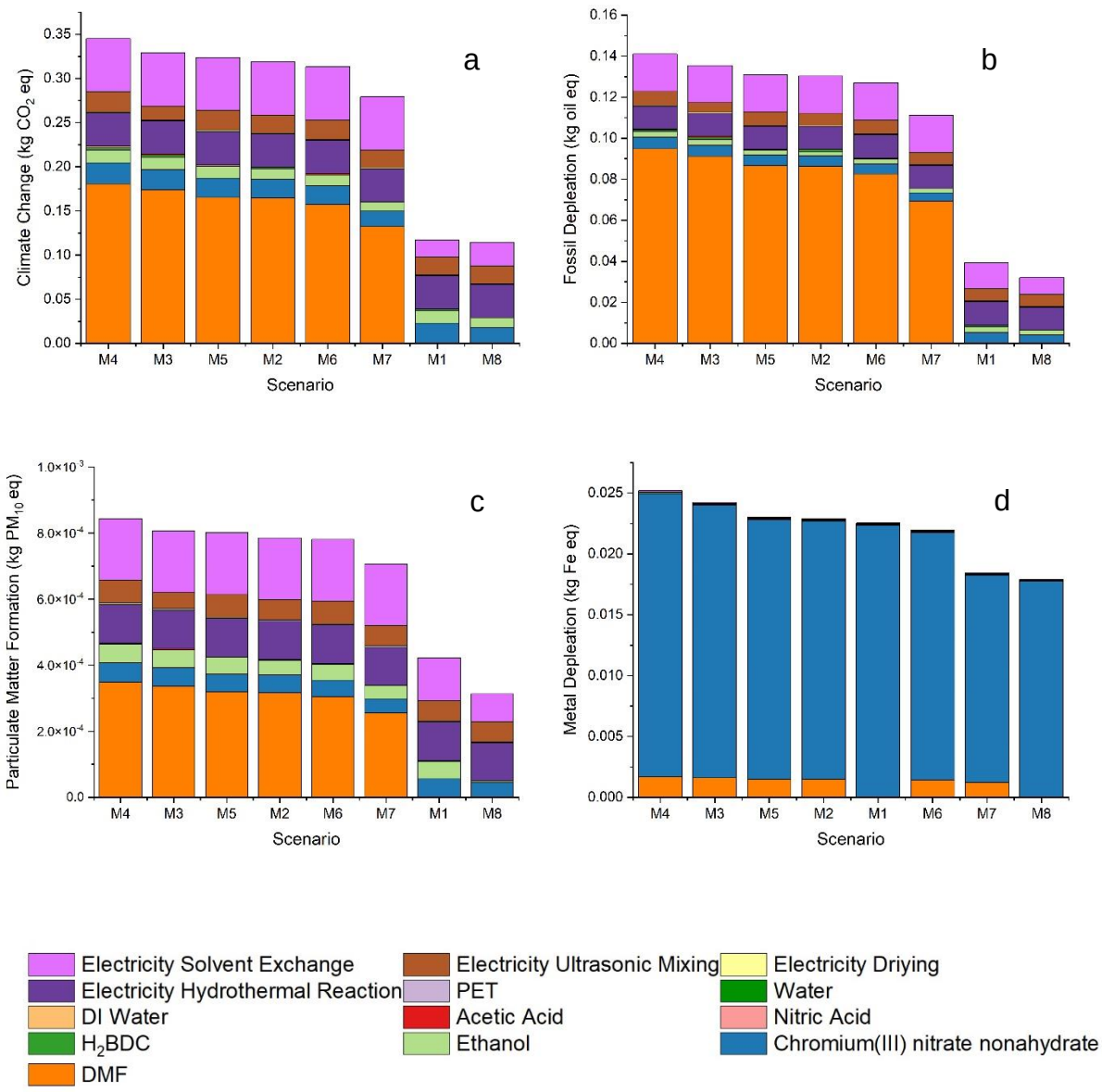

Fig. 23. Environmental impact indicators of each scenario of MIL-101(Cr) production a) climate change, b) fossil depletion, c) particulate matter formation, and d) metal depletion.

On the other hand, the negative sources observed in M1 and M7 were in electricity production used in the hydrothermal reaction stage (0.011 kg oil eq), drying (3.37×10^{-4} and 1.97×10^{-4} kg oil eq), ultrasonic mixing (5.96×10^{-3} kg oil eq), and solvent exchange

(1.2×10^{-2} and 8.1×10^{-3} kg oil eq). Additionally, metallic salt and ethanol production presented 8.02×10^{-2} and 6.36×10^{-3} kg oil eq for M1 and M7, respectively.

Another indicator evaluated was particulate matter formation (Figure 23c). The air emissions responsible for particulate formation come mainly from DMF production in M2-M6 (3.03×10^{-4} - 3.48×10^{-4} kg PM_{10} eq); the main contributors to this indicator are sulfur dioxide (39%), $PM_{2.5}$ (32%), and nitrogen oxides (17%). In addition, the total energy necessary for MIL-101 (Cr) production added near of 30% of the total impact on particulate matter formation. Finally, as described before, chromium (III) nitrate nonahydrate impacts in the metal depletion category (Fig 23d): 99% of impact into this environmental category was due to metal salt in M7 and M1; additionally, DMF only is related to 6-7% of effects in the metal depletion category.

Similar studies of LCA of MOF production exhibit that a significant decrease in solvent consumption can reduce the impact of climate change, fossil depletion, and particulate matter production indicators; in this sense, the greenness scenario decreases 66% of the adverse effects observed in M4. Pioquinto-García et al., (2021) presented a scenario of DUT-4 avoiding DMF solvent; as a result, a reduction of 90% impacts was achieved, although the adsorption capacity of the material was lower than conventional synthesis.

The Green Chemistry Principle 4, applied to MOF production, explains that chemical modifications to MOF procedure should be designed to preserve the efficacy of function while reducing toxicity [156,165]. As presented before, all MIL-101 (Cr) showed a similar

adsorption capacity, but the M7 procedure eliminates toxic solvent and reduces the energy used in the cleaning step; as a result, the product still exhibits the desired function with less environmental impact.

8.5 Economic Assessment

The potential of a novel green material must be evaluated, along with its economic performance, according to certain current criteria for assessing MOF synthesis. These criteria focus on environmental issues or a specific application and the product's entire cost. [168] The manufacturing cost distributions of MIL-101(Cr) at a laboratory scale were evaluated using Monte Carlo simulation. The variability of chemicals market price, electricity cost, and equipment acquisition were related in Appendix B.

The results of simulated production cost distributions for MIL-101(Cr) scenarios are observed in Fig. 24. M4 presented the highest mean production cost ($6.56 g^{-1}, ±1.48), and a major part of the results (90%) are from $4.34 g^{-1} to $8.50 g^{-1}. The synthesis cost of routes M3, M5, M2, M6, and M7 are $6.42 g^{-1} (±1.43), $6.26 g^{-1} (± 1.36), $6.24 g^{-1} (±1.35), $6.11 g^{-1} (±1.29), and $5.62 g^{-1} respectively. Meanwhile, M1 presented a mean synthesis cost of $5.25 g^{-1} (±0.88), and M7 has the lowest average production cost ($4.28 g^{-1}, ±0.70), with 90% of outcomes from $3.18 g^{-1} to $5.17 g^{-1}. Monte Carlo simulations indicate that avoiding the use of an organic solvent (DMF) reduced the economic

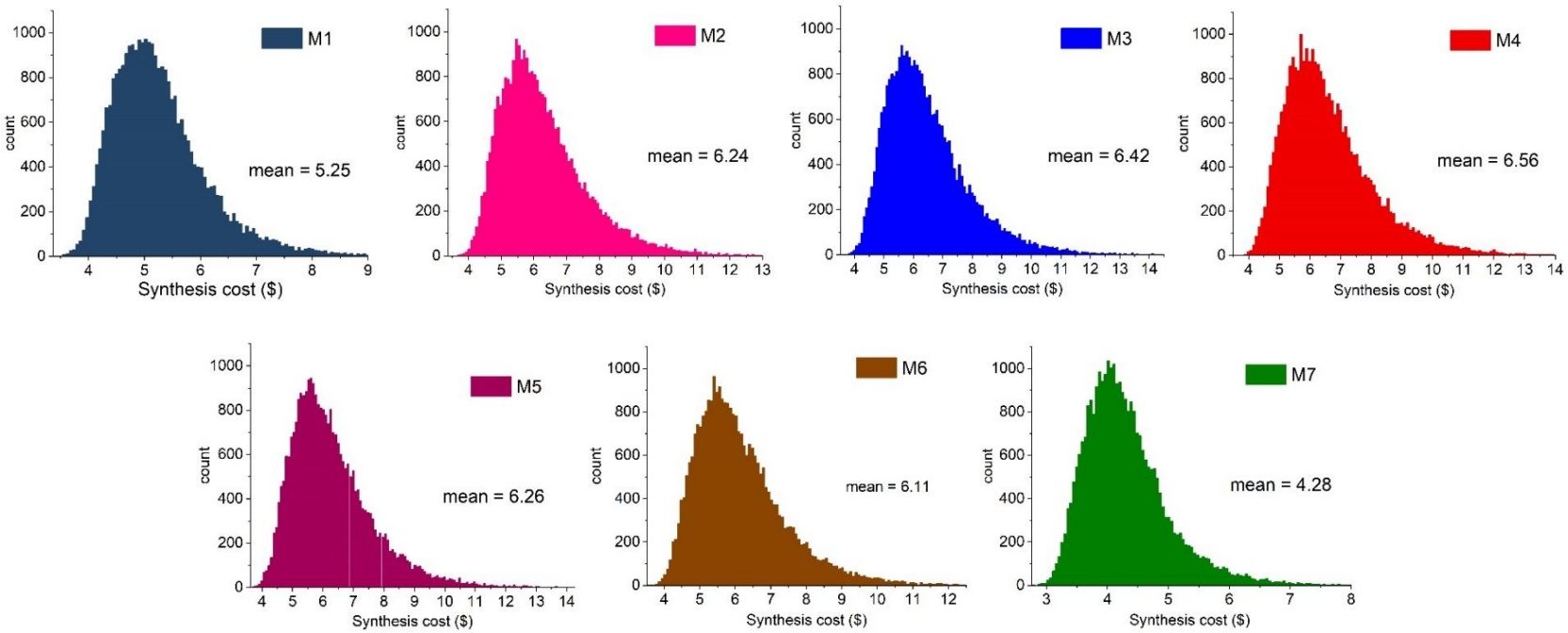

Fig. 24. Total cost production of MIL-101(Cr) scenarios.

impact of MOF production; M1 and M7 presented the lower cost values; meanwhile, the synthesis applied DMF in the exchange solvent process (M2, M3, M4, M5, M6, and M7) exhibited cost from \$6.11 g^{-1} to \$6.56 g^{-1}.

The total cost of producing 1 g of MIL-101(Cr) was divided into capital and operating costs (see Eq. 1). About 50% of the total synthesis cost corresponded to equipment acquisition, categorized into the operating cost. At a laboratory scale, the value of producing material can be up to 1000 times in comparison with an industrial process [169,170], increasing the amount of material produced can reduce the cost of capital cost for example, in a scaled-up production of UiO-66, the equipment cost showed a 20% of the total value of MOF manufacture.[171] The operating cost includes the raw chemicals for MOF synthesis (metal salt, DI water, and organic linker), solvents (DMF, ethanol, and water), and energy consumption. Especially the use of organic solvent significantly impacted the total cost. The Monte Carlo simulation indicates that the no use of DMF reduced the economic impact of synthesis. M1 and M7 presented the lower cost values (USD 5.25 g^{-1} and USD 4.26 g^{-1}); meanwhile, the routes that used DMF in the purification process (M2, M3, M4, M5, and M6) exhibited cost from USD 6.11 g^{-1} to USD 6.56 g^{-1}, the amount used was about 49.75 mL-54.7 mL, corresponding about 30-35% of the total cost (USD 1.8 g^{-1}-USD 1.96 g^{-1}). In similar research, the economic feasibility of different UiO- 66-NH_2 production; 50% of the synthesis cost corresponded to solvents (DMF and methanol).[171] In addition, 40% of the total cost of MOF Mg_2(dobdc) production corresponds to solvents.[172] In our study, not using DMF solvent at the laboratory scale could reduce 35% of the synthesis

cost of M7 compared with the higher cost value (M4). In the case of electricity, nearly 3% of the total value of 1 g MIL-101(Cr) manufacture corresponded to the energy cost (USD 0.14-0.16 g^{-1}); the price of electricity was calculated using the Mexican rate (north), based on 0.047 USD kWh^{-1}. M7 production is favorably significantly increased at the lab scale from operating and capital costs.

Even though MOF has been studied and applied recently, only a few industries commercialize the MIL-101(Cr). Depending on the physicochemical properties of MOF powder and the commercial brand, the cost of MIL-101(Cr) varies between USD 315-880 g^{-1}.[173,174] Although in this study, the cost related to lab construction, management, labor, equipment maintenance, and taxes did not account for; the value obtained by M7 (USD 4.28 g^{-1}), avoiding the use of DMF and H_2BDC could reduce the impact cost of commercial value. For example, PET flakes used in the M7 scenario as an organic linker instead of H_2BDC could promote an eco-design or recycling cost subsidy [175].

8.6 Adsorption MIL-101(Cr) powders

8.6.1 Adsorption Kinetics

Adsorption kinetics is the study of how adsorption occurs over time, including the rate at process it happens. The adsorption kinetics experiments of toluene onto MIL-101(Cr) powders (M1-M7) were performed using 40 mg of each adsorbent in a headspace vial (20 mL) under laboratory conditions and 2 ppm initial concentration of the VOC. The

kinetic adsorption of the MIL-101(Cr) materials took around 20 min to reach equilibrium (Fig. 25). The adsorption capacity of M5-M7 samples was comparable to that of M1-M4, indicating that PET waste did not compromise the performance of the material at low toluene concentrations.

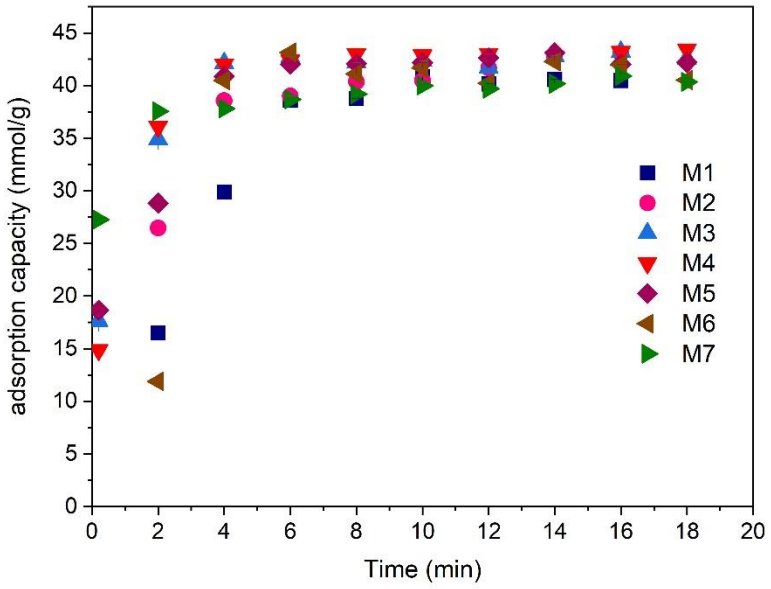

Fig. 25. Adsorption kinetics of M1-M7.

The PFO and PSO kinetic models were used to fit the experimental data of the MIL-101 (Cr) powder material (Appendix C). The parameters of the models and the experimental fit error are shown in Table 6. The PFO model correlation coefficients (R^2) were higher than those presented by the PSO model. On the other hand, the theoretical adsorption capacity of the adsorbent at equilibrium (q_e) using the PFO model was near to the experimental values; experimental data of q_e for M7 was 40.34 mmol g^{-1}; meanwhile simulation model observed 40.34 mmol g^{-1}. Although the PSO model presented high correlation coefficients, the PFO coefficients were closer to 1; only M3-PFO showed a lower value of R^2 compared with the PFO kinect model (0.89<0.95). PSO model was

more suitable for describing the toluene adsorption process at 2 ppm toluene concentration; this meant physical adsorption played a significant role in the toluene adsorption processes.

Table 6. Parameters for PFO and PSO kinetic models.

Scenario	PFO			PSO		
	q_e (mmol g^{-1})	k_1 (min^{-1})	R^2	q_e (mmol g^{-1})	k_2 (g $mg^{-1}min^{-1}$)	R^2
M1	42.01 ± 1.18	0.28	0.97	52.3 ± 3.7	0.00543	0.93
M2	41.87 ± 0.60	0.51	0.97	47.41 ± 1.51	0.01481	0.94
M3	42.53 ± 0.18	2.51	0.89	43.40 ± 0.19	0.07912	0.95
M4	43.06 ± 0.11	0.89	0.86	44.03 ± 0.25	0.08464	0.84
M5	43.31 ± 0.27	0.08	0.96	43.31 ± 0.27	0.08643	0.96
M6	42.01 ± 0.19	0.70	0.30	42.72 ± 0.71	0.09713	0.16
M7	40.34 ± 0.11	5.63	0.99	40.60 ± 0.09	0.25167	0.99

8.6.2 Adsorption Isotherms

Adsorption isotherm is a graphical representation of the relationship between the adsorption capacity at equilibrium and the residual concentration of the adsorbate at equilibrium at constant temperature. To determine the adsorption capacity at equilibrium as a function of the toluene concentration at equilibrium, the adsorption isotherms for M4 and M7 were performed at a constant temperature of 25 °C, 1 atm of pressure, 40 mg of MOF material, and up to P/P_o 3.0 x 10^{-3} (Fig. 26). At a low relative pressure (P/P_o = 3.2 x10^{-5}), the equilibrium adsorption capacity of M4 and M7 was found to be similar, ranging between 0.66-0.68 mmol g^{-1}. However, as the relative pressure increased (P/P_o =2.2x10^{-3}), the adsorption capacity of M4 was found to be higher (6.8 mmol g^{-1}) that that of M7

(3.97 mmol g^{-1}). These findings suggest that while M7 may exhibit comparable performance to M4 at low relative pressures, it may not be as effective at higher relative pressures.

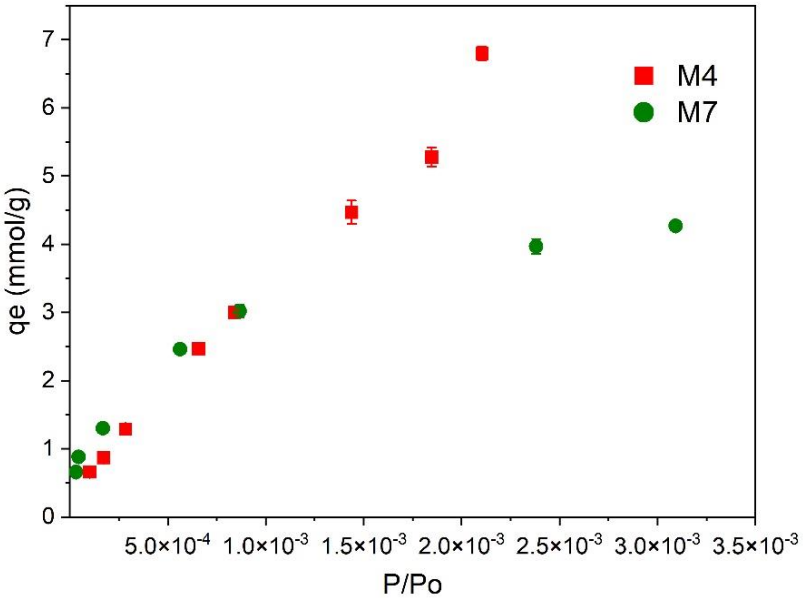

Fig. 26. M4 and M7 adsorption isotherms.

8.6.3 Continuous Toluene Adsorption onto MIL-101(Cr) powder

Breakthrough curves can be considered the last essential characterizations to determine the adsorption processes of new materials. Two samples were used: the conventional synthesis method (M4) versus the green material (M7). The toluene adsorption (250 ppm) was carried out at 25°C and 1 atm with flow of 250 mL min^{-1}. The breakthrough curves of toluene in M4 and M7 are shown in Figure 27. The saturation time of M4 and M7 was 240 and 170 min, respectively. In addition, the adsorption capacity at saturation time observed was 50.54 and 31.41 mg g^{-1} for M4 and M7, respectively. These values resulted from the

differences in the surface area of the evaluated materials. M4 presented a higher value (3431 m^2 g^{-1}) compared with the greener version of MIL-101(Cr) (1852 m^2 g^{-1}).

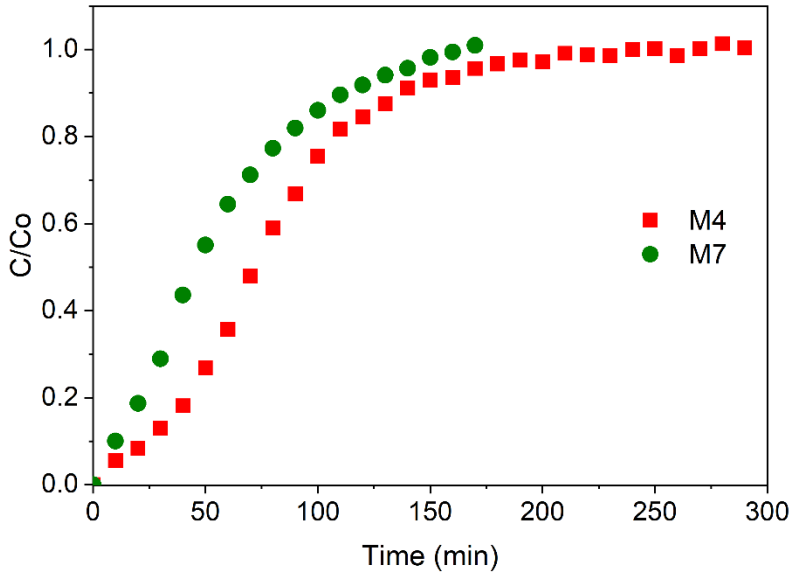

Fig. 27. Breakthrough curves of M4 and M7 samples.

For an idealized situation, the breakthrough curve is S-shaped, symmetrical, and with similar times at breakthrough and saturation.[178] In this regard, the breakthrough curve of M7 is less stepper than M4 curve. The gradual slope change observed in the breakthrough curve of M7 could be attributed to the more complex pore structure or a high degree of tortuosity. The non-local density functional theory (NL-DFT) was applied to obtain the pore size distribution curves [179] for M7 and M4. The distribution over the mesoporous range (2-50 nm) is extensive for the M7 sample; this behaviour can be understood in terms of PET impurities.

8.7 Techno-Economic and Environmental Assessment of MIL-101(Cr) powders.

To obtain a general view of the selection of the ideal adsorbent, it is essential to evaluate the economical and sustainable impact of MIL-101(Cr) routes. Previously, Pioquinto-García et al. (2021) presented a techno-environmental impact factor of DUT-4; the value was obtained by the ratio of environmental impact and the adsorption capacity, in this case, an economic factor of MIL-101(Cr) scenarios was added (Table 7). Therefore, the environmental impact-adsorption capacity ratio and economic value were estimated for M1-M7 scenarios. The assessment considered the environmental impact using LCA, the adsorption kinetics of toluene, and the production cost using Monte Carlo simulation for all the MIL-101(Cr) scenarios.

Table 7. Techno-Economic Environmental Assessment of MIL-101(Cr) Scenarios.

Scenario	Environmental impact/Adsorption capacity ratio (mPt $mmol^{-1}$)	Synthesis cost (USD g^{-1})
M1	0.4484	5.25
M2	0.9285	6.24
M3	0.9258	6.42
M4	0.9669	6.56
M5	0.9048	6.26
M6	0.9132	6.11
M7	0.3719	4.28

First, M2-M6 had a high environmental impact/adsorption capacity ratio (mPt $mmol^{-1}$) and a high synthesis cost (USD g^{-1}). These values can be explained by the fact that M2-M6

employs DMF as a solvent in an additional step, raising the cost of material and energy needed for the purification step; additionally, the environmental impact of solvent manufacture impacts the ratio considering the adsorption capacity. On the other hand, M1 has a 20% lower synthesis cost than M4 and a 55% lower environmental impact per mmol of toluene adsorbed. Moreover, the M7 scenario offers the lowest environmental impact/adsorption capacity ratio, and the average synthesis cost was the lowest. Therefore, compared with M4, M7 is considered 45% more economically efficient and 60% better environmental performance by mass of toluene adsorbed. Although all scenarios presented similar adsorption capacities (40.33 mmol g^{-1}-43.43 mmol g^{-1}), the use of DMF increased the cost of synthesis and showed more negative environmental impacts due to solvent production.

In a sustainable approach, a novel material must demonstrate an economic advantage, minimal environmental impact, and technical improvement, [180,181] in this sense, the TOPSIS methodology was used to select the best option material. Three criteria were applied: adsorption capacity, environmental, and cost impact (Fig. 28).

The ideal option as a toluene adsorbent at low concentrations was M7 scenario; the low environmental impact (15 mPt) of production and the minor synthesis cost (USD 4.28 g^{-1}) compared with the scenarios helped to obtain a score of 0.92. In the case of adsorption capacity, the value obtained of M7 (40.33 mmol g^{-1}) was not the higher value; nevertheless, no differences were shown compared with scenarios ubicated in superior adsorption rank (43.03 mmol g^{-1}).

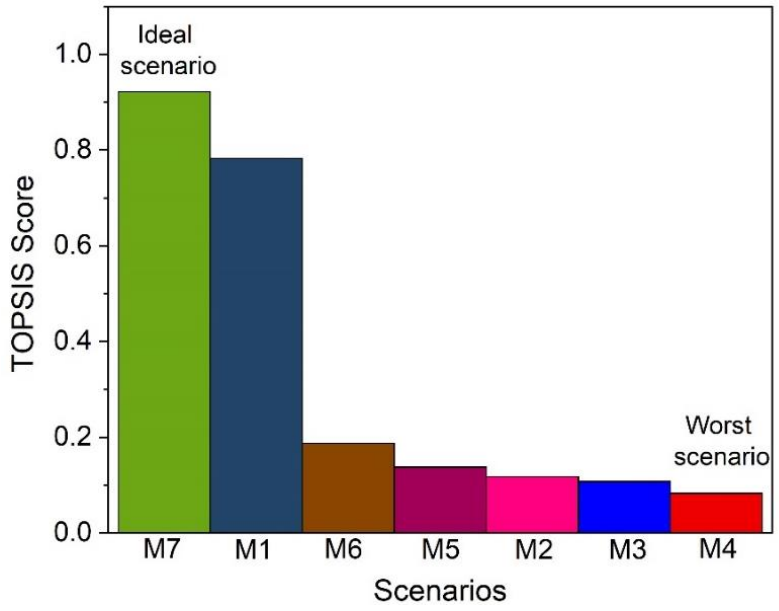

Fig. 28. TOPSIS score of MIL-101(Cr) scenarios.

The second most cost-environmentally-effective scenario was M1, which, compared with M7, presented nearly -15% efficiency. Although the values of adsorption capacity (40.14 mmol/mg) and the environmental impact (18 mPt) were near M7, the criteria of synthesis cost were higher (USD 5.25 g^{-1}), affecting the rank obtained. The next rank was M6 (score = 0.18); compared with M7 and M1, the environmental impact (37 mPt) and synthesis cost were higher (USD 6.11 g^{-1}). The following scenarios ubicated in the rank were M5 (score 0.13) > M2 (score 0.11) > M3 (score 0.10); the differences observed were minimal. Finally, although M4 had the highest toluene adsorption capacity (43.44 mmol g^{-1}), it is the most expensive option, and the environmental impact that presented the synthesis is considered the worst. In this sense, M4 showed -91% effectiveness compared with the cleaner option (M7).

8.8 MIL-101(Cr)-Monolith

To determine the ideal paste formulation, two types of solvents, two binders, and different MOF amounts resulted in 55 different formulations of pastes, however, only three formulations presented characteristics that allowed extrusion (Table 8).

Table 8. Paste formulations with printability.

	Monolith A (%wt)	Monolith B (%wt)	Monolith C (%wt)
M4	17.5	29	24
CMC	2.5	3	2
H_2O	80	68	74

Fig. 29 shows the MIL-101(Cr)-monoliths using paste formulations described before. The printed monolith was designed with specific dimensions (1.5 cm of diameter and 1 cm of height). However, monolith A (Fig. 29a) showed deficiencies, the monolith channels did not have the required size and form. Modifying the percentage of MOF and CMC (29% and 3%wt) resulted in monolith B (Fig. 29b). While well-defined channels were observed in the initial layers of the monolith, it was found that the paste did not exhibit sufficient printability in the later layers to form a complete structure. This may be attributed to a low water content in the paste relative to monoliths A and C, which may have resulted in insufficient adhesion between adjacent layers.

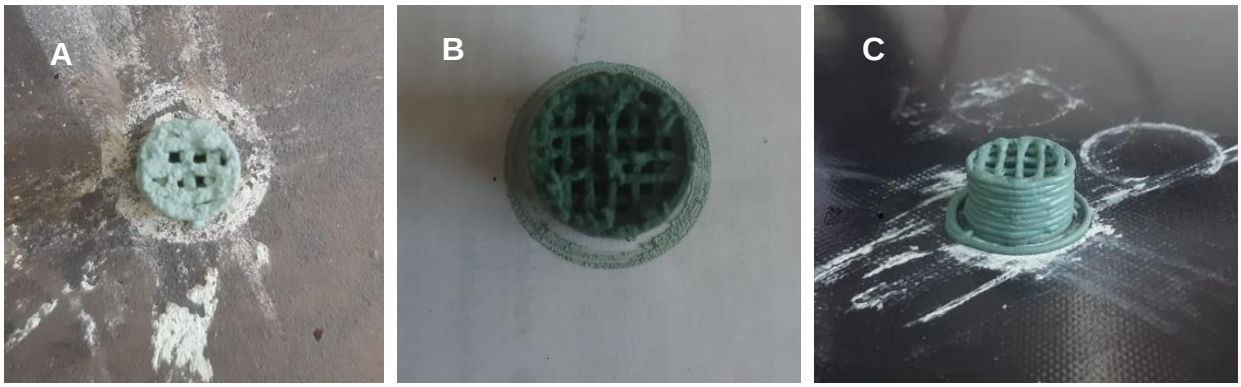

Fig. 29. 3D printed monoliths using paste formulations described in Table 9 a) monolith A, b) monolith B and c) monolith C.

Finally, Monolith C, which contained 24% MOF, exhibited ideal extrusion properties, resulting in a well-defined structure with clearly defined channels (Fig. 29c). However, the dimensions of the printed monolith differed slightly from those specified in the Cura software, with a 10% difference in extrusion line diameter and a 13% difference in spacing between channels (Fig. 30). This deviation may be attributed to the density of the CMC (1.59 g cm^{-3}), which can affect the size and shape of the printed channels.

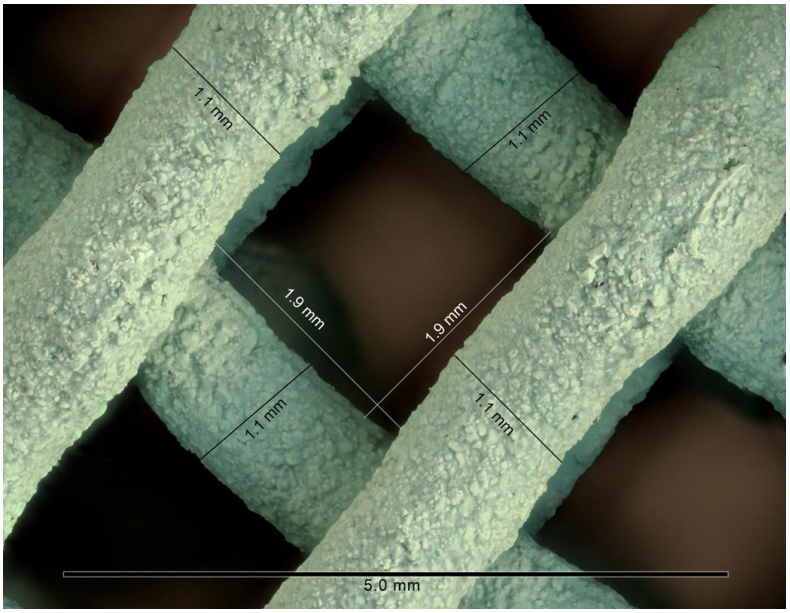

Fig. 30. Channels size of monolith C.

Although an extrusion was achieved, the monolith presents structural deficiencies, as shown in Fig. 31. The channels presented several fractures, which are of the fragile fracture type; the kind of crack presented is observed with a shallow plastic deformation at the fracture vertex.

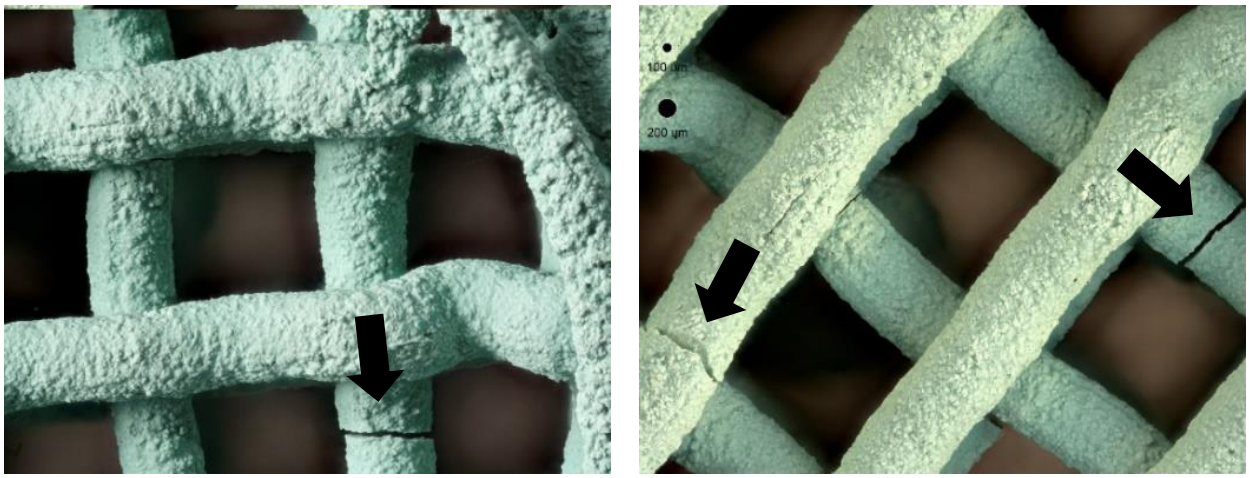

Fig. 31. Fractures observed in channels of monolith c.

Binder plays a crucial role in paste 3D printing; it is responsible for holding the shape of the printed object until it is cured or dried, without binder, the printed object may lose its shape, deform, or collapse. [127,182] In this sense, monolith D was formed with a percentage of kaolin (10%wt) to prevent fractures in the structure. Although the extrusion of the paste was observed, the phenomenon of widening of the lower layers is present; the density of the material used in 3D printing can have an effect on the widening of printed monoliths walls. The monolith D still presents structural deficiency due to the density of CMC (Fig. 32), it presented a variation (7.5 %) in dimensions of the first layers compared to the last.

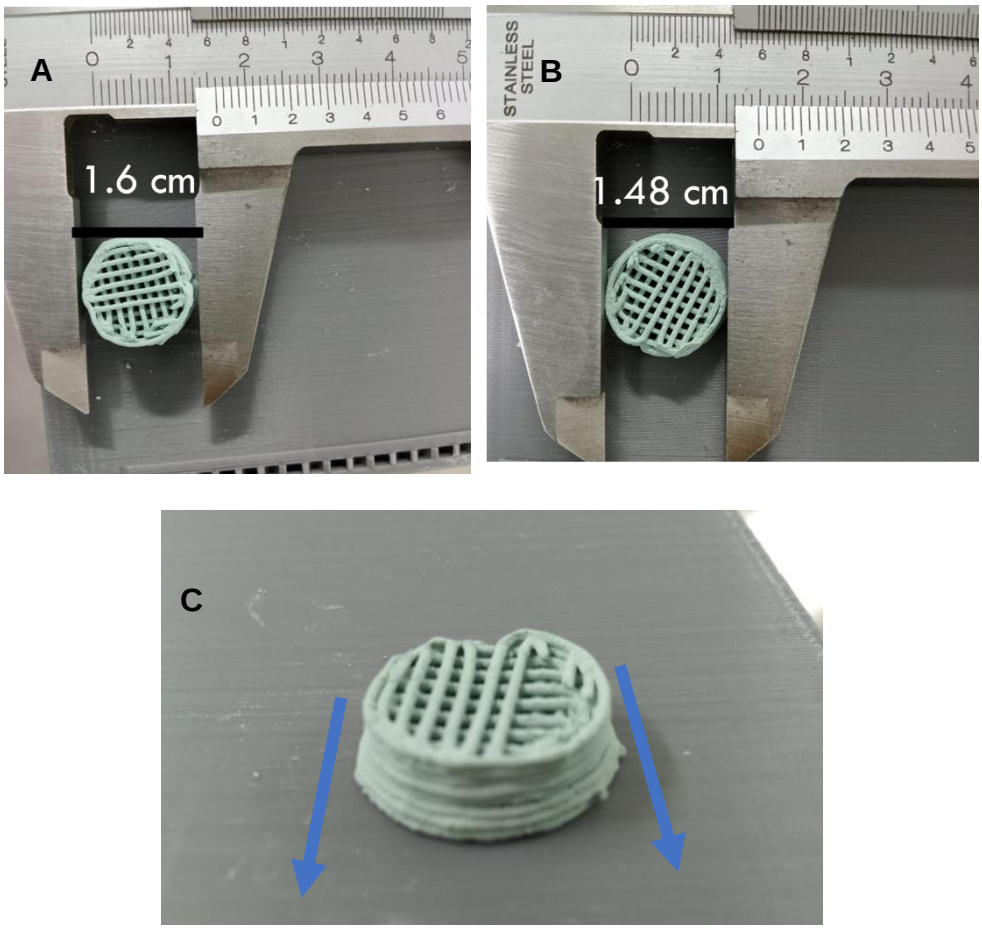

Fig. 32. Dimensions of monolith D a) first layers, b) last layers ,and c) effect of CMC into dimensions of monolith d.

To minimize the impact of CMC density on the 3D printing process and the dimensions fo the monolith, it was necessary to modify the paste formulation by using a solvent that allowed for optimal paste flow. Ethylene glycol (EG) was identified as a suitable solvent and substituted for CMC in the new formulation. Specifically, the new paste composition comprised 1 g of 90% wt MIL-101(Cr) powder material, 10% wt kaolin clay, 1.2 mL of EG, and water in 1:1 ratio. As a result of the new formulation, a Monolith E was printed in a 0.6 mm nozzle. The effect of the widening of the lower layers on the overall geometry of the printed monolith was not observed, the lower density of EG (1.11 g cm^{-3}) compared

with CMC demonstrate better results. This allowed for the printing of monoliths with varying channel geometries, such as square or hexagonal channels, as demonstrated in Fig. 33.

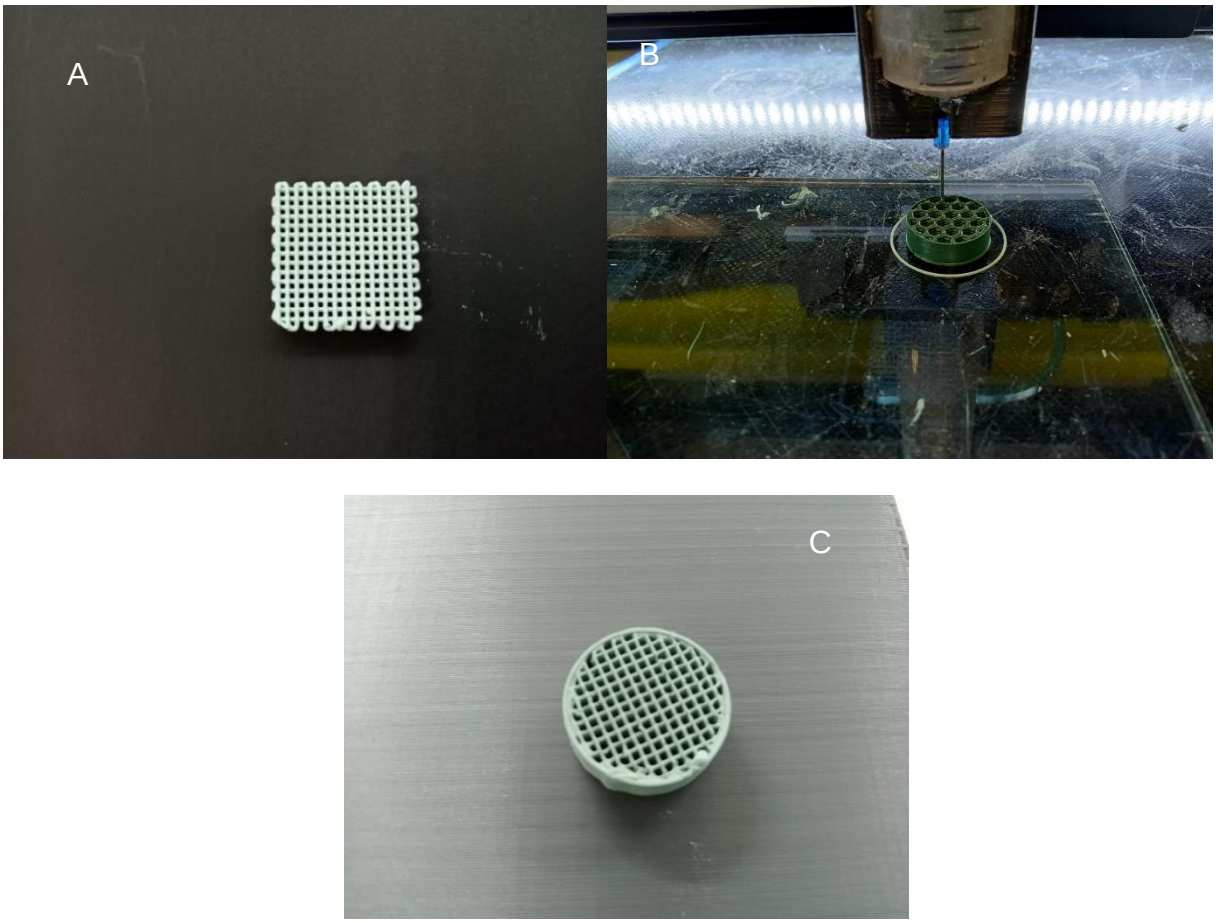

Fig. 33. Monolith E a) square form and honeycomb channels, b) circle form and hexagonal channels, and c) circle form and honeycomb channels.

8.8.1. Rheology Characterization

The paste or slurry used in 3d printing must have the necessary rheological characteristics to be applied in the extrusion process.[183] This slurry must flow

continuously through a small nozzle without clogging (shear thinning), then quickly solidify to maintain its form after extrusion. [184] The viscosity-shear rate profile of MOF-kaolin paste is observed in Fig. 34.

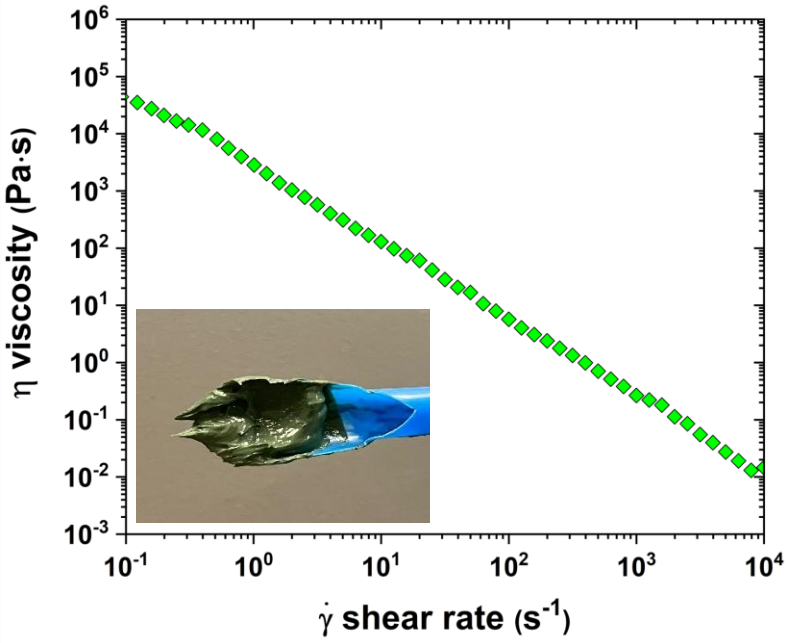

Fig 34. Apparent viscosity MIL-101(Cr)-kaolin paste as a function of shear rate.

The paste displays the shear thinning characteristic, a rheological property necessary for extrusion-based 3D printing. In addition, the MOF-kaolin paste presented a high viscosity at a low shear rate, but the viscosity decreased with increasing the shear rate; these results suggested suitable extrusion behavior, as in previous reports.[126] Furthermore, the viscosity of the paste is controlled by the presence of solvents (EG+H_2O); in this sense, the relation 1:1 in the 1.2 mL volume seems ideal for presenting the required viscoelasticity.

As previously mentioned, the paste must flow constantly through a fine nozzle. In contrast to the paste used in Monolith D, which required a 0.8 mm extrusion nozzle, the paste used in Monolith E operated effectively with a smaller 0.6 mm nozzle due to its improved shear thinning behavior.

The oscillatory frequency sweep (OFS) data also reinforces the result of the apparent viscosity of MIL-101(Cr)-kaolin paste. OFS experiment is applied to evaluate the viscoelastic behavior of a material (Fig. 35). The storage modulus shear (G') and loss modulus (G'') indicate solid-state and liquid-state behaviors, respectively. The storage modulus (G') of the MOF-kaolin paste was observed at ~1x10^5 Pa, which is above the loss modulus (G'') ~ 1x10^4 Pa until they crossed at a high yield stress value (1.2x10^2 Pa). The gel point is considered when the fluid changes from liquid-state to solid elastic behavior.

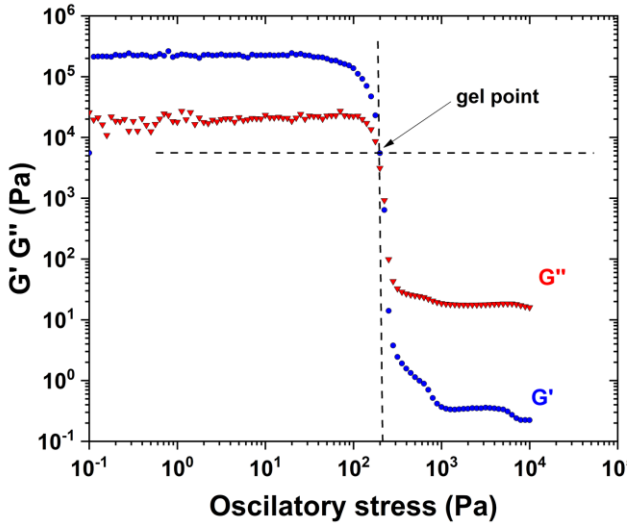

Fig. 35. The storage modulus G' and the loss modulus G'' obtained against the Oscillatory stress (Pa).

The rheological characterization of the MOF-kaolin paste confirmed its printability, and monolith E did not exhibit any deformation (Fig. 36) in comparison to monoliths A through D

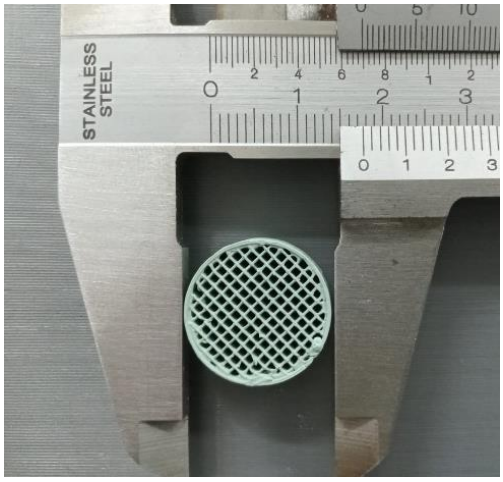

Fig. 36. Monolith printed with no deformation.

8.8.2. XRD

The XRD patterns of the kaolin clay, MIL-101(Cr) powder, and MOF-monolith are presented in Fig. 37. The diffraction peaks of kaolin clay are observed in 2θ = 12.4º, 19.9º, 24.9º, 35º, and 38º. Meanwhile, the MIL-101(Cr) powder sample presented similar peaks mentioned before (XRD powder characterization, section 4.2.1). For the 3D-printed MIL-101(Cr) monolith, the X-ray reflections from planes (333), (531), (606), and (753) with diffraction peaks at 2θ = 5.3°, 6°, 8.5°, 9.2°, confirm the MIL-101(Cr) crystal structure. MIL-101(Cr) still exhibits the original structure of MOF after extruding. The peaks corresponding to kaolin clay in the MOF-monolith pattern showed a low intensity attributed to the minimum percentage in the paste to form the monolith (10%).

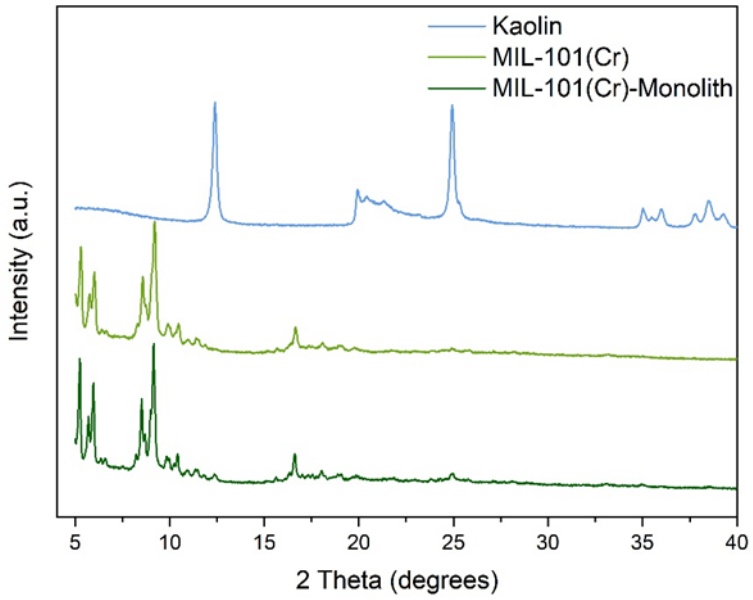

Fig. 37. XRD patterns of kaolin clay, MIL-101(Cr), and MIL-101(Cr)-monolith.

8.8.3. FT-IR

The functional groups of kaolin clay, MIL-101(Cr), and MIL-101(Cr)-monolith were obtained by FT-IR (Fig. 38). The characteristic peak at 570 cm^{-1} corresponding to the Cr-O vibration is observed, which indicates a connection between Cr and the carboxyl groups of the organic ligand. While the peaks between 600 and 1600 cm^{-1} are attributed to terephthalic acid and its aromatic rings, the peaks at 750, 880, 1016, and 1150 cm^{-1} correspond to the C-H vibration. The peak located near 1400 cm^{-1} is due to the symmetric O-C-O strain. The band indicated at the wavelength of 1517 cm^{-1} is related to the C=C tension. The peaks observed at 1623 and 3400 cm^{-1} are characteristic of water molecules adsorbed inside the MOF. The results shown in the FT-IR analysis are consistent with data already published. [50,185,186]

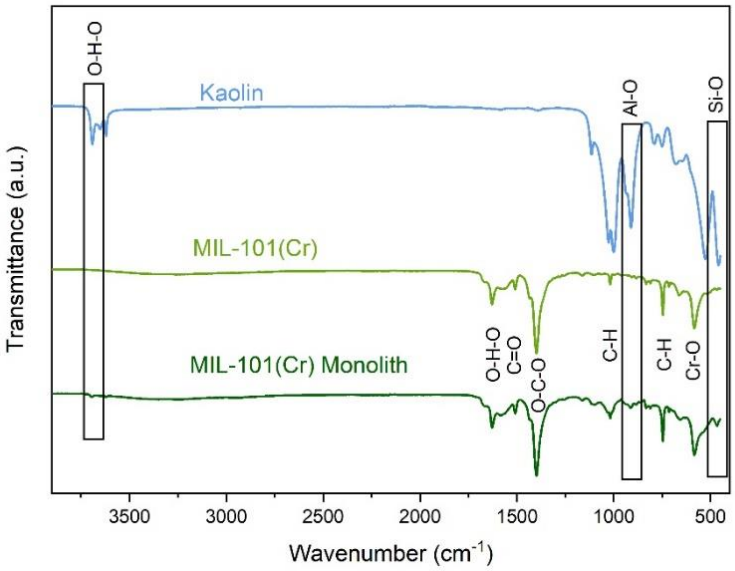

Fig. 38. FTIR spectra for kaolin clay, MIL-101(Cr), and MIL-101(Cr)-monolith.

8.8.4. Continuous Toluene Adsorption onto MIL-101(Cr) Monolith

The dynamic adsorption performance of the 3D-printed MIL-101(Cr)-monolith was evaluated through breakthrough tests; the effluent was diluted with air, choosing the required air flow rate (Q= 250 mL min^{-1}) to get C_o=250 ppm of VOC vapor (butanol, toluene or cyclohexane), the experiment was carried out at ambient temperature, the adsorption experiment was done by duplicate. Previously, a nitrogen flow was applied to the monolith column (1.8 cm in diameter and 0.5 cm high). The breakthrough curve using the 3D printed MIL-101(Cr)-monolith for butanol and cyclohexane removal is observed in Fig. 39. The initial removal of VOCs by the adsorbent monolith was found to be higher in the first few minutes of exposure. However, as the saturation time was reached, the amount of adsorption became constant, indicating that no further removal of butanol or cyclohexane from the stream was observed.

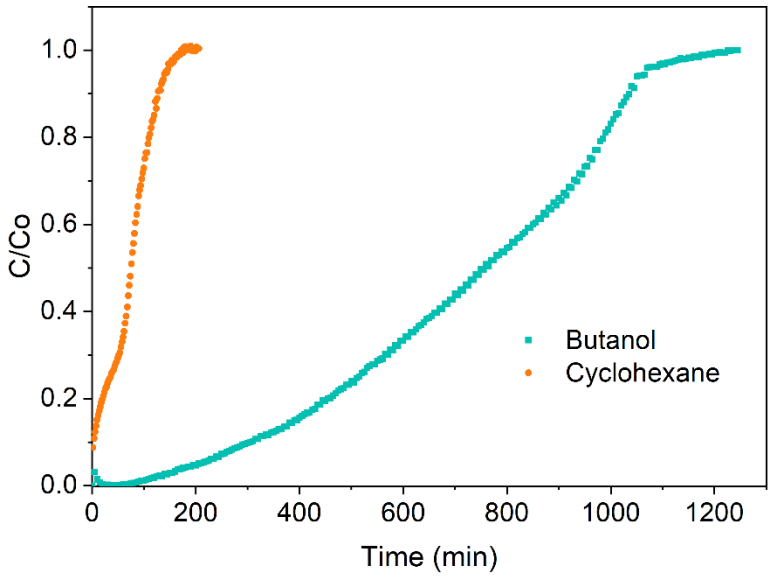

Fig. 39. Breakthrough curve of butanol and cyclohexane using 3D printed MIL-101(Cr)-kaolin monolith.

It is noted that the saturation time for cyclohexane (160 min) was lower than that obtained from butanol (1230 min). As a result, the adsorption capacity was 40.43 mg g^{-1} and 215 mg g^{-1} for cyclohexane and butanol, respectively. The high butanol adsorption capacity can be explained by the stronger interactions, such as electrostatic interactions, with the polar metal centers in the MOF structure compared to the relatively nonpolar cyclohexane. In addition, butanol can engage in additional intermolecular forces, such as hydrogen bonding, due to its polar nature and the presence of the hydroxyl groups. These hydrogen bonding interactions can further strengthen the adsorption of butanol within the MIL-101(Cr) structure.

The breakthrough curves of toluene adsorption in MIL-101(Cr)-monolith and MIL-101(Cr) powder are shown in Fig. 40. The breakthrough curves are similar for both materials; a saturation time of 240 and 270 min was obtained for MOF powder and monolith,

respectively. The equilibrium adsorption capacity of monolith was slightly lower (46.19 ± 0.59 mg g^{-1}) than MOF powder (52.65 ± 1.59 mg g^{-1}), the reason could be that monolith presented lower MIL-101(Cr) material in its structure (90%MOF-10%Kaolin); the active sites for toluene adsorption was decreased and finally the adsorption capacity was reduced.

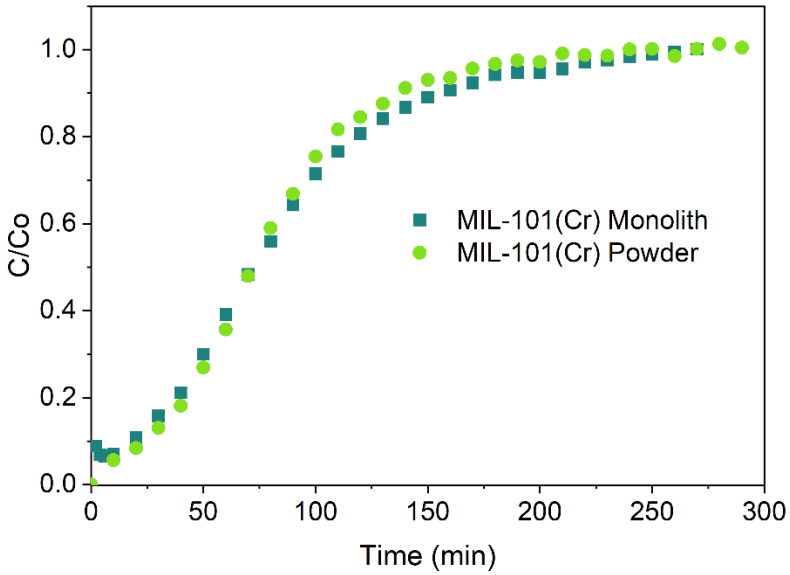

Fig. 40. Breakthrough curve of toluene using MIL-101(Cr) powder and 3D printed MIL-101(Cr)-kaolin monolith.

The breakthrough curves of MIL-101(Cr) powder and MIL-101(Cr) monolith data was fitted to Thomas and Yoon-Nelson models. These models are the most general and widely used to describe the dynamic adsorption in fixed bed columns. Table 9 presents the parameters for Thomas and Yoon-Nelson models which have been calculated from breakthrough curve of MIL-101(Cr) powder and MIL-101(Cr) monolith at toluene concentration of 250 ppm. According to the coefficient correlation (R^2) value, the Yoon-Nelson model prediction was in good agreement with the experimental results indicating

that it is suitable for describing the toluene dynamic adsorption at initial concentration of 250 ppm. The time required to reach 50 % of breakthrough time t obtained from the calculation is similar to those obtained experimentally (74 min).

Table 9. Predicted parameters for Thomas and Yoon Nelson model for toluene adsorption at 250 ppm.

Material	Thomas Model			Yoon-Nelson Model		
	K_{TM} (mL mg^{-1} min^{-1})	q_{TM} (mg g^{-1})	r^2	K_{YN} (mL min^{-1})	τ (min)	r^2
MIL-101(Cr) powder	0.031	61.35	0.986	0.034	78.35	0.996
MIL-101(Cr)-kaolin monolith	0.032	48.47	0.984	0.028	84.5	0.995

MOFs have been applied to remove toluene from air streams; in this sense, Table 10 resumes the adsorption capacity and experiment conditions of various MOFs. Even though the value of toluene adsorbed (mg) per gram of MIL-101(Cr)-monolith was lower than other MOFs, in dynamic adsorption, the velocity of the fluid flowing through the adsorbent bed can significantly impact the adsorption capacity. The flow conditions of the MIL-101(Cr)-monolith adsorption experiment was carried out at 250 mL min^{-1}, higher compared with the other adsorbents; at higher fluid velocities, the contact time between the adsorbate and adsorbent is reduced, resulting in lower adsorption capacity. For future work, it will be necessary to compare adsorption capacities at different flow conditions.

Table 10. Toluene adsorption capacity of MOF adsorbents.

Adsorbent	Form	Mass (mg)	Flow (mL min^{-1})	Co (ppm)	q_t (mg/g))	Reference
UiO-66	powder	200	50	1000	151	Zhang et al. (2019).[187]
ZIF-8	powder	50	50	110	6.3	Li et al. (2021).[188]
CF-1100 (ZIF-8 at 1100°C)	powder	51	50	110	208.5	
MIL-101 (Cr)	powder	40	70	655	397	Wang et al. (2021).[189]
MIL-68@PVA	beads	200	1000	200	43.59	Berilyn et al. (2022).[190]
HKUST-1@PVA	beads	200	1000	200	123	
UiO-66-NH_2	powder	200	50	1000	162	Shi et al. (2020).[191]
MIL-101(Cr)	powder	360	250	250	52.6	This study
MIL-101(Cr)-monolith	monolith	360	250	250	35.09	

9. CONCLUSIONS

This research obtained the techno-economical environmental assessment of eight routes of MIL-101(Cr) synthesis. In addition, MOF powder was suitable to be printed in monolith form by 3D technology. According to XRD and NMR data from BDC obtained from PET and compared with BDC-Sigma Aldrich, it was possible to use PET to synthesize MOF due to similar characteristics. Meanwhile, XRD reflections of M1-M7 matched XRD patterns of simulated MIL-101(Cr); However, only M2, M3, and M4 present a comparable intensity of the peaks. According to SEM analysis, M1-M4 showed the octahedral form of the MIL-101(Cr); meanwhile, M5-M7 exhibited agglomeration of particulate. In another way, M7 presented the higher surface area of scenarios that use PET and avoid DMF (1852 m^2 g^{-1}).

Using DOZN software was determined that M4 synthesis represented the higher adverse effect on the Green Chemistry Principles; the significant impacts were observed in Prevention, Less Hazardous Chemical Synthesis, Safer Solvents and Auxiliaries, and Inherently Safer Chemistry for Accident Prevention. Furthermore, green synthesis of MIL-101(Cr) was achieved and evaluated by LCA. The main environmental impacts were observed in Climate Change, Fossil Depletion, Particulate Matter, and Metal Depletion due to DMF and chromium (III) nitrate nonahydrate production. The M7 scenario reduced 66% of the adverse effects observed in M4.

Monte Carlo simulation assessed the production cost distributions of MIL-101(Cr) scenarios at a laboratory scale. The results of simulated production cost distributions in

order were M4>M3>M5>M2>M6>M1>M7. The lowest average production cost was observed in M7 ($4.28 g^{-1}, ±0.70), with 90% of outcomes from $3.18 g^{-1} to $5.17 g^{-1}.

The adsorption kinetics of toluene onto MIL-101(Cr) powders (M1-M7) was fast, 20 min to reach equilibrium. A minimal difference in adsorption capacity was observed in MIL-101 scenarios (43.44-40.33 mmol g^{-1}). The PFO presented a higher correlation than PSO kinetic model; physical adsorption played a significant role in the toluene adsorption processes. The toluene adsorption isotherms for M4 and M7 at P/P_0 =2.2x10^{-3} were 6.8 mmol g^{-1} and 3.97 mmol $g^{-1,}$ respectively. Finally, the saturation time in continuous adsorption processes of M4 and M7 and was 1.5 h and 6.25 h, respectively; the main difference is due to the superior surface area of M4-MOF.

Breakthrough curves can be considered the last essential characterizations to determine the adsorption processes of new materials. M4 and M7 were used to evaluate the continuous adsorption processes (250 ppm and 250 mL min^{-1}); the saturation time of M4 and M7 was 240 min and 170 min, respectively. The differences in the saturation time were derived from the surface area of the materials.

TOPSIS method was applied to consider three criteria: adsorption capacity, environmental, and cost impact. The best option for toluene MIL-101(Cr) adsorbent was M7; the low environmental impact (15 mPt) of production and the minor synthesis cost (USD 4.28/g) compared with the M1-M6 scenarios helped obtain a high score of 0.92. In the case of the adsorption capacity, the value obtained of M7 (40.33 mmol/g) was not the

higher value; nevertheless, no differences were shown compared with scenarios ubicated in superior adsorption rank (43.03 mmol/g). In this sense, M7 was 91% cleaner option than the worst scenario (M4).

55 pastes formulations were evaluated to allow extrusion; in this sense, the paste that used CMC presented extrusion; however, monolith presented structural affections due to the density of CMC (1.59 g cm^{-3}). On the other hand, applying EG into the paste exhibited no dimension or widening effect in the monolith due to the lower density (1.11 g cm^{-3}) value compared with CMC. In addition, rheology experiments showed that the paste of monolith E presented the necessary printability; XRD and FTIR confirmed the structure of MIL-101(Cr) remains after printing.

The breakthrough experiment (Co= 250 ppm and Q=250 mL min^{-1}) for MOF powder and monolith presented a similar saturation time, 240 min and 270 min. In addition, the equilibrium adsorption capacity of the monolith was slightly lower (46.19 ± 0.59 mg g^{-1}) than MOF powder (52.65 ± 1.59 mg g^{-1}). The lower toluene uptake over MIL-101(Cr)-monolith than powder resulted from less active sites (90% MOF-10% kaolin). Nevertheless, the adsorption capacity difference was near 8%. Finally, MIL-101(Cr) could be immobilized in monolith using a 3D printing technique, and it showed a similar performance than powder material for the adsorption of toluene in dynamic conditions.

10. REFERENCES

(1) Kumar, A.; Singh, B. P.; Punia, M.; Singh, D.; Kumar, K.; Jain, V. K. Assessment of Indoor Air Concentrations of VOCs and Their Associated Health Risks in the Library of Jawaharlal Nehru University, New Delhi. *Environmental Science and Pollution Research* **2014**, *21* (3), 2240–2248. https://doi.org/10.1007/s11356-013-2150-7.

(2) Sacks, J. D.; Fann, N.; Gumy, S.; Kim, I.; Ruggeri, G.; Mudu, P. Quantifying the Public Health Benefits of Reducing Air Pollution : Critically Assessing the Features and Capabilities of WHO ' s AirQ + and U . S . EPA ' s Environmental Benefits Mapping and Analysis Program — Community Edition (BenMAP — CE). *Atmosphere (Basel)* **2020**, *11* (516), 1–15.

(3) Madureira, J.; Paciência, I.; Rufo, J.; Severo, M.; Ramos, E.; Barros, H.; de Oliveira Fernandes, E. Source Apportionment of CO2, PM10 and VOCs Levels and Health Risk Assessment in Naturally Ventilated Primary Schools in Porto, Portugal. *Build Environ* **2016**, *96*, 198–205. https://doi.org/http://dx.doi.org/10.1016/j.buildenv.2015.11.031.

(4) Fang, L.; Norris, C.; Johnson, K.; Cui, X.; Sun, J.; Teng, Y.; Tian, E.; Xu, W.; Li, Z.; Mo, J.; Schauer, J. J.; Black, M.; Bergin, M.; Zhang, J.; Zhang, Y. Toxic Volatile Organic Compounds in 20 Homes in Shanghai: Concentrations, Inhalation Health Risks, and the Impacts of Household Air Cleaning. *Build Environ* **2019**, *157* (March), 309–318. https://doi.org/10.1016/j.buildenv.2019.04.047.

(5) D'Eon, J. C.; Stirchak, L. T.; Brown, A. S.; Saifuddin, Y. Project-Based Learning Experience That Uses Portable Air Sensors to Characterize Indoor and Outdoor Air Quality. *J Chem Educ* **2021**, *98* (2), 445–453. https://doi.org/10.1021/acs.jchemed.0c00222.

(6) Ohura, T.; Amagai, T.; Senga, Y.; Fusaya, M. Organic Air Pollutants inside and Outside Residences in Shimizu, Japan: Levels, Sources and Risks. *Science of the Total Environment* **2006**, *366* (2–3), 485–499. https://doi.org/10.1016/j.scitotenv.2005.10.005.

(7) Fernandes, M. B.; Brickus, L. S. R.; Moreira, J. C.; Cardoso, J. N. Atmospheric BTX and Polyaromatic Hydrocarbons in Rio de Janeiro, Brazil. *Chemosphere* **2002**, *47* (4), 417–425. https://doi.org/10.1016/S0045-6535(01)00319-8.

(8) Tello-Leal, E.; Macías-Hernández, B. A. Association of Environmental and Meteorological Factors on the Spread of COVID-19 in Victoria, Mexico, and Air Quality during the Lockdown. *Environ Res* **2021**, *196* (November 2020). https://doi.org/10.1016/j.envres.2020.110442.

(9) Notario, A.; Bravo, I.; Adame, J. A.; Díaz-de-Mera, Y.; Aranda, A.; Rodríguez, A.; Rodríguez, D. Variability of Oxidants (OX=O3+NO2), and Preliminary Study on Ambient Levels of Ultrafine Particles and VOCs, in an Important Ecological Area in Spain. *Atmos Res* **2013**, *128* (2), 35–45. https://doi.org/10.1016/j.atmosres.2013.03.008.

(10) Wu, X. M.; Fan, Z. T.; Zhu, X.; Jung, K. H.; Ohman-Strickland, P.; Weisel, C. P.; Lioy, P. J. Exposures to Volatile Organic Compounds (VOCs) and Associated Health Risks of Socio-Economically Disadvantaged Population in a “Hot Spot” in Camden, New Jersey. *Atmos Environ* **2012**, *57*, 72–79. https://doi.org/10.1016/j.atmosenv.2012.04.029.
(11) Arora, P.; Rehman, I. H.; Suresh, R.; Sharma, A.; Sharma, D.; Sharma, A. Assessing the Role of Advanced Cooking Technologies to Mitigate Household Air Pollution in Rural Areas of Solan, Himachal Pradesh, India. *Environ Technol Innov* **2020**, *20*, 101084. https://doi.org/10.1016/j.eti.2020.101084.
(12) Hori, H.; Ishimatsu, S.; Fueta, Y.; Ishidao, T. Evaluation of a Real-Time Method for Monitoring Volatile Organic Compounds in Indoor Air in a Japanese University. *Environ Health Prev Med* **2013**, *18* (4), 285–292. https://doi.org/10.1007/s12199-012-0319-1.
(13) Caselli, M.; de Gennaro, G.; Marzocca, A.; Trizio, L.; Tutino, M. Assessment of the Impact of the Vehicular Traffic on BTEX Concentration in Ring Roads in Urban Areas of Bari (Italy). *Chemosphere* **2010**, *81* (3), 306–311. https://doi.org/10.1016/j.chemosphere.2010.07.033.
(14) Bari, Md. A.; Kindzierski, W. B.; Wheeler, A. J.; Héroux, M.-È.; Wallace, L. a. Source Apportionment of Indoor and Outdoor Volatile Organic Compounds at Homes in Edmonton, Canada. *Build Environ* **2015**, *90*, 114–124. https://doi.org/10.1016/j.buildenv.2015.03.023.
(15) Luo, H.; Guan, Q.; Lin, J.; Wang, Q.; Yang, L.; Tan, Z.; Wang, N. Air Pollution Characteristics and Human Health Risks in Key Cities of Northwest China. *J Environ Manage* **2020**, *269* (May), 110791. https://doi.org/10.1016/j.jenvman.2020.110791.
(16) Tóxicas, S.; Enfermedades, R. De. ATSDR - ToxFAQs™: Tolueno. **2001**.
(17) Haro-garcía, L.; Vélez-zamora, N.; Aguilar-madrid, G.; Guerrero-rivera, S. ALTERACIONES Hematológicas En Trabajadores Expuestos Ocupacionalmente a Mezcla de Benceno- Tolueno-Xileno (BTX) En Una FÁBRICA de PinturaS BENZENE-TOLUENE-XYLENE (BTX) IN A PAINT FACTORY. **2012**, *29* (2), 181–187.
(18) An, Y. J. Toxicity of Benzene, Toluene, Ethylbenzene, and Xylene (BTEX) Mixtures to Sorghum Bicolor and Cucumis Sativus. *Bull Environ Contam Toxicol* **2004**, *72* (5), 1006–1011. https://doi.org/10.1007/s00128-004-0343-y.
(19) Services, H. INTERACTION PROFILE FOR : Benzene , Toluene , Ethylbenzene , and Xylenes (BTEX). **2004**, No. May.
(20) Yang, Y.; Liu, X.; Zheng, J.; Tan, Q.; Feng, M.; Qu, Y.; An, J.; Cheng, N. Characteristics of One-Year Observation of VOCs, NOx, and O3 at an Urban Site in Wuhan, China. *Journal of Environmental Sciences* **2019**, *79*, 297–310. https://doi.org/10.1016/J.JES.2018.12.002.
(21) Huang, L.; Wei, Y.; Zhang, L.; Ma, Z.; Zhao, W. Estimates of Emission Strengths of 43 VOCs in Wintertime Residential Indoor Environments, Beijing. *Science of the Total Environment* **2021**, *793*, 148623. https://doi.org/10.1016/j.scitotenv.2021.148623.

(22) Sofuoglu, S. C.; Aslan, G.; Inal, F.; Sofuoglu, A. An Assessment of Indoor Air Concentrations and Health Risks of Volatile Organic Compounds in Three Primary Schools. *Int J Hyg Environ Health* **2011**, *214* (1), 36–46. https://doi.org/10.1016/j.ijheh.2010.08.008.

(23) Yao, M.; Zhang, Q.; Hand, D. W.; Perram, D. L.; Taylor, R. Investigation of the Treatability of the Primary Indoor Volatile Organic Compounds on Activated Carbon Fiber Cloths at Typical Indoor Concentrations. *J Air Waste Manage Assoc* **2009**, *59* (7), 882–890. https://doi.org/10.3155/1047-3289.59.7.882.

(24) Parmar, G. R.; Rao, N. N. Emerging Control Technologies for Volatile Organic Compounds. *http://dx.doi.org/10.1080/10643380701413658* **2009**, *39* (1), 41–78. https://doi.org/10.1080/10643380701413658.

(25) Thakkar, H.; Eastman, S.; Hajari, A.; Rownaghi, A. A.; Knox, J. C.; Rezaei, F. 3D-Printed Zeolite Monoliths for CO2 Removal from Enclosed Environments. *ACS Appl Mater Interfaces* **2016**, *8* (41), 27753–27761. https://doi.org/10.1021/acsami.6b09647.

(26) Dedecker, K.; Dumas, E.; Lavédrine, B.; Steunou, N.; Serre, C. *Metal-Organic Frameworks for the Capture of Volatile Organic Compounds and Toxic Chemicals*; 2019. https://doi.org/10.1016/b978-0-12-814633-0.00007-7.

(27) Sepúlveda-Cervantes, C. v.; Soto-Regalado, E.; Rivas-García, P.; Loredo-Cancino, M.; Cerino-Córdova, F. d. J.; García Reyes, R. B. Technical-Environmental Optimisation of the Activated Carbon Production of an Agroindustrial Waste by Means Response Surface and Life Cycle Assessment. *Waste Management and Research* **2018**, *36* (2), 121–130. https://doi.org/10.1177/0734242X17741680.

(28) Zhao, X. S.; Ma, Q.; Lu, G. Q. VOC Removal: Comparison of MCM-41 with Hydrophobic Zeolites and Activated Carbon. *Energy and Fuels* **1998**, *12* (6), 1051–1054. https://doi.org/10.1021/ef980113s.

(29) Piechota, G.; Hagmann, M.; Buczkowski, R. Removal and Determination of Trimethylsilanol from the Landfill Gas. *Bioresour Technol* **2012**, *103* (1), 16–20. https://doi.org/10.1016/J.BIORTECH.2011.09.002.

(30) Yaghi, O. M.; Li, H. Hydrothermal Synthesis of a Metal-Organic Framework Containing Large Rectangular Channels. *J Am Chem Soc* **1995**, *117* (41), 10401–10402. https://doi.org/10.1021/ja00146a033.

(31) Kwon, H. T.; Jeong, H. K. In Situ Synthesis of Thin Zeolitic-Imidazolate Framework ZIF-8 Membranes Exhibiting Exceptionally High Propylene/Propane Separation. *J Am Chem Soc* **2013**, *135* (29), 10763–10768. https://doi.org/10.1021/ja403849c.

(32) Sheikh Alivand, M.; Hossein Tehrani, N. H. M.; Shafiei-Alavijeh, M.; Rashidi, A.; Kooti, M.; Pourreza, A.; Fakhraie, S. Synthesis of a Modified HF-Free MIL-101(Cr) Nanoadsorbent with Enhanced H2S/CH4 , CO2/CH4, and CO2 /N2 Selectivity. *J Environ Chem Eng* **2019**, *7* (2), 102946. https://doi.org/10.1016/j.jece.2019.102946.

(33) Karina, A.; Leite, P.; Silva, B.; Kulesza, J.; Fagner, J. Modulator Effect of Acetic Acid on the Morphology of Luminescent Mixed Lanthanide- Organic Frameworks. **2017**, *20*, 681–687.
(34) Wen, M.; Li, G.; Liu, H.; Chen, J.; An, T.; Yamashita, H. Metal-Organic Framework-Based Nanomaterials for Adsorption and Photocatalytic Degradation of Gaseous Pollutants: Recent Progress and Challenges. *Environ Sci Nano* **2019**, *6* (4), 1006–1025. https://doi.org/10.1039/c8en01167b.
(35) Yang, K.; Xue, F.; Sun, Q.; Yue, R.; Lin, D. Adsorption of Volatile Organic Compounds by Metal-Organic Frameworks MOF-177. *J Environ Chem Eng* **2013**, *1* (4), 713–718. https://doi.org/10.1016/j.jece.2013.07.005.
(36) Howarth, A. J.; Peters, A. W.; Vermeulen, N. A.; Wang, T. C.; Hupp, J. T.; Farha, O. K. Best Practices for the Synthesis, Activation, and Characterization of Metal−organic Frameworks. *Chemistry of Materials*. American Chemical Society January 10, 2017, pp 26–39. https://doi.org/10.1021/acs.chemmater.6b02626.
(37) Kayal, S.; Sun, B.; Chakraborty, A. Study of Metal-Organic Framework MIL-101(Cr) for Natural Gas (Methane) Storage and Compare with Other MOFs (Metal-Organic Frameworks). *Energy* **2015**, *91*, 772–781. https://doi.org/10.1016/j.energy.2015.08.096.
(38) Ren, J.; Dyosiba, X.; Musyoka, N. M.; Langmi, H. W.; North, B. C.; Mathe, M.; Onyango, M. S. ScienceDirect Green Synthesis of Chromium-Based Metal-Organic Framework (Cr-MOF) from Waste Polyethylene Terephthalate (PET) Bottles for Hydrogen Storage Applications. *Int J Hydrogen Energy* **2016**, *41* (40), 18141–18146. https://doi.org/10.1016/j.ijhydene.2016.08.040.
(39) Campbell, C.; Ferreiro-Rangel, C. A.; Fischer, M.; Gomes, J. R. B.; Jorge, M. A Transferable Model for Adsorption in Mofs with Unsaturated Metal Sites. *Journal of Physical Chemistry C* **2017**, *121* (1), 441–458. https://doi.org/10.1021/acs.jpcc.6b10751.
(40) Elsayed, E.; AL-Dadah, R.; Mahmoud, S.; Anderson, P. A.; Elsayed, A.; Youssef, P. G. CPO-27(Ni), Aluminium Fumarate and MIL-101(Cr) MOF Materials for Adsorption Water Desalination. *Desalination* **2017**, *406*, 25–36. https://doi.org/10.1016/j.desal.2016.07.030.
(41) Wang, D.; Wu, G.; Zhao, Y.; Cui, L.; Shin, C. H.; Ryu, M. H.; Cai, J. Study on the Copper(II)-Doped MIL-101(Cr) and Its Performance in VOCs Adsorption. *Environmental Science and Pollution Research* **2018**, *25* (28), 28109–28119. https://doi.org/10.1007/s11356-018-2849-6.
(42) Shafiei, M.; Alivand, M. S.; Rashidi, A.; Samimi, A.; Mohebbi-Kalhori, D. Synthesis and Adsorption Performance of a Modified Micro-Mesoporous MIL-101(Cr) for VOCs Removal at Ambient Conditions. *Chemical Engineering Journal* **2018**, *341* (December 2017), 164–174. https://doi.org/10.1016/j.cej.2018.02.027.
(43) Bahri, M.; Haghighat, F.; Kazemian, H.; Rohani, S. A Comparative Study on Metal Organic Frameworks for Indoor Environment Application: Adsorption

Evaluation. *Chemical Engineering Journal* **2017**, *313*, 711–723. https://doi.org/10.1016/j.cej.2016.10.004.
(44) Férey, C.; Mellot-Draznieks, C.; Serre, C.; Millange, F.; Dutour, J.; Surblé, S.; Margiolaki, I. Chemistry: A Chromium Terephthalate-Based Solid with Unusually Large Pore Volumes and Surface Area. *Science (1979)* **2005**, *309* (5743), 2040–2042. https://doi.org/10.1126/science.1116275.
(45) Naseri, M.; Mousavi, S. F.; Mohammadi, T.; Bakhtiari, O. Synthesis and Gas Transport Performance of MIL-101/Matrimid Mixed Matrix Membranes. *Journal of Industrial and Engineering Chemistry* **2015**, *29*, 249–256. https://doi.org/10.1016/j.jiec.2015.04.007.
(46) Kumar, V.; Kumar, S.; Kim, K. H.; Tsang, D. C. W.; Lee, S. S. Metal Organic Frameworks as Potent Treatment Media for Odorants and Volatiles in Air. *Environ Res* **2019**, *168* (October 2018), 336–356. https://doi.org/10.1016/j.envres.2018.10.002.
(47) Férey, C.; Mellot-Draznieks, C.; Serre, C.; Millange, F.; Dutour, J.; Surblé, S.; Margiolaki, I. Chemistry: A Chromium Terephthalate-Based Solid with Unusually Large Pore Volumes and Surface Area. *Science (1979)* **2005**, *309* (5743), 2040–2042. https://doi.org/10.1126/science.1116275.
(48) Singh, L.; Agarwal, T. Comparative Analysis of Conventional and Greener Extraction Methods and Method Validation for Analyzing PAHs in Cooked Chicken and Roasted Coffee. *Food Chem* **2021**, *364* (June), 130440. https://doi.org/10.1016/j.foodchem.2021.130440.
(49) Han, G.; Rodriguez, K. M.; Qian, Q.; Smith, Z. P. Acid-Modulated Synthesis of High Surface Area Amine-Functionalized MIL-101(Cr) Nanoparticles for CO2Separations. *Ind Eng Chem Res* **2020**, *59* (40), 18139–18150. https://doi.org/10.1021/acs.iecr.0c03456.
(50) Lo, S. H.; Senthil Raja, D.; Chen, C. W.; Kang, Y. H.; Chen, J. J.; Lin, C. H. Waste Polyethylene Terephthalate (PET) Materials as Sustainable Precursors for the Synthesis of Nanoporous MOFs, MIL-47, MIL-53(Cr, Al, Ga) and MIL-101(Cr). *Dalton Transactions* **2016**, *45* (23), 9565–9573. https://doi.org/10.1039/c6dt01282e.
(51) Dyosiba, X.; Ren, J.; Musyoka, N. M.; Langmi, H. W.; Mathe, M.; Onyango, M. S. Feasibility of Varied Polyethylene Terephthalate Wastes as a Linker Source in Metal–Organic Framework UiO-66(Zr) Synthesis. *Ind Eng Chem Res* **2019**, *58* (36), 17010–17016. https://doi.org/10.1021/acs.iecr.9b02205.
(52) Zhou, L.; Wang, S.; Chen, Y.; Serre, C. Direct Synthesis of Robust Hcp UiO-66(Zr) MOF Using Poly(Ethylene Terephthalate) Waste as Ligand Source. *Microporous and Mesoporous Materials* **2019**, *290*, 109674. https://doi.org/10.1016/j.micromeso.2019.109674.
(53) Mourabet, M.; El Boujaady, H.; El Rhilassi, A.; Ramdane, H.; Bennani-Ziatni, M.; El Hamri, R.; Taitai, A. Defluoridation of Water Using Brushite: Equilibrium, Kinetic and Thermodynamic Studies. *Desalination*. Elsevier September 1, 2011, pp 1–9. https://doi.org/10.1016/j.desal.2011.05.068.
(54) Rahimi, M. R.; Mosleh, S. Application of the Supercritical Fluids (SCFs) in the Sorption Processes. In *Intensification of Sorption Processes*; Elsevier, 2022; pp 219–252. https://doi.org/10.1016/b978-0-12-821411-4.00001-8.

(55) Ayawei, N.; Ebelegi, A. N.; Wankasi, D. Modelling and Interpretation of Adsorption Isotherms. *Journal of Chemistry*. Hindawi Limited 2017. https://doi.org/10.1155/2017/3039817.
(56) Kalam, S.; Abu-Khamsin, S. A.; Kamal, M. S.; Patil, S. Surfactant Adsorption Isotherms: A Review. *ACS Omega*. American Chemical Society December 7, 2021, pp 32342–32348. https://doi.org/10.1021/acsomega.1c04661.
(57) Nethaji, S.; Sivasamy, A.; Mandal, A. B. Adsorption Isotherms, Kinetics and Mechanism for the Adsorption of Cationic and Anionic Dyes onto Carbonaceous Particles Prepared from Juglans Regia Shell Biomass. *International Journal of Environmental Science and Technology* **2013**, *10* (2), 231–242. https://doi.org/10.1007/s13762-012-0112-0.
(58) Wang, J.; Guo, X. Adsorption Kinetic Models: Physical Meanings, Applications, and Solving Methods. *Journal of Hazardous Materials*. Elsevier B.V. May 15, 2020, p 122156. https://doi.org/10.1016/j.jhazmat.2020.122156.
(59) Shah, G.; Sahota, S.; Vijay, V. K.; Pant, K. K.; Ghosh, P. Recent Developments in Pressure Swing Adsorption for Biomethane Production. In *Emerging Technologies and Biological Systems for Biogas Upgrading*; Elsevier, 2021; pp 93–116. https://doi.org/10.1016/B978-0-12-822808-1.00005-2.
(60) Kim, R. G.; Hwang, C. W.; Jeon, C. H. Kinetics of Coal Char Gasification with CO2: Impact of Internal/External Diffusion at High Temperature and Elevated Pressure. *Appl Energy* **2014**, *129*, 299–307. https://doi.org/10.1016/J.APENERGY.2014.05.011.
(61) Sahoo, T. R.; Prelot, B. Adsorption Processes for the Removal of Contaminants from Wastewater: The Perspective Role of Nanomaterials and Nanotechnology. *Nanomaterials for the Detection and Removal of Wastewater Pollutants* **2020**, 161–222. https://doi.org/10.1016/B978-0-12-818489-9.00007-4.
(62) Ray, S. S.; Gusain, R.; Kumar, N. Adsorption Equilibrium Isotherms, Kinetics and Thermodynamics. *Carbon Nanomaterial-Based Adsorbents for Water Purification* **2020**, 101–118. https://doi.org/10.1016/B978-0-12-821959-1.00005-2.
(63) Agbovi, H. K.; Wilson, L. D. Adsorption Processes in Biopolymer Systems: Fundamentals to Practical Applications. *Natural Polymers-Based Green Adsorbents for Water Treatment* **2021**, 1–51. https://doi.org/10.1016/B978-0-12-820541-9.00011-9.
(64) Taraba, B.; Bulavová, P. Second or Pseudo-Second-Order Model for Adsorption Kinetics? *Separation Science and Technology (Philadelphia)* **2022**, *57* (10), 1558–1562. https://doi.org/10.1080/01496395.2021.1998124.
(65) Zhang, J. Physical Insights into Kinetic Models of Adsorption. *Sep Purif Technol* **2019**, *229*, 115832. https://doi.org/10.1016/j.seppur.2019.115832.
(66) Wu, F. C.; Tseng, R. L.; Juang, R. S. Characteristics of Elovich Equation Used for the Analysis of Adsorption Kinetics in Dye-Chitosan Systems. *Chemical Engineering Journal* **2009**, *150* (2–3), 366–373. https://doi.org/10.1016/j.cej.2009.01.014.

(67) Marsh, H.; Rodríguez-Reinoso, F. Characterization of Activated Carbon. *Activated Carbon* **2006**, 143–242. https://doi.org/10.1016/B978-008044463-5/50018-2.
(68) Pal, P. Adsorption Method of Arsenic Separation from Water. *Groundwater Arsenic Remediation* **2015**, 71–104. https://doi.org/10.1016/B978-0-12-801281-9.00003-5.
(69) Sabouni, R.; Kazemian, H.; Rohani, S. Mathematical Modeling and Experimental Breakthrough Curves of Carbon Dioxide Adsorption on Metal Organic Framework CPM-5. *Environ Sci Technol* **2013**, *47* (16), 9372–9380. https://doi.org/10.1021/ES401276R/SUPPL_FILE/ES401276R_SI_001.PDF .
(70) *Sustainable Chemistry - IUPAC | International Union of Pure and Applied Chemistry*. https://iupac.org/who-we-are/committees/sustainable-chemistry/ (accessed 2022-10-23).
(71) Anastas, P.; Eghbali, N. Green Chemistry: Principles and Practice. *Chem Soc Rev* **2010**, *39* (1), 301–312. https://doi.org/10.1039/b918763b.
(72) Sheldon, R. A. Metrics of Green Chemistry and Sustainability: Past, Present, and Future. *ACS Sustain Chem Eng* **2018**, *6* (1), 32–48. https://doi.org/10.1021/acssuschemeng.7b03505.
(73) DeVierno Kreuder, A.; House-Knight, T.; Whitford, J.; Ponnusamy, E.; Miller, P.; Jesse, N.; Rodenborn, R.; Sayag, S.; Gebel, M.; Aped, I.; Sharfstein, I.; Manaster, E.; Ergaz, I.; Harris, A.; Nelowet Grice, L. A Method for Assessing Greener Alternatives between Chemical Products Following the 12 Principles of Green Chemistry. *ACS Sustain Chem Eng* **2017**, *5* (4), 2927–2935. https://doi.org/10.1021/acssuschemeng.6b02399.
(74) Kong, X.-J.; Li, J.-R. An Overview of Metal–Organic Frameworks for Green Chemical Engineering. *Engineering* **2021**, *7* (8), 1115–1139. https://doi.org/10.1016/j.eng.2021.07.001.
(75) Zhang, J.; White, G. B.; Ryan, M. D.; Hunt, A. J.; Katz, M. J. Dihydrolevoglucosenone (Cyrene) As a Green Alternative to N,N-Dimethylformamide (DMF) in MOF Synthesis. *ACS Sustain Chem Eng* **2016**, *4* (12), 7186–7192. https://doi.org/10.1021/acssuschemeng.6b02115.
(76) Selva, M.; Perosa, A. Green Chemistry Metrics: A Comparative Evaluation of Dimethyl Carbonate, Methyl Iodide, Dimethyl Sulfate and Methanol as Methylating Agents. *Green Chemistry* **2008**, *10* (4), 457–46. https://doi.org/10.1039/b713985c.
(77) Sepúlveda-Cervantes, C. V.; Soto-Regalado, E.; Rivas-García, P.; Loredo-Cancino, M.; Cerino-Córdova, F. d. J.; García Reyes, R. B. Technical-Environmental Optimisation of the Activated Carbon Production of an Agroindustrial Waste by Means Response Surface and Life Cycle Assessment. *Waste Management and Research* **2018**, *36* (2), 121–130. https://doi.org/10.1177/0734242X17741680.
(78) *ISO - ISO 14040:2006 - Environmental management — Life cycle assessment — Principles and framework*. https://www.iso.org/standard/37456.html (accessed 2022-10-05).

(79) Huijbregts, M. A. J.; Steinmann, Z. J. N.; Elshout, P. M. F.; Stam, G.; Verones, F.; Vieira, M.; Zijp, M.; Hollander, A.; van Zelm, R. ReCiPe2016: A Harmonised Life Cycle Impact Assessment Method at Midpoint and Endpoint Level. *International Journal of Life Cycle Assessment* **2017**, *22* (2), 138–147. https://doi.org/10.1007/s11367-016-1246-y.

(80) Loya-González, D.; Loredo-Cancino, M.; Soto-Regalado, E.; Rivas-García, P.; Cerino-Córdova, F. de J.; García-Reyes, R. B.; Bustos-Martínez, D.; Estrada-Baltazar, A. Optimal Activated Carbon Production from Corn Pericarp: A Life Cycle Assessment Approach. *J Clean Prod* **2019**, *219*, 316–325. https://doi.org/10.1016/j.jclepro.2019.02.068.

(81) Grande, C. A.; Blom, R.; Spjelkavik, A.; Moreau, V.; Payet, J. Life-Cycle Assessment as a Tool for Eco-Design of Metal-Organic Frameworks (MOFs). *Sustainable Materials and Technologies* **2017**, *14* (October), 11–18. https://doi.org/10.1016/j.susmat.2017.10.002.

(82) Pioquinto-García, S.; Rosas, J. M.; Loredo-Cancino, M.; Giraudet, S.; Soto-Regalado, E.; Rivas-García, P.; Dávila-Guzmán, N. E. Environmental Assessment of Metal-Organic Framework DUT-4 Synthesis and Its Application for Siloxane Removal. *J Environ Chem Eng* **2021**, *9* (6). https://doi.org/10.1016/j.jece.2021.106601.

(83) DeVierno Kreuder, A.; House-Knight, T.; Whitford, J.; Ponnusamy, E.; Miller, P.; Jesse, N.; Rodenborn, R.; Sayag, S.; Gebel, M.; Aped, I.; Sharfstein, I.; Manaster, E.; Ergaz, I.; Harris, A.; Nelowet Grice, L. A Method for Assessing Greener Alternatives between Chemical Products Following the 12 Principles of Green Chemistry. *ACS Sustain Chem Eng* **2017**, *5* (4), 2927–2935. https://doi.org/10.1021/acssuschemeng.6b02399.

(84) Anastas, P.; Eghbali, N. Green Chemistry: Principles and Practice. *Chem Soc Rev* **2010**, *39* (1), 301–312. https://doi.org/10.1039/b918763b.

(85) Nowrouzi, M.; Abyar, H.; Younesi, H.; Khaki, E. Life Cycle Environmental and Economic Assessment of Highly Efficient Carbon-Based CO2adsorbents: A Comparative Study. *Journal of CO2 Utilization* **2021**, *47*, 101491. https://doi.org/10.1016/j.jcou.2021.101491.

(86) Meramo-Hurtado, S. I.; González-Delgado, Á. D. Application of Techno-Economic and Sensitivity Analyses as Decision-Making Tools for Assessing Emerging Large-Scale Technologies for Production of Chitosan-Based Adsorbents. *ACS Omega* **2020**, *5* (28), 17601–17610. https://doi.org/10.1021/acsomega.0c02064.

(87) Meramo-Hurtado, S. I.; González-Delgado, Á. D. Application of Techno-Economic and Sensitivity Analyses as Decision-Making Tools for Assessing Emerging Large-Scale Technologies for Production of Chitosan-Based Adsorbents. *ACS Omega* **2020**, *5* (28), 17601–17610. https://doi.org/10.1021/acsomega.0c02064.

(88) Nowrouzi, M.; Abyar, H.; Younesi, H.; Khaki, E. Life Cycle Environmental and Economic Assessment of Highly Efficient Carbon-Based CO2adsorbents: A Comparative Study. *Journal of CO2 Utilization* **2021**, *47*, 101491. https://doi.org/10.1016/j.jcou.2021.101491.

(89) Sinha, A.; Thakkar, H.; Rezaei, F.; Kawajiri, Y.; Realff, M. J. Direct Air Capture of CO2 in Enclosed Environments: Design under Uncertainty and Techno-Economic Analysis. In *Computer Aided Chemical Engineering*; Elsevier B.V., 2018; Vol. 44, pp 2179–2184. https://doi.org/10.1016/B978-0-444-64241-7.50358-X.
(90) Yang, J.; Bai, H.; Zhang, F.; Liu, J.; Winarta, J.; Wang, Y.; Mu, B. Effects of Activation Temperature and Densification on Adsorption Performance of MOF MIL-100(Cr). *J Chem Eng Data* **2019**, *64* (12), 5814–5823. https://doi.org/10.1021/acs.jced.9b00770.
(91) Lawson, S.; Al-Naddaf, Q.; Newport, K.; Rownaghi, A.; Rezaei, F. Assessment of CO2/CH4Separation Performance of 3D-Printed Carbon Monoliths in Pressure Swing Adsorption. *Ind Eng Chem Res* **2021**, *60* (45), 16445–16456. https://doi.org/10.1021/ACS.IECR.1C01741/SUPPL_FILE/IE1C01741_SI_001.PDF.
(92) Zheng, J.; Cui, X.; Yang, Q.; Ren, Q.; Yang, Y.; Xing, H. Shaping of Ultrahigh-Loading MOF Pellet with a Strongly Anti-Tearing Binder for Gas Separation and Storage. *Chemical Engineering Journal* **2018**, *354*, 1075–1082. https://doi.org/10.1016/j.cej.2018.08.119.
(93) Peterson, G. W.; Decoste, J. B.; Glover, T. G.; Huang, Y.; Jasuja, H.; Walton, K. S. Effects of Pelletization Pressure on the Physical and Chemical Properties of the Metal-Organic Frameworks Cu3(BTC)2 and UiO-66. *Microporous and Mesoporous Materials* **2013**, *179*, 48–53. https://doi.org/10.1016/j.micromeso.2013.02.025.
(94) Akhtar, F.; Andersson, L.; Ogunwumi, S.; Hedin, N.; Bergström, L. Structuring Adsorbents and Catalysts by Processing of Porous Powders. *J Eur Ceram Soc* **2014**, *34* (7), 1643–1666. https://doi.org/10.1016/j.jeurceramsoc.2014.01.008.
(95) Majchrzak-Kucęba, I.; Ściubidło, A. Shaping Metal–Organic Framework (MOF) Powder Materials for CO2 Capture Applications—a Thermogravimetric Study. *J Therm Anal Calorim* **2019**, 1–6. https://doi.org/10.1007/s10973-019-08314-5.
(96) Cousin-Saint-Remi, J.; Finoulst, A.-L.; Jabbour, C.; Baron, G. V.; Denayer, J. F. M. Selection of Binder Recipes for the Formulation of MOFs into Resistant Pellets for Molecular Separations by Fixed-Bed Adsorption. *Microporous and Mesoporous Materials* **2020**, *304*, 109322. https://doi.org/10.1016/j.micromeso.2019.02.009.
(97) Zheng, J.; Cui, X.; Yang, Q.; Ren, Q.; Yang, Y.; Xing, H. Shaping of Ultrahigh-Loading MOF Pellet with a Strongly Anti-Tearing Binder for Gas Separation and Storage. *Chemical Engineering Journal* **2018**, *354*, 1075–1082. https://doi.org/10.1016/j.cej.2018.08.119.
(98) Li, L.; Yao, J.; Xiao, P.; Shang, J.; Feng, Y.; Webley, P. A.; Wang, H. One-Step Fabrication of ZIF-8/Polymer Composite Spheres by a Phase Inversion Method for Gas Adsorption. *Colloid Polym Sci* **2013**, *291* (11), 2711–2717. https://doi.org/10.1007/s00396-013-3024-8.

(99) Zhu, H.; Zhang, Q.; Zhu, S. Preparation of Raspberry-like ZIF-8/PS Composite Spheres via Dispersion Polymerization. *Dalton Transactions* **2015**, *44* (38), 16752–16757. https://doi.org/10.1039/c5dt02627j.
(100) Avci-Camur, C.; Troyano, J.; Pérez-Carvajal, J.; Legrand, A.; Farrusseng, D.; Imaz, I.; Maspoch, D. Aqueous Production of Spherical Zr-MOF Beads: Via Continuous-Flow Spray-Drying. *Green Chemistry* **2018**, *20* (4), 873–878. https://doi.org/10.1039/c7gc03132g.
(101) Mondino, G.; Spjelkavik, A. I.; Didriksen, T.; Krishnamurthy, S.; Stensrød, R. E.; Grande, C. A.; Nord, L. O.; Blom, R. Production of MOF Adsorbent Spheres and Comparison of Their Performance with Zeolite 13X in a Moving-Bed TSA Process for Postcombustion CO2 Capture. *Ind Eng Chem Res* **2020**, *59* (15), 7198–7211. https://doi.org/10.1021/acs.iecr.9b06387.
(102) Gama, M. R.; Rocha, F. R. P.; Bottoli, C. B. G. Monoliths: Synthetic Routes, Functionalization and Innovative Analytical Applications. *TrAC - Trends in Analytical Chemistry* **2019**, *115*, 39–51. https://doi.org/10.1016/j.trac.2019.03.020.
(103) Ramos-Fernandez, E. V.; Garcia-Domingos, M.; Juan-Alcañiz, J.; Gascon, J.; Kapteijn, F. MOFs Meet Monoliths: Hierarchical Structuring Metal Organic Framework Catalysts. *Appl Catal A Gen* **2011**, *391* (1–2), 261–267. https://doi.org/10.1016/j.apcata.2010.05.019.
(104) Govender, S.; Friedrich, H. B. Monoliths: A Review of the Basics, Preparation Methods and Their Relevance to Oxidation. *Catalysts* **2017**, *7* (2). https://doi.org/10.3390/catal7020062.
(105) Hong, W. Y.; Perera, S. P.; Burrows, A. D. Manufacturing of Metal-Organic Framework Monoliths and Their Application in CO2 Adsorption. *Microporous and Mesoporous Materials* **2015**, *214*, 149–155. https://doi.org/10.1016/j.micromeso.2015.05.014.
(106) Rezaei, F.; Lawson, S.; Hosseini, H.; Thakkar, H.; Hajari, A.; Monjezi, S.; Rownaghi, A. A. MOF-74 and UTSA-16 Film Growth on Monolithic Structures and Their CO2 Adsorption Performance. *Chemical Engineering Journal* **2017**, *313*, 1346–1353. https://doi.org/10.1016/j.cej.2016.11.058.
(107) Ramos-Fernandez, E. V.; Garcia-Domingos, M.; Juan-Alcañiz, J.; Gascon, J.; Kapteijn, F. MOFs Meet Monoliths: Hierarchical Structuring Metal Organic Framework Catalysts. *Appl Catal A Gen* **2011**, *391* (1–2), 261–267. https://doi.org/10.1016/j.apcata.2010.05.019.
(108) Zacharia, R.; Cossement, D.; Lafi, L.; Chahine, R. Volumetric Hydrogen Sorption Capacity of Monoliths Prepared by Mechanical Densification of MOF-177. *J Mater Chem* **2010**, *20* (11), 2145–2151. https://doi.org/10.1039/b922991d.
(109) Küsgens, P.; Zgaverdea, A.; Fritz, H. G.; Siegle, S.; Kaskel, S. Metal-Organic Frameworks in Monolithic Structures. *Journal of the American Ceramic Society* **2010**, *93* (9), 2476–2479. https://doi.org/10.1111/j.1551-2916.2010.03824.x.
(110) Hong, W. Y.; Perera, S. P.; Burrows, A. D. Comparison of MIL-101(Cr) Metal-Organic Framework and 13X Zeolite Monoliths for CO2 Capture.

Microporous and Mesoporous Materials **2020**, *308* (August), 110525. https://doi.org/10.1016/j.micromeso.2020.110525.
(111) Thakkar, H.; Eastman, S.; Al-Naddaf, Q.; Rownaghi, A. A.; Rezaei, F. 3D-Printed Metal-Organic Framework Monoliths for Gas Adsorption Processes. *ACS Appl Mater Interfaces* **2017**, *9* (41), 35908–35916. https://doi.org/10.1021/acsami.7b11626.
(112) Lefevere, J.; Claessens, B.; Mullens, S.; Baron, G.; Cousin-Saint-Remi, J.; Denayer, J. F. M. 3D-Printed Zeolitic Imidazolate Framework Structures for Adsorptive Separations. *ACS Appl Nano Mater* **2019**, *2* (8), 4991–4999. https://doi.org/10.1021/acsanm.9b00934.
(113) Kreider, M. C.; Sefa, M.; Fedchak, J. A.; Scherschligt, J.; Bible, M.; Natarajan, B.; Klimov, N. N.; Miller, A. E.; Ahmed, Z.; Hartings, M. R. Toward 3D Printed Hydrogen Storage Materials Made with ABS-MOF Composites. *Polym Adv Technol* **2018**, *29* (2), 867–873. https://doi.org/10.1002/pat.4197.
(114) Vikrant, K.; Na, C. J.; Younis, S. A.; Kim, K. H.; Kumar, S. Evidence for Superiority of Conventional Adsorbents in the Sorptive Removal of Gaseous Benzene under Real-World Conditions: Test of Activated Carbon against Novel Metal-Organic Frameworks. *J Clean Prod* **2019**, *235*, 1090–1102. https://doi.org/10.1016/j.jclepro.2019.07.038.
(115) Zhao, Z.; Li, X.; Huang, S.; Xia, Q.; Li, Z. Adsorption and Diffusion of Benzene on Chromium-Based Metal Organic Framework MIL-101 Synthesized by Microwave Irradiation. *Ind Eng Chem Res* **2011**, *50* (4), 2254–2261. https://doi.org/10.1021/ie101414n.
(116) Dedecker, K.; Dumas, E.; Lavédrine, B.; Steunou, N.; Serre, C. *Metal-Organic Frameworks for the Capture of Volatile Organic Compounds and Toxic Chemicals*; 2019. https://doi.org/10.1016/b978-0-12-814633-0.00007-7.
(117) Bahri, M.; Haghighat, F.; Kazemian, H.; Rohani, S. A Comparative Study on Metal Organic Frameworks for Indoor Environment Application: Adsorption Evaluation. *Chemical Engineering Journal* **2017**, *313*, 711–723. https://doi.org/10.1016/j.cej.2016.10.004.
(118) Shafiei, M.; Alivand, M. S.; Rashidi, A.; Samimi, A.; Mohebbi-Kalhori, D. Synthesis and Adsorption Performance of a Modified Micro-Mesoporous MIL-101(Cr) for VOCs Removal at Ambient Conditions. *Chemical Engineering Journal* **2018**, *341* (December 2017), 164–174. https://doi.org/10.1016/j.cej.2018.02.027.
(119) Kurisingal, J. F.; Li, Y.; Sagynbayeva, Y.; Chitumalla, R. K.; Vuppala, S.; Rachuri, Y.; Gu, Y.; Jang, J.; Park, D.-W. Porous Aluminum-Based DUT Metal-Organic Frameworks for the Transformation of CO2 into Cyclic Carbonates: A Computationally Supported Study. *Catal Today* **2020**, *352*, 227–236. https://doi.org/10.1016/j.cattod.2019.12.038.
(120) Yang, K.; Sun, Q.; Xue, F.; Lin, D. Adsorption of Volatile Organic Compounds by Metal-Organic Frameworks MIL-101: Influence of Molecular Size and Shape. *J Hazard Mater* **2011**, *195*, 124–131. https://doi.org/10.1016/j.jhazmat.2011.08.020.

(121) Zhao, T.; Yang, L.; Feng, P.; Gruber, I.; Janiak, C.; Liu, Y. Facile Synthesis of Nano-Sized MIL-101(Cr) with the Addition of Acetic Acid. *Inorganica Chim Acta* **2018**, *471*, 440–445. https://doi.org/10.1016/j.ica.2017.11.030.
(122) Zhao, Z.; Li, X.; Huang, S.; Xia, Q.; Li, Z. Adsorption and Diffusion of Benzene on Chromium-Based Metal Organic Framework MIL-101 Synthesized by Microwave Irradiation. **2011**, 2254–2261.
(123) Mellot-Draznieks, C.; Férey, G. Assembling Molecular Species into 3D Frameworks: Computational Design and Structure Solution of Hybrid Materials. *Progress in Solid State Chemistry* **2005**, *33* (2-4 SPEC. ISS.), 187–197. https://doi.org/10.1016/j.progsolidstchem.2005.11.047.
(124) Zhao, Z.; Li, X.; Huang, S.; Xia, Q.; Li, Z. Adsorption and Diffusion of Benzene on Chromium-Based Metal Organic Framework MIL-101 Synthesized by Microwave Irradiation. **2011**, 2254–2261.
(125) Luo, H.; Cheng, F.; Huelsenbeck, L.; Smith, N. Comparison between Conventional Solvothermal and Aqueous Solution-Based Production of UiO-66-NH2: Life Cycle Assessment, Techno-Economic Assessment, and Implications for CO2capture and Storage. *J Environ Chem Eng* **2021**, *9* (2), 105159. https://doi.org/10.1016/j.jece.2021.105159.
(126) Thakkar, H.; Lawson, S.; Rownaghi, A. A.; Rezaei, F. Development of 3D-Printed Polymer-Zeolite Composite Monoliths for Gas Separation. *Chemical Engineering Journal* **2018**, *348* (April), 109–116. https://doi.org/10.1016/j.cej.2018.04.178.
(127) Lawson, S.; Adebayo, B.; Robinson, C.; Al-Naddaf, Q.; Rownaghi, A. A.; Rezaei, F. The Effects of Cell Density and Intrinsic Porosity on Structural Properties and Adsorption Kinetics in 3D-Printed Zeolite Monoliths. *Chem Eng Sci* **2020**, *218*, 115564. https://doi.org/10.1016/j.ces.2020.115564.
(128) Claessens, B.; Dubois, N.; Lefevere, J.; Mullens, S.; Cousin-Saint-Remi, J.; Denayer, J. F. M. 3D-Printed ZIF-8 Monoliths for Biobutanol Recovery. *Ind Eng Chem Res* **2020**, *59* (18), 8813–8824. https://doi.org/10.1021/acs.iecr.0c00453.
(129) Lefevere, J.; Claessens, B.; Mullens, S.; Baron, G.; Cousin-saint-remi, J.; Denayer, J. F. M. 3D-Printed Zeolitic Imidazolate Framework Structures for Adsorptive Separations. **2019**. https://doi.org/10.1021/acsanm.9b00934.
(130) Sheikh Alivand, M.; Hossein Tehrani, N. H. M.; Shafiei-Alavijeh, M.; Rashidi, A.; Kooti, M.; Pourreza, A.; Fakhraie, S. Synthesis of a Modified HF-Free MIL-101(Cr) Nanoadsorbent with Enhanced H 2 S/CH 4 , CO 2 /CH 4, and CO 2 /N 2 Selectivity. *J Environ Chem Eng* **2019**, *7* (2), 102946. https://doi.org/10.1016/j.jece.2019.102946.
(131) DeVierno Kreuder, A.; House-Knight, T.; Whitford, J.; Ponnusamy, E.; Miller, P.; Jesse, N.; Rodenborn, R.; Sayag, S.; Gebel, M.; Aped, I.; Sharfstein, I.; Manaster, E.; Ergaz, I.; Harris, A.; Nelowet Grice, L. A Method for Assessing Greener Alternatives between Chemical Products Following the 12 Principles of Green Chemistry. *ACS Sustain Chem Eng* **2017**, *5* (4), 2927–2935. https://doi.org/10.1021/acssuschemeng.6b02399.

(132) *ISO - ISO 14040:2006 - Environmental management — Life cycle assessment — Principles and framework*. https://www.iso.org/standard/37456.html (accessed 2022-10-04).
(133) Pioquinto-García, S.; Rosas, J. M.; Loredo-Cancino, M.; Giraudet, S.; Soto-Regalado, E.; Rivas-García, P.; Dávila-Guzmán, N. E. Environmental Assessment of Metal-Organic Framework DUT-4 Synthesis and Its Application for Siloxane Removal. *J Environ Chem Eng* **2021**, *9* (6). https://doi.org/10.1016/j.jece.2021.106601.
(134) Grande, C. A.; Blom, R.; Spjelkavik, A.; Moreau, V.; Payet, J. Life-Cycle Assessment as a Tool for Eco-Design of Metal-Organic Frameworks (MOFs). *Sustainable Materials and Technologies* **2017**, *14* (October), 11–18. https://doi.org/10.1016/j.susmat.2017.10.002.
(135) Sepúlveda-Cervantes, C. V.; Soto-Regalado, E.; Rivas-García, P.; Loredo-Cancino, M.; Cerino-Córdova, F. d. J.; García Reyes, R. B. Technical-Environmental Optimisation of the Activated Carbon Production of an Agroindustrial Waste by Means Response Surface and Life Cycle Assessment. *Waste Management and Research* **2018**, *36* (2), 121–130. https://doi.org/10.1177/0734242X17741680.
(136) Pioquinto-García, S.; Rosas, J. M.; Loredo-Cancino, M.; Giraudet, S.; Soto-Regalado, E.; Rivas-García, P.; Dávila-Guzmán, N. E. Environmental Assessment of Metal-Organic Framework DUT-4 Synthesis and Its Application for Siloxane Removal. *J Environ Chem Eng* **2021**, *9* (6). https://doi.org/10.1016/j.jece.2021.106601.
(137) *ISO - ISO 14040:2006 - Environmental management — Life cycle assessment — Principles and framework*. https://www.iso.org/standard/37456.html (accessed 2022-10-04).
(138) Huijbregts, M. A. J.; Steinmann, Z. J. N.; Elshout, P. M. F.; Stam, G.; Verones, F.; Vieira, M.; Zijp, M.; Hollander, A.; van Zelm, R. ReCiPe2016: A Harmonised Life Cycle Impact Assessment Method at Midpoint and Endpoint Level. *International Journal of Life Cycle Assessment* **2017**, *22* (2), 138–147. https://doi.org/10.1007/s11367-016-1246-y.
(139) *CONAC | Normatividad Vigente*. https://www.conac.gob.mx/es/CONAC/Normatividad_Vigente (accessed 2022-07-11).
(140) Heidari, A.; Boleydei, H.; Rohani, A.; Lu, H. R.; Younesi, H. Integrating Life Cycle Assessment and Life Cycle Costing Using TOPSIS to Select Sustainable Biomass-Based -Carbonaceous Adsorbents for CO2 Capture. *J Clean Prod* **2022**, *357*. https://doi.org/10.1016/j.jclepro.2022.131968.
(141) Liang, H.; Ren, J.; Gao, S.; Dong, L.; Gao, Z. Comparison of Different Multicriteria Decision-Making Methodologies for Sustainability Decision Making. *Hydrogen Economy: Supply Chain, Life Cycle Analysis and Energy Transition for Sustainability* **2017**, 189–224. https://doi.org/10.1016/B978-0-12-811132-1.00008-0.
(142) Teodorović, D.; Janić, M. Traffic and Transportation Analysis Techniques. *Transportation Engineering* **2017**, 63–162. https://doi.org/10.1016/B978-0-12-803818-5.00003-2.

(143) Iacomi, P.; Gulcay, E.; Pires Conti, P.; Biswas, S.; Steunou, N.; Maurin, G.; Rioland, G.; Devautour-Vinot, S. MIL-101(Cr) MOF as an Effective Siloxane Sensor. *ACS Appl Mater Interfaces* **2022**, *14* (15), 17531–17538. https://doi.org/10.1021/acsami.2c02607.
(144) Shi, E.; Yu, G.; Lin, H.; Liang, C.; Zhang, T.; Zhang, F.; Qu, F. The Incorporation of Bismuth(III) into Metal-Organic Frameworks for Electrochemical Detection of Trace Cadmium(II) and Lead(II). *Microchimica Acta* **2019**, *186* (7), 451. https://doi.org/10.1007/s00604-019-3522-6.
(145) Mansur, A. A. P.; de Carvalho, F. G.; Mansur, R. L.; Carvalho, S. M.; de Oliveira, L. C.; Mansur, H. S. Carboxymethylcellulose/ZnCdS Fluorescent Quantum Dot Nanoconjugates for Cancer Cell Bioimaging. *Int J Biol Macromol* **2017**, *96*, 675–686. https://doi.org/10.1016/j.ijbiomac.2016.12.078.
(146) Li, L.; Wang, F.; Shao, Z.; Liu, J.; Zhang, Q.; Jiao, W. Chitosan and Carboxymethyl Cellulose-Multilayered Magnetic Fluorescent Systems for Reversible Protein Immobilization. *Carbohydr Polym* **2018**, *201*, 357–366. https://doi.org/10.1016/j.carbpol.2018.08.088.
(147) Zhang, F.; Jin, Y.; Fu, Y.; Zhong, Y.; Zhu, W.; Ibrahim, A. A.; El-Shall, M. S. Palladium Nanoparticles Incorporated within Sulfonic Acid-Functionalized MIL-101(Cr) for Efficient Catalytic Conversion of Vanillin. *J Mater Chem A Mater* **2015**, *3* (33), 17008–17015. https://doi.org/10.1039/c5ta03524d.
(148) Mu, L.; Zhang, L.; Zhu, K.; Ma, J.; Ifran, M.; Li, A. Anaerobic Co-Digestion of Sewage Sludge, Food Waste and Yard Waste: Synergistic Enhancement on Process Stability and Biogas Production. *Science of the Total Environment* **2020**, *704*, 135429. https://doi.org/10.1016/j.scitotenv.2019.135429.
(149) Jangodaz, E.; Alaie, E.; Safekordi, A. A.; Tasharrofi, S. Adsorption of Ethylbenzene from Air on Metal–Organic Frameworks MIL-101(Cr) and MIL-53(Fe) at Room Temperature. *J Inorg Organomet Polym Mater* **2018**, *28* (5), 2090–2099. https://doi.org/10.1007/s10904-018-0896-6.
(150) Tan, B.; Luo, Y.; Liang, X.; Wang, S.; Gao, X.; Zhang, Z.; Fang, Y. Composite Salt in MIL-101(Cr) with High Water Uptake and Fast Adsorption Kinetics for Adsorption Heat Pumps. *Microporous and Mesoporous Materials* **2019**, *286* (April), 141–148. https://doi.org/10.1016/j.micromeso.2019.05.039.
(151) Férey, C.; Mellot-Draznieks, C.; Serre, C.; Millange, F.; Dutour, J.; Surblé, S.; Margiolaki, I. Chemistry: A Chromium Terephthalate-Based Solid with Unusually Large Pore Volumes and Surface Area. *Science (1979)* **2005**, *309* (5743), 2040–2042. https://doi.org/10.1126/science.1116275.
(152) Lo, S. H.; Senthil Raja, D.; Chen, C. W.; Kang, Y. H.; Chen, J. J.; Lin, C. H. Waste Polyethylene Terephthalate (PET) Materials as Sustainable Precursors for the Synthesis of Nanoporous MOFs, MIL-47, MIL-53(Cr, Al, Ga) and MIL-101(Cr). *Dalton Transactions* **2016**, *45* (23), 9565–9573. https://doi.org/10.1039/c6dt01282e.
(153) Zorainy, M. Y.; Gar Alalm, M.; Kaliaguine, S.; Boffito, D. C. Revisiting the MIL-101 Metal-Organic Framework: Design, Synthesis, Modifications, Advances, and Recent Applications. *J Mater Chem A Mater* **2021**, *9* (39), 22159–22217. https://doi.org/10.1039/d1ta06238g.

(154) Zhao, H.; Li, Q.; Wang, Z.; Wu, T.; Zhang, M. Synthesis of MIL-101(Cr) and Its Water Adsorption Performance. *Microporous and Mesoporous Materials* **2020**, *297*, 110044. https://doi.org/10.1016/J.MICROMESO.2020.110044.
(155) Mousavi, S.; Zeinali, S. VOC s Detection Using Resistive Gas Nanosensor Based on MIL-101(Cr) as a Metal Organic Framework. *Sens Actuators A Phys* **2022**, *346*, 113810. https://doi.org/10.1016/J.SNA.2022.113810.
(156) Reinsch, H. "Green" Synthesis of Metal-Organic Frameworks. *Eur J Inorg Chem* **2016**, *2016* (27), 4290–4299. https://doi.org/10.1002/ejic.201600286.
(157) Schukraft, G.; Petit, C. *Green Synthesis and Engineering Applications of Metal-Organic Frameworks*; Szekely, G., Livingston, A., Eds.; Elsevier, 2020. https://doi.org/10.1016/B978-0-12-814681-1.00006-0.
(158) Ardila-Fierro, K. J.; Hernández, J. G. Sustainability Assessment of Mechanochemistry by Using the Twelve Principles of Green Chemistry. *ChemSusChem* **2021**, *14* (10), 2145–2162. https://doi.org/10.1002/cssc.202100478.
(159) Fu, J.; Wu, Y. nan. A Showcase of Green Chemistry: Sustainable Synthetic Approach of Zirconium-Based MOF Materials. *Chemistry - A European Journal* **2021**, *27* (39), 9967–9987. https://doi.org/10.1002/chem.202005151.
(160) Kumar, S.; Jain, S.; Nehra, M.; Dilbaghi, N.; Marrazza, G.; Kim, K. H. Green Synthesis of Metal–Organic Frameworks: A State-of-the-Art Review of Potential Environmental and Medical Applications. *Coord Chem Rev* **2020**, *420*, 213407. https://doi.org/10.1016/j.ccr.2020.213407.
(161) IARC MONOGRAPHS. Some Industrial Chemicals: IARC Monographs on the Evaluation of Carcinogenic Risks to Humans. *IARC Monogr Eval Carcinog Risks Hum* **2018**, *115*, 119–170.
(162) Venturi, D. M.; Campana, F.; Marmottini, F.; Costantino, F.; Vaccaro, L. Extensive Screening of Green Solvents for Safe and Sustainable UiO-66 Synthesis. *ACS Sustain Chem Eng* **2020**, *8* (46), 17154–17164. https://doi.org/10.1021/acssuschemeng.0c05587.
(163) Eftaiha, A. F.; Qaroush, A. K.; Abu-Daabes, M. A.; Alsyouri, H. M.; Assaf, K. I. New Metrics of Green Sorbents for CO2 Capturing. *Adv Sustain Syst* **2020**, *4* (7), 1–15. https://doi.org/10.1002/adsu.201900121.
(164) García-Quintero, A.; Palencia, M. A Critical Analysis of Environmental Sustainability Metrics Applied to Green Synthesis of Nanomaterials and the Assessment of Environmental Risks Associated with the Nanotechnology. *Science of the Total Environment* **2021**, *793*, 148524. https://doi.org/10.1016/j.scitotenv.2021.148524.
(165) Peh, S. B.; Wang, Y.; Zhao, D. Scalable and Sustainable Synthesis of Advanced Porous Materials. *ACS Sustain Chem Eng* **2019**, *7* (4), 3647–3670. https://doi.org/10.1021/acssuschemeng.8b05463.
(166) Sajid, M.; Płotka-Wasylka, J. Green Analytical Chemistry Metrics: A Review. *Talanta* **2021**, *238* (October 2021), 123046. https://doi.org/10.1016/j.talanta.2021.123046.
(167) Pioquinto-García, S.; Rosas, J. M.; Loredo-Cancino, M.; Giraudet, S.; Soto-Regalado, E.; Rivas-García, P.; Dávila-Guzmán, N. E. Environmental Assessment of Metal-Organic Framework DUT-4 Synthesis and Its

Application for Siloxane Removal. *J Environ Chem Eng* **2021**, *9* (6). https://doi.org/10.1016/j.jece.2021.106601.
(168) Julien, P. A.; Mottillo, C.; Friščić, T. Metal-Organic Frameworks Meet Scalable and Sustainable Synthesis. *Green Chemistry* **2017**, *19* (12), 2729–2747. https://doi.org/10.1039/c7gc01078h.
(169) Vogel, G. H. Process Development, 2. Evaluation. *Ullmann's Encyclopedia of Industrial Chemistry* **2011**. https://doi.org/10.1002/14356007.O22_O01.
(170) Piccinno, F.; Hischier, R.; Saba, A.; Mitrano, D.; Seeger, S.; Som, C. Multi-Perspective Application Selection: A Method to Identify Sustainable Applications for New Materials Using the Example of Cellulose Nanofiber Reinforced Composites. *J Clean Prod* **2016**, *112*, 1199–1210. https://doi.org/10.1016/j.jclepro.2015.06.105.
(171) Luo, H.; Cheng, F.; Huelsenbeck, L.; Smith, N. Comparison between Conventional Solvothermal and Aqueous Solution-Based Production of UiO-66-NH2: Life Cycle Assessment, Techno-Economic Assessment, and Implications for CO2capture and Storage. *J Environ Chem Eng* **2021**, *9* (2), 105159. https://doi.org/10.1016/j.jece.2021.105159.
(172) DeSantis, D.; Mason, J. A.; James, B. D.; Houchins, C.; Long, J. R.; Veenstra, M. Techno-Economic Analysis of Metal-Organic Frameworks for Hydrogen and Natural Gas Storage. *Energy and Fuels* **2017**, *31* (2), 2024–2032. https://doi.org/10.1021/acs.energyfuels.6b02510.
(173) *MIL-101 (Cr), Chromium-based MOFs (Cr-MOF) - CD Bioparticles*. https://www.cd-bioparticles.net/p/9151/mil-101-cr (accessed 2022-11-27).
(174) *MIL-101（Cr),Materials of Institut Lavoisier-101（Chromium） - Ruixibiotech*. http://ruixibiotech.com/pts/mil-101 (accessed 2022-11-27).
(175) Yu, H.; Chang, X.; Liu, W. Cost-Based Subsidy and Performance-Based Subsidy in a Manufacturing-Recycling System Considering Product Eco-Design. *J Clean Prod* **2021**, *327*, 129391. https://doi.org/10.1016/J.JCLEPRO.2021.129391.
(176) Wang, A.; Dangleben, N. L.; Dodge, D. E.; Silva, R. M. *Toluene Reference Exposure Levels*. Office of Environmental Health Hazard Assessment. https://oehha.ca.gov/media/downloads/crnr/noncancertsdfinal.pdf.
(177) Hazrati, S.; Rostami, R.; Farjaminezhad, M.; Fazlzadeh, M. Preliminary Assessment of BTEX Concentrations in Indoor Air of Residential Buildings and Atmospheric Ambient Air in Ardabil, Iran. *Atmos Environ* **2016**, *132*, 91–97. https://doi.org/10.1016/j.atmosenv.2016.02.042.
(178) Marsh, H.; Rodríguez-Reinoso, F. Characterization of Activated Carbon. In *Activated Carbon*; Elsevier, 2006; pp 143–242. https://doi.org/10.1016/b978-008044463-5/50018-2.
(179) Zhao, T.; Jeremias, F.; Boldog, I.; Nguyen, B.; Henninger, S. K.; Janiak, C. High-Yield, Fluoride-Free and Large-Scale Synthesis of MIL-101(Cr). *Dalton Transactions* **2015**, *44* (38), 16791–16801. https://doi.org/10.1039/c5dt02625c.
(180) Sud, D.; Kaur, G. A Comprehensive Review on Synthetic Approaches for Metal-Organic Frameworks: From Traditional Solvothermal to Greener

Protocols. *Polyhedron*. Elsevier Ltd January 1, 2021, p 114897. https://doi.org/10.1016/j.poly.2020.114897.
(181) Khodaei, M. M.; Dehghan, M. A Green and Cost-Effective Approach for the Production of Gold Nanoparticles Using Corn Silk Extract: A Recoverable Catalyst for Suzuki–Miyaura Reaction and Adsorbent for Removing of Dye Pollutants. *Polyhedron* **2019**, *162*, 219–231. https://doi.org/10.1016/j.poly.2019.01.060.
(182) Lawson, S.; Al-Naddaf, Q.; Krishnamurthy, A.; Amour, M. S.; Griffin, C.; Rownaghi, A. A.; Knox, J. C.; Rezaei, F. UTSA-16 Growth within 3D-Printed Co-Kaolin Monoliths with High Selectivity for CO2/CH4, CO2/N2, and CO2/H2 Separation. *ACS Appl Mater Interfaces* **2018**, *10* (22), 19076–19086. https://doi.org/10.1021/acsami.8b05192.
(183) Alghamdi, H.; Nair, S. A. O.; Neithalath, N. Insights into Material Design, Extrusion Rheology, and Properties of 3D-Printable Alkali-Activated Fly Ash-Based Binders. *Mater Des* **2019**, *167*, 107634. https://doi.org/10.1016/j.matdes.2019.107634.
(184) Lim, G. J. H.; Wu, Y.; Shah, B. B.; Koh, J. J.; Liu, C. K.; Zhao, D.; Cheetham, A. K.; Wang, J.; Ding, J. 3D-Printing of Pure Metal–Organic Framework Monoliths. *ACS Mater Lett* **2019**, *1* (1), 147–153. https://doi.org/10.1021/acsmaterialslett.9b00069.
(185) El-Aal, M. A.; Said, A. E. A. A.; Abdallah, M. H.; Goda, M. N. Modified Natural Kaolin Clay as an Active, Selective, and Stable Catalyst for Methanol Dehydration to Dimethyl Ether. *Scientific Reports 2022 12:1* **2022**, *12* (1), 1–13. https://doi.org/10.1038/s41598-022-13349-0.
(186) Rico-Barragán, A. A.; Raziel Álvarez, J.; Hernández-Fernández, E.; Rodríguez-Hernández, J.; Garza-Navarro, M. A.; Dávila-Guzmán, N. E. Green Synthesis of Metal-Organic Framework Mil-101(Cr) – an Assessment by Quantitative Green Chemistry Metrics. *Polyhedron* **2022**, *225* (July). https://doi.org/10.2139/ssrn.4137378.
(187) Zhang, X.; Shi, X.; Chen, J.; Yang, Y.; Lu, G. The Preparation of Defective UiO-66 Metal Organic Framework Using MOF-5 as Structural Modifier with High Sorption Capacity for Gaseous Toluene. *J Environ Chem Eng* **2019**, *7* (5), 103405. https://doi.org/10.1016/J.JECE.2019.103405.
(188) Li, Z.; Yuan, Y.; Wu, H.; Li, X.; Yuan, M.; Wang, H.; Wu, X.; Liu, S.; Zheng, X.; Kim, M.; Zheng, H.; Rehman, S.; Jiang, G.; Fu, W.; Jiang, J. Investigation of MOF-Derived Humidity-Proof Hierarchical Porous Carbon Frameworks as Highly-Selective Toluene Absorbents and Sensing Materials. *J Hazard Mater* **2021**, *411*, 125034. https://doi.org/10.1016/J.JHAZMAT.2020.125034.
(189) Wang, J.; Muhammad, Y.; Gao, Z.; Jalil Shah, S.; Nie, S.; Kuang, L.; Zhao, Z.; Qiao, Z.; Zhao, Z. Implanting Polyethylene Glycol into MIL-101(Cr) as Hydrophobic Barrier for Enhancing Toluene Adsorption under Highly Humid Environment. *Chemical Engineering Journal* **2021**, *404*, 126562. https://doi.org/10.1016/J.CEJ.2020.126562.
(190) So, P. B.; Liu, C. Y.; Lai, Y. L.; Lee, C. S.; Lin, C. H. MOF@PVA Beads for Dynamic and Low Concentration VOC Capture. *Mater Adv* **2022**, *3* (16), 6458–6465. https://doi.org/10.1039/D2MA00257D.

(191) Shi, X.; Zhang, X.; Bi, F.; Zheng, Z.; Sheng, L.; Xu, J.; Wang, Z.; Yang, Y. Effective Toluene Adsorption over Defective UiO-66-NH2: An Experimental and Computational Exploration. *J Mol Liq* **2020**, *316*, 113812. https://doi.org/10.1016/J.MOLLIQ.2020.113812.

Scientific Contribution

Articles

A.A. Rico-Barragán, J.R. Álvarez, E. Hernández-Fernández, J. Rodríguez-Hernández, M.A. Garza-Navarro, N. E Dávila-Guzmán. **Green synthesis of metal-organic framework MIL-101 (Cr)–An assessment by quantitative green chemistry metrics.** Polyhedron, 2022, Vol. 225, p.116052. doi:10.1016/j.poly.2022.116052. https://www.sciencedirect.com/science/article/abs/pii/S0277538722004041

A.A. Rico-Barragán, J.R. Álvarez, S. Pioquinto-García, J. Rodríguez-Hernández, P. Rivas-García, N. E Dávila-Guzmán. **Cleaner production of metal-organic framework MIL-101(Cr) for toluene adsorption.** Sustainable Production and Consumption Journal, 2023, Vol. 40, 159-168. doi:10.1016/j.spc.2023.06.011 https://www.sciencedirect.com/science/article/abs/pii/S2352550923001446

S. Pioquinto-García, J.R. Álvarez, **A.A. Rico-Barragán**, S. Giraudet, J.M. Rosas-Martínez, M. Loredo-Cancino, E. Soto-Regalado, V.M Ovando-Medina, T. Cordero, J. Rodríguez-Mirasol, N.E Dávila-Guzmán. **Electrospun Al-MOF fibers as D4 Siloxane adsorbent: Synthesis, environmental impacts, and adsorption behavior.** Microporous and Mesoporous Materials, 2023, Vol. 348, p.112327 doi:10.1016/j.micromeso.2022.112327. https://www.sciencedirect.com/science/article/abs/pii/S138718112200645X.

N. Tiempos-Flores, E. Hernández-Fernández, **A.A. Rico-Barragán**, J R. Álvarez, I. Juárez-Ramírez, M.A Garza-Navarro, J. Rodríguez-Hernández, A. Fonseca-García, D.J. Michaelis, N.E. Davila-Guzman. **Enhanced hydrophobicity of modified ZIF-71 metal-organic framework for biofuel purification.** Polyhedron, 2022, Vol. 217, p.115736**.** doi:org/10.1016/j.poly.2022.115736. https://www.sciencedirect.com/science/article/abs/pii/S0277538722000882.

S. Pioquinto-García, N. Tiempos-Flores, **A.A. Rico-Barragán**, N.E. Dávila-Guzmán. **Metal-organic frameworks as adsorbents for impurities of biogas**. Mater. Today Proc., 2022 p. S2214785321018460. doi:2810.1016/j.matpr.2021.02.693. https://www.sciencedirect.com/science/article/pii/S2214785321018460.

Book Chapter

A. A. Rico-Barragán, E. Soto-Regalado, S. Pioquinto-García, N.E. Dávila-Guzmán. **Engineering structured metal-organic frameworks for environmental applications** in **Advanced Materials for Sustainable Environmental Remediation.** 2022, p.175-194. Editor Elsevier. doi:10.1016/B978-0-323-90485-8.00002-3. https://www.sciencedirect.com/science/article/abs/pii/B9780323904858000023.

Patent

A.A. Rico Barragán, N.E. Dávila Guzmán. **Método verde de síntesis de MIL-101(Cr) con capacidad de adsorción de tolueno**. (Sent)

Oral/Poster Presentation

A. A. Rico Barragán, N. Tiempos Flores, M. Loredo Cancino, J. J. Salazar Rabago, J. A. Arcibar Orozco, and N. E. Dávila Guzmán. **"Metal Organic Framework for Adsorption Processes, Synthesis and Mechanism".** LatinXChem Twitter Conference 2020.

A.A. Rico Barragán, N. Tiempos Flores, M. Loredo Cancino, J.J. Salazar Rábago, J.A. Arcibar Orozco, N.E. Dávila Guzmán. **"Aplicación de residuos de PET para la síntesis del MIL-101 (Cr) como posible adsorbente de COV".** Primer Foro de Adsorción en México, 2021.

A.A Rico Barragán. **"Estructuras Metal Orgánicas y su aplicación en Ingeniería Ambiental"**. XXXVI Jornadas Académicas de Ciencias Químicas. La Salle campus Ciudad de México, 2021.

Biographical summary

Alan Antonio Rico Barragán

Candidate for the Degree of Doctor of Science with Orientation in Sustainable Processes

Thesis: Design and Evaluation of a 3D Printed MOF-Monolith for the Removal of Volatile Organic Compound in Indoor Environments.

Field of study: Engineering, Chemical Sciences

Personal Information:
Born in Ciudad Victoria, Tamaulipas, December, 1989, son of Ma. de los Angeles Barragán Delgado y Antonio Rico Trejo.

Education:
- Degree in Chemical Engineering (2008-2012) Tecnológico Nacional de México, campus Cd. Madero.
- Master of Science in Agricultural Systems and Environment (2014-2016). Facultad de Ingeniería, Universidad Autónoma de Tamaulipas.

Research Experience:
- Intership. Facultad de Ingeniería Química, Universidad de Murcia. 2016.
Development of fibroin nanoparticles for the removal of NOx.

Work Experience
Planta Tratadora de Aguas Residuales de Cd. Victoria, Ing. de Operaciones. 2012-2014.
Universidad del Mar de Tamaulipas, Profesor. 2014-2016
Tecnológico Nacional de México, Campus Misantla. Profesor de Tiempo Completo. 2016-2019,
Universidad Autónoma de Nuevo León, Facultad de Ciencias Químicas. 2019

APPENDIX A

Process of $Cr(NO_3)_3*9H_2O$

Sodium Chromate (Na_2CrO_4) is obtained from alkali roasting (soda-ash roasting) of chromite ores (CrO_3) with Sodium Carbonate (Na_2CO_3) in a conventional reaction. Na_2CO_3 (100 kg) is mixed with the CrO_3 (100 kg) and heated at around 900 °C for 2 hours. After the reaction, the product sodium is leached out in the water, and the formation efficiency is 80%.[194] The sodium oxide reacts with the chromium ion in the following manner.

$$2CrO_3 + 4Na_2CO_3 + 3O_2 \rightarrow 4Na_2CrO_4 + 4CO_2 \qquad \text{(a1)}$$

The precursor metal, $Cr(NO_3)_3*9H_2O$, necessary to the synthesis of MIL-101(Cr), is obtained from the reduction reaction of sodium chromate (Na_2CrO_4) in the presence of HNO_3. In a reactor with a temperature of 10°C, 100 kg of Na_2CrO_4 is mixed with 63 kg of HNO_3 (23%); additionally, 20 g of methyl alcohol (CH_3OH) is added. The product is separated through a fritted glass filter and concentrated by boiling. The crystallization of the product occurs at 30 °C, as a result, a slurry is obtained. Finally, chromic nitrate slurry is filtered through a fritted glass filter to collect the $Cr(NO_3)_3*9H_2O$ crystals; the efficiency reaction is about 75%. The reaction to obtain the $Cr(NO_3)_3*9H_2O$ from reduction Na_2CrO_4 as follows:

$$Na_2CrO_4 + HNO_3 + CH_3OH \rightarrow Cr(NO_3)_3 * 9H_2O + Na \qquad (2)$$

Energies requirements for ($Cr(NO_3)_3*9H_2O$) production

The energy consumption of ($Cr(NO_3)_3*9H_2O$) synthetized was estimated based on the heat reaction of the process. The following equations calculate the heat associated with ($Cr(NO_3)_3*9H_2O$).

$$\widehat{H} = \Delta\widehat{H}f^0 + \int_{T1}^{T2} Cp\Delta T \qquad \text{(a3)}$$

$$\Delta H = \sum(n\widehat{H})outputs - \sum(n\widehat{H})inputs \qquad \text{(a4)}$$

$$E_i = \Delta H + FC \qquad \text{(a5)}$$

where:

$\widehat{H}$: specific enthalpy of reactants (kJ mol^{-1})

$\Delta\widehat{H}f^0$: heat of formation of reactants (kJ mol^{-1})

T_1, T_2: Temperature of reference and reactants (°K)

Cp: calorific value of reactants (kJ mol^{-1} $°K^{-1}$)

n: molecular weight

E_i: theoretical energy consumption

FC: Factor endothermic reactions (4.2)

Factor exothermic reactions (3.2)

The values to obtain the LCI for $Cr(NO_3)_3*9H_2O$ production are resume in Table A1.

Table A1. Values for energy balance into $Cr(NO_3)_3*9H_2O$ production.

Reactant/Product	$\Delta\widehat{H}f^0$ (kJ mol^{-1})	Cp (kJ mol^{-1} °K^{-1})	ΔT (°K)	n
Equation 1				
$2CrO_3$	-589.3	0.060		10
$4Na_2CO_3$	-1130.7	0.111	875	9.43
$4Na_2CrO_4$	-1329	0.053		9.87
Equation 2				
$4Na_2CrO_4$	-1329	0.053		6.17
HNO_3	-206.3	0.109		9.99
CH_3OH	-251.3	0.06	-15	0.006
$Cr(NO_3)_3 * 9H_2O$		0.45		3.05

APPENDIX B

Economical Assessment

The price of chemicals was registered to take a count in small quantities (kg or g, and L). The laboratory equipment, such as an oven or reactor, were analyzed as a laboratory scale, meaning a small capacity.

The raw materials and energy requirements for the production of MIL-101(Cr) powder are included in the operational cost. Chemical suppliers were listed and collected to evaluate raw material distribution (Table B1). The raw material value was gathered from different chemical supplier internet pages such as Molbase.com or CTRscientific.com. The cost was registered between December 2021 and March 2022. Finally, the distribution model of each chemical was obtained by MINITAB 19^{TM}.

The energy needed to synthesize MIL-101(Cr) was obtained from LCI data for each scenario. The cost of electricity was 0.88 Mexican currency \$ kWh^{-1}; the operating cost was then obtained by multiplying the energy consumption and adding the raw material cost.

Table B1. Raw materials cost and distribution

Raw material	Distribution	Unit	Mean (US dollar)	Standard Deviation	
H_2BDC	Normal	Kg	1.64	2.48	
			Mean		
DMF	Exponential	Kg	2.14		
$Cr(NO_3)_3*9H_2O$	Exponential	Kg	1.48		
			Min	Max	Mean
Deionized H_2O	Triangular	g	0.03	0.07	0.05
Ethanol	Triangular	g	0.03	3.50	0.77
CH_3COOH	Triangular	g	0.01	0.02	0.01
HNO_3	Triangular	g	0.01	0.01	0.01
Distilled H_2O	Triangular	g	0.06	0.11	0.09

Capital Cost

As the study presented by Luo et al. (2021), because of their significant cost variability, the lab construction and labor costs were not analyzed in this analysis. Although meanwhile, the equipment cost was obtained from Mexican providers (Table S5); due to price variability, the input into Montecarlo Simulation was considered a difference of ± 20% as a previous study.

Table B2. Equipment Cost for MIL-101 (Cr) production.

Equipment Cost (USD $)	-20%		20%
Oven	1789.16	2236.45	2683.74
Ultrasonic	1620.6916	2025.8645	2431.0374
Centrifuge	940.72	1175.9	1411.08
Hydrothermal reactor	83.84	104.8	125.76
Hot plate	1103	1379	1655
Purification equipment	137.25	171.57	205.88
Total Cost (USD $)	4350.5716	5438.2145	6525.8574

Every variable was added with their distribution, and Montecarlo Simulation was run 30,000 times to obtain the mean of 1 g of MIL-101 (Cr)